Development of Galinstan-based Thermal Switches: from 1D to 2D operation

João Pedro Chousa Maganinho
Master in Engineering Physics
Department of Physics and Astronomy
Faculty of Sciences of the University of Porto
2024

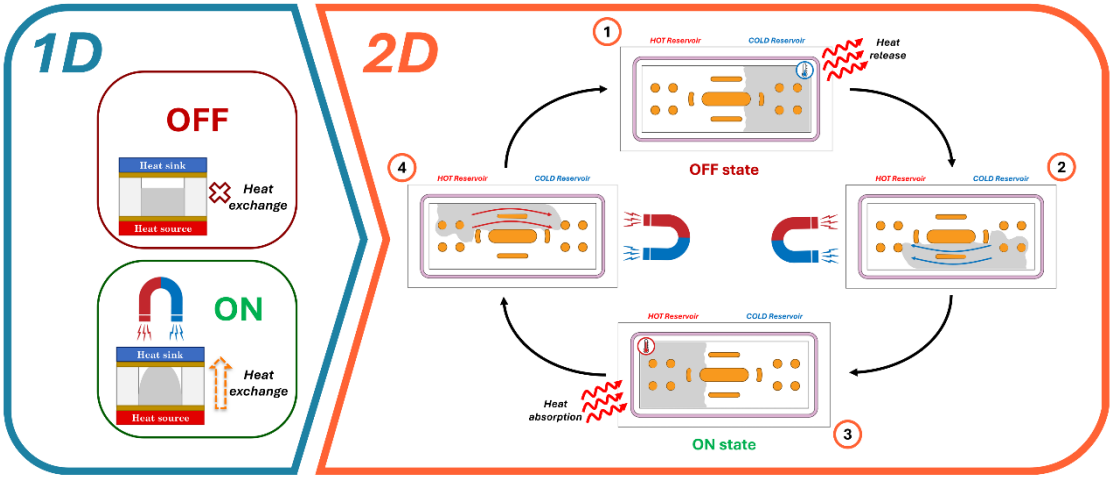

Development of Galinstan-based Thermal Switches: from 1D to 2D operation

João Pedro Chousa Maganinho
Dissertation carried out as part of Master in Engineering Physics
Department of Physics and Astronomy
2024

Supervisor
Dr. João Horta Belo, Auxiliar Professor, Faculty of Sciences of University of Porto

Co-supervisor
Dr. Ana Lúcia Pires, Junior Researcher, Faculty of Sciences of University of Porto

IFIMUP
Institute of Physics for Advanced Materials, Nanotechnology, and Photonics
University of Porto

Dedicated to my family

Acknowledgements

As much as I try, words will always fall short in expressing the profound gratitude I feel. Nonetheless, there are people whose unwavering support over the last five years, and especially during the realization of this dissertation, deserves special recognition.

First and foremost, I would like to extend my deepest thanks to my supervisors, Dr. João Horta and Dr. Ana Pires, for their wisdom, dedication, trust, and mentorship over the past two and a half years. You have shown me that in a supportive and collaborative environment, no obstacle is too great to overcome. Dr. João Horta, your kindness, availability, and above all, your contagious passion for physics, make you an inspiring role model. Dr. Ana Pires, without your expertise, kindness, and constant support, this thesis - like so many others at IFIMUP - would not have been possible.

To the IFIMUP family, the camaraderie fostered through every coffee break and various activities gave me the extra motivation I needed during the last six months. You have made this journey far more enjoyable, and for that, I am deeply grateful.

I must also extend a special thank you to Prof. Paulo Marques for all the insightful conversations and for your guidance, especially during the first year, when everything felt so unclear. Your support helped me shape my path forward, and I will never forget that.

To every friend who crossed my path during this dissertation and stood by my side in these final stressful times, your presence made this achievement far more joyful.

To my close friends, especially to *"Cafezada"*, thank you for the countless coffees, parties, and spontaneous night outs. Some of the happiest memories of my life were made with you, and for that, I am forever grateful.

Last, but certainly not least, I want to thank my family for your unwavering support, for being my safe haven, for showing me that hard work pays off, and for instilling in me the values that have shaped who I am today. You are the four (soon-to-be five) pillars of my life, and I dedicate all my achievements to you.

Resumo

A rápida progressão da inteligência artificial (IA) e da tecnologia de informação (TI) teve um impacto profundo na indústria de semicondutores, exigindo o desenvolvimento de dispositivos compactos com elevada *performance*. No entanto, estes dispositivos enfrentam desafios associados aos níveis elevados de densidade de potência térmica, que as tecnologias de arrefecimento atuais não conseguem gerir de forma eficaz, comprometendo o seu desempenho e durabilidade. Por conseguinte, é de grande interesse desenvolver métodos alternativos de gestão térmica que permitam um controlo eficiente do fluxo de calor, promovendo, assim, a dissipação térmica e prevenindo o sobreaquecimento. Uma linha promissora de investigação assenta na integração de metais líquidos magnéticos à base de *Galinstan* em Interruptores Térmicos Fluídicos Magneticamente Atuados (do inglês MAFTSs). Em comparação com as alternativas existentes, estes dispositivos beneficiam de uma maior condutividade térmica dos fluidos constituintes (o *Galinstan* tem uma condutividade térmica mais de 38 vezes superior à da água) e de uma atuação mais rápida devido à aplicação de campos magnéticos.

Neste contexto, este trabalho propõe o desenvolvimento de dois MAFTS à base de *Galinstan*, com mecanismos de funcionamento distintos. A transição de uma atuação unidimensional (1D) para bidimensional (2D) do fluido oferece duas novas alternativas sem fios para o arrefecimento de dispositivos eletrónicos de diferentes dimensões. Os MAFTS 1D e 2D incorporam diferentes metais líquidos magnéticos que combinam sinergicamente a elevada condutividade térmica do *Galinstan* (valor experimental de $25.5\,\mathrm{W\,m^{-1}\,K^{-1}}$) com o ferromagnetismo de micropartículas (microfluido ferromagnético) e nanopartículas (nanofluido ferromagnético) de Níquel (Ni), respetivamente.

As micropartículas de Ni foram mecanicamente incorporadas numa matriz de *Galinstan* sob uma atmosfera inerte, o que permitiu obter um metal líquido com comportamento ferromagnético. O microfluido ferromagnético, com uma concentração de Ni de $2.6\,\mathrm{wt.\%}$, apresentou uma condutividade térmica de aproximadamente $21\,\mathrm{W\,m^{-1}\,K^{-1}}$. Demonstrou-se experimentalmente que o microfluido pode servir como meio de troca de calor num dispositivo MAFTS 1D, estabelecendo uma ponte térmica eficiente entre a fonte e o dissipador de calor, permitindo, assim, a dissipação do calor gerado pela fonte. A dissipação térmica do MAFTS 1D foi máxima para a menor razão de preenchimento ($65\,\%$) e maior frequência de operação ($0.5\,\mathrm{Hz}$) testadas. Sob estas condições ótimas de funcionamento, foi alcançada uma variação de temperatura de $19.8\,\%$ e um *switching*

ratio de 1.26. O elevado ponto de ebulição do *Galinstan* sugere que o MAFTS 1D terá uma maior longevidade operacional, mantendo o mesmo nível de desempenho, do que as alternativas magneticamente atuadas atualmente disponíveis.

As nanopartículas de Ni foram funcionalizadas com sílica para facilitar a sua incorporação na matriz de *Galinstan*. Posteriormente, as nanopartículas de Ni revestidas com sílica foram incorporadas no metal líquido, seguindo a mesma metodologia aplicada para a fabricação do microfluido ferromagnético. Os nanofluidos produzidos apresentaram um comportamento ferromagnético, demonstrando, assim, que podem ser controlados remotamente através da aplicação de campos magnéticos externos. No entanto, a elevada viscosidade dos nanofluidos ferromagnéticos e a sua adesão às paredes do canal do MAFTS 2D impediram o movimento do metal líquido magnético entre os reservatórios quente e frio.

Por este motivo, integrámos um ferrofluido à base de magnetite no MAFTS 2D para demonstrar a sua viabilidade para aplicações de gestão térmica. Os resultados obtidos indicaram que o aumento da potência da fonte de calor contribui para uma melhoria da capacidade de arrefecimento do dispositivo, devido ao aumento da absorção e libertação de calor. Para a maior potência média da fonte de calor testada ($2.32\,\mathrm{W}$), conseguiu-se alcançar uma redução máxima da temperatura do reservatório quente em $1.33\,^{\circ}\mathrm{C}$. Estes resultados validam a prova de conceito e revelam o potencial do MAFTS 2D para o controlo da temperatura de componentes eletrónicos.

Palavras-chave: Galinstan, Metal líquido magnético, Interruptor térmico fluídico atuado magneticamente, Controlo remoto de calor, Controlo sem fios

Abstract

The rapid progression of artificial intelligence (AI) and Information technology (IT) has profoundly impacted the semiconductor industry, requiring the development of compact, high-performance devices. These devices, however, face challenges related to high thermal power densities that current cooling technologies cannot effectively manage, compromising their performance and durability. It is therefore of great interest to develop alternative thermal management methods that enable an effective heat flux control, thus boosting heat dissipation and preventing overheating. A promising avenue of research relies on the integration of Galinstan-based magnetic liquid metals into Magnetically Actuated Fluidic Thermal Switches (MAFTSs). In comparison to existing alternatives, these devices benefit from an increased thermal conductivity of the base fluids (Galinstan has a thermal conductivity more than 38 times greater than that of water) and a faster actuation due to the application of magnetic fields.

In light of these consideration, the present work proposes the development of two Galinstan-based MAFTS devices with distinct operating mechanisms. The transition from a one-dimensional (1D) to a two-dimensional (2D) working fluid actuation offers two new wireless cooling alternatives for electronic devices of varying sizes. The 1D and 2D MAFTS devices incorporate different magnetic liquid metals that synergistically combine the high thermal conductivity of Galinstan (experimental value of $25.5\,\mathrm{W\,m^{-1}\,K^{-1}}$) with the ferromagnetism of Nickel (Ni) micro (ferromagnetic microfluid) and nanoparticles (ferromagnetic nanofluid), respectively.

Through mechanical alloying within an inert atmosphere, we embedded Ni microparticles in a Galinstan matrix, which provided a liquid metal with a ferromagnetic behavior. The ferromagnetic microfluid, containing a Ni concentration of $2.6\,\mathrm{wt.\%}$, yielded a thermal conductivity of approximately $21\,\mathrm{W\,m^{-1}\,K^{-1}}$. We experimentally demonstrate that the microfluid can serve as heat exchange medium in a 1D MAFTS device. The magnetic liquid metal establishes an optimal thermal bridge between heat source and sink, thereby enabling the dissipation of heat from the source. The 1D MAFTS exhibited optimal heat dissipation for the lower filling ratio ($65\,\%$) and higher operating frequency ($0.5\,\mathrm{Hz}$) tested. Under these optimal working conditions, a temperature span of $19.8\,\%$ and a switching ratio of 1.26 were achieved. The high boiling point of Galinstan suggests that the 1D MAFTS device will have a longer operational lifespan, at the same performance level, than currently available magnetically actuated alternatives.

In order to facilitate the incorporation of the Ni nanoparticles within the Galinstan matrix, a silica deposition process was undertaken. Subsequently, the silica-coated Ni nanoparticles were embedded into the liquid metal, using the same methodology employed for the fabrication of the ferromagnetic microfluid. The produced nanofluids exhibited a ferromagnetic response to applied magnetic fields, thereby demonstrating that they could be remotely controlled through the application of external magnetic fields. However, the high viscosity of the ferromagnetic nanofluids and their adhesion to the 2D MAFTS channel walls prevented the motion of the magnetic liquid metal between the hot and cold reservoirs.

As a consequence, we integrated a magnetite-based ferrofluid into the 2D MAFTS device to demonstrate its feasibility for thermal management applications. Our findings indicated that an increase in the heat source power resulted in an improvement in the cooling performance of the device, due to enhancement of the absorption and rejection of heat. For the higher average heat source power tested ($2.32\,\mathrm{W}$), a maximum reduction of the temperature of the hot reservoir by $1.33\,^{\circ}\mathrm{C}$ was achieved. These results validate the proof-of-concept and unveil the potential of the 2D MAFTS device for temperature control of electronic components.

Keywords: Galinstan, Magnetic liquid metal, Magnetically actuated fluidic thermal switch, Remote heat control, Wireless control

Table of Contents

Acknowledgements i

Resumo ii
Abstract iv

Table of Contents vi
List of Tables ix
List of Figures x
List of Abbreviations xii

Preface 1
Thesis overview 1
Objectives 1
Scientific outreach 2
1. Motivation 3
2. State of the art in electronics thermal management 6
2.1. Thermal control devices 6
2.2. Liquid metals 10
2.3. Computer overheating solutions 14
2.3.1. Software solutions 15
2.3.2. Hardware solutions 15
2.3.2.1. Passive cooling 16
2.3.2.2. Active cooling 17
2.3.3. Overview on current cooling systems 19
3. Experimental characterization techniques 21
3.1. Morphological and chemical characterization 21
3.1.1. Electron Microscopy 21
3.1.2. Differential Scanning Calorimetry (DSC) 23
3.2. Structural characterization 23
3.2.1. Raman Spectroscopy 23
3.2.2. X-Ray Diffraction (XRD) 24
3.3. Magnetic characterization 25
3.4. Transport properties characterization 26
4. Galinstan-based magnetic liquid metals: production and characterization 29
4.1. Galinstan 29
4.1.1. Production method 29

4.1.2. Characterization 30
4.2. Nickel microparticles 34
4.2.1. Production method 34
4.2.2. Characterization 35
4.3. Silica-coated Nickel nanoparticles 37
4.3.1. Production method 37
4.3.2. Characterization 38
4.4. Magnetic liquid metals 46
4.4.1. Ferromagnetic microfluid 47
4.4.1.1. Production method 47
4.4.1.2. Characterization 48
4.4.2. Ferromagnetic nanofluid 50
4.4.2.1. Production method 50
4.4.2.2. Characterization 52
5. 1D cooling performance 55
5.1. Experimental setup 55
5.2. Performance evaluation 56
5.2.1. Performance evaluation trials 57
5.2.2. Influence of the FR and operating frequency on the performance 57
6. 2D cooling performance 62
6.1. Development of the 2D MAFTS device 62
6.1.1. Device design 62
6.1.2. Production method 64
6.2. Experimental setup 67
6.3. Performance evaluation 69
6.3.1. Performance evaluation trials 71
6.3.2. Influence of the heat source power on the performance 72
6.3.3. Influence of the motor operating mode on the performance 73
6.3.4. Comparison with the performance of the 1D MAFTS device 74
7. Conclusions and future work 77
7.1. General conclusions 77
7.2. Future work 79
A. Appendix A - Supplementary multimedia 81
A1. Figures 81
A1.1. Morphological characterization of the commercial Nickel nanoparticles 81
A1.2. 2D cooling experimental setup - Magnetic field distribution 81
A1.3. 2D cooling experimental setup - Electrical circuit diagram 82

B. Appendix B - Characterization of the silica-coated Ni nanoparticles 83
B1. Raman measurements 83
B2. X-ray diffraction measurements 85
B3. Magnetic measurements 86
C. Appendix C - 1D MAFTS device thermal circuit model 89
D. Appendix D - Determination of the specific heat of the PDMS devices 91

Bibliography 92

List of Tables

2.1. Thermophysical properties of fluids suitable for thermal applications 12
2.2. Characteristics of reported Gallium-based magnetic liquid metals 14

4.1. Element wt.% distribution in each zone of the Galinstan EDS measurements 30
4.2. Experimental and reported values for the endothermic ($P1$) and exothermic ($P2$, $P3$ and $P4$) peaks of Galinstan's DSC thermogram 31
4.3. Lattice parameters yielded from the Le Bail refinement of the commercial and silica-coated Ni nanoparticles 45
4.4. Experimental results for the ferromagnetic microfluid Ni $\mathrm{wt.\%}$ determination. 49
4.5. Experimental results for the ferromagnetic nanofluid nanoparticles $\mathrm{wt.\%}$ determination. 52

6.1. Performance comparison between the 1D and 2D MAFTS devices. 75

B1. Position of the Raman peaks in samples containing silica. 85
B2. Summary of the Le Bail refinements to the silica-coated Ni nanoparticles batches. 86
B3. Results from the magnetic characterization of the silica-coated Ni particles. 88

D1. PDMS experimental specific heat values. 93

List of Figures

2.1. Types and operation of thermal control devices 7
2.2. Illustration of the implementation of MAFTS devices in electronics cooling..... 9
2.3. Illustration of the heat sink designs used in computer cooling 16
2.4. Illustration of the heat pipe operating principle and design 17
2.5. Illustration of an air cooling system 18
2.6. Schematic illustration of water-based liquid cooling system..... 19

3.1. Summary of the techniques used for the materials' characterization. 21
3.2. Galinstan sample preparation for magnetization measurements. 26
3.3. Illustration of the transport properties measurement setup. 27

4.1. Illustration of the Galinstan production and storage. 29
4.2. DSC thermogram obtained for a Galinstan sample. 31
4.3. X-ray diffractogram obtained for a Galinstan sample, and comparison with a reported Gallium X-ray diffractogram. 32
4.4. Magnetic curve obtained for a Galinstan sample. 33
4.5. Electrical resistivity measurements obtained for a Galinstan sample. 34
4.6. Illustration of the Ni microparticles production. 35
4.7. SEM image and particle size distribution of the Ni microparticles. 36
4.8. X-ray diffractogram and magnetic hysteresis curve of the Ni microparticles. 36
4.9. Illustration of the different stages comprising the silica coating of the Ni nanoparticles. 39
4.10. SEM top-view images of the commercial Ni nanoparticles, and histogram with the particle size distribution. 40
4.11. SEM top-view images of the silica-coated Ni nanoparticles, and histogram with the particle size distribution. 41
4.12. Normalized Raman spectra of the commercial (a) and silica-coated (b) Ni nanoparticles. 43
4.13. Room-temperature X-ray diffractograms of the commercial (a) and silica-coated (b) Ni nanoparticles. 44
4.14. Magnetic curves obtained for the commercial and silica-coated Ni nanoparticles. 46
4.15. Illustration of the ferromagnetic microfluid production and storage. 47
4.16. SEM image of the ferromagnetic microfluid. 48
4.17. Magnetic curve obtained for a FM microfluid sample. 49
4.18. Electrical resistivity measurements obtained for a ferromagnetic microfluid sample. 50
4.19. Magnetic curves obtained for a ferromagnetic nanofluid sample, for different after-production time spans. 53
4.20. Isofield magnetization versus temperature curves obtained for a ferromagnetic nanofluid sample, for different after-production time spans. 54

5.1. Illustration of the experimental setup (a) and the device (b) used to evaluate the performance of the ferromagnetic microfluid. 55
5.2. Illustration of the effects of the 1D MAFTS operation throughout a complete trial. 58
5.3. Illustration of the influence of the filling ratio and operating frequency on the performance of the 1D MAFTS. 59

6.1. Illustration of the structure (a), working principle (b), and 3D design (c) of the 2D MAFTS device. 63
6.2. Illustration of the different stages comprising the production of a 2D MAFTS device. 65
6.3. Illustration of the experimental setup used to evaluate the 2D MAFTS performance. 67
6.4. Illustration of the ferromagnetic nanofluid (a) and commercial ferrofluid (b) within the 2D MAFTS device. 70
6.5. Illustration of the temperature variation of the cold and hot reservoirs throughout a 2D MAFTS device complete trial. 71
6.6. (a) Illustration of the time evolution of the temperature span for each heat source average power tested. (b) Dependence of the minimum temperature rate on the average power. 73
6.7. (a) Illustration of the time dependence of the hot reservoir temperature for the feedback operating mode, during the device operation. (b) and (c) Time evolution of the temperature span and ΔT_{cycle}^{hot} for both operating modes. 75

A1. TEM images of the commercial Ni nanoparticles. 81
A2. Simulated magnetic field lines and intensity distribution produced by the magnetic configuration used in the 2D MAFTS setup. 81
A3. Diagram of the electric circuit used to control the rotation of the magnets in the 2D MAFTS setup. 82

B1. Normalized Raman spectra of the analyzed batches of silica-coated Ni nanoparticles. 84
B2. Room temperature X-ray diffractograms of the analyzed batches of silica-coated Ni nanoparticles. 86
B3. Magnetic curves obtained for the analyzed batches of silica-coated Ni naparticles. 87

C1. Thermal circuit model of the 1D MAFTS device at the stationary state. 90

D1. Temperature variation during the cooling of the hot and cold reservoirs for the determination of the specific heat of PDMS. 92

List of Abbreviations

AI Artificial Intelligence

IT Information Technology

CEAP Circular Economy Action Plan

MAFTS Magnetically Actuated Fluidic Thermal Switch

TCD Thermal Control Device

RTLM Room-temperature Liquid Metal

LM Liquid Metal

1D One-dimensional

2D Two-dimensional

TS Thermal Switch

PDMS Polydimethylsiloxane

PMMA Poly(methylmethacrylate)

MHD Magneto-hydrodynamic

CPU Central Processing Unit

HTC Heat Transfer Coefficient

SEM Scanning Electron Microscopy

EDS Energy Dispersive X-ray Spectroscopy

TEM Transmission Electron Microscopy

SE Secondary Electrons

BSE Backscattered Electrons

DSC Differential Scanning Calorimetry

XRD X-ray Diffraction

SQUID Superconducting Quantum Interference Device

TC Thermocouple

TEOS Tetraethyl Orthosilicate

DI Deionized

2M Two-magnon

1P One-phonon

2P Two-phonon

FCC Face-centered Cubic

HCP Hexagonal Close Packed

FR Filling Ratio

PLA Polyactic Acid

SAS Stamp and Stick

IR Infrared

CHTC Convective Heat Transfer Coefficient

Preface

Thesis overview

This document is divided into a preface and seven main chapters. The **preface** outlines the overarching goals of this research and highlights its scientific outreach. The **first chapter** briefly discusses the motivation underpinning this dissertation. The **second chapter** provides a review of the state of the art in electronics thermal management, with the objective of contextualizing the proposed magnetic liquid metal-based magnetically actuated fluidic thermal switch (MAFTS) devices within the existing range of cooling alternatives. The **third chapter** introduces the techniques used to characterize the properties of the materials produced, including the information provided by them and the experimental details about their utilization. Subsequently, the **fourth chapter** outlines the methodologies employed to produce the constituent materials of the magnetic liquid metals, and presents the findings from their characterization.

The **fifth** and **sixth chapters** present the experimental setups used to evaluate the cooling performance of the 1D and 2D MAFTS devices, respectively, and the results from each of those evaluations. In the latter, particular emphasis is placed on the design and fabrication of the 2D MAFTS device itself.

Finally, in the **seventh chapter**, the main conclusions are highlighted and future research directions are suggested.

Objectives

The principal objective of this thesis is to develop two MAFTS devices with distinct operating mechanisms. These incorporate different magnetic liquid metals that synergistically combine the high thermal conductivity of Galinstan with the ferromagnetism of Ni micro (ferromagnetic microfluid) and nanoparticles (ferromagnetic nanofluid). The first MAFTS device incorporates a ferromagnetic microfluid, which exhibits a one-dimensional (1D) motion in the direction of the gravitational force. The second device was designed to facilitate a two-dimensional (2D) actuation of the ferromagnetic nanofluid. These devices

offer a new cooling alternative for different-sized electronic equipment. To this end, the constitutive materials of the magnetic liquid metals were synthesized and thoroughly characterized; a new 2D MAFTS device was designed and fabricated; the performance of both 1D and 2D MAFTS devices was evaluated with suitable magnetic fluids, on home-made experimental setups.

Scientific outreach

Throughout the dissertation, this work was presented in the following conferences:

- **IEEE Around-the-Clock Around-the-Globe Magnetics Conference 2023**, Online, 27 September 2023, with a poster presentation named "*Production of a Thermal Switch with a Galinstan based Ferromagnetic Fluid*"
- **EMFL Spring School 2024**, Dresden, Germany, 15-19 April 2024, with a pitch and a poster presentation named "*Production of a Galinstan-Based Ferromagnetic Fluid for Thermal Management Applications*"
- **2024 European School on Magnetism**, York, United Kingdom, 26 August - 6 September 2024, with a poster presentation named "*Magnetic Liquid Metal for Thermal Management*"

Furthermore, the following article has been published in the Energy Conversion and Management journal:

- **J. P. Maganinho**, R. M. C. Pinto, V. Andrade, B. G. F. Eggert, C. Frommen, J. P. Araújo, J. O. Ventura, J. Oliveira, A. L. Pires and J. H. Belo, "Engineering a Galinstan-based Ferromagnetic Fluid for Heat Management", *Energy Conversion and Management*, vol. 322, 2024

1. Motivation

The issue of thermal power density represents a significant challenge in meeting the demands of technological evolution. As indicated in a report by McKinsey & Company [1], the advent of artificial intelligence (AI) is set to drive a 100-fold increase in computer demand over the next five years. This, in conjunction with the accelerated advancement of information technology (IT), has led to an intensifying pressure within the semiconductor and chip development sectors. As predicted by Moore in 1965 [2], computing power has been doubling approximately every two years, with the devices' characteristic dimensions shrinking to the nanometric scale. However, advancements in this field have begun to plateau, as this shrinkage has brought several challenges, specifically, an increase in heat generation, responsible for device overheating [3–5]. To date, the maximum chip heat flux has reached $200\,\mathrm{W\,cm^{-2}}$, with projections indicating that it will imminently exceed $500\,\mathrm{W\,cm^{-2}}$ [6]. Localized heat fluxes are also anticipated to reach values of $1000\,\mathrm{W\,cm^{-2}}$ [6]. Consequently, the ineffective dissipation of the heat generated poses a threat to the performance, reliability and durability of electronic equipment. The failure rate of such equipment has been observed to follow a near exponential rise with operating temperature [6]. Efficient thermal management solutions, that dissipate the heat generated and keep the devices' working temperature within optimal values, are therefore in great need. This is not only essential for achieving the demanded computational power, but also for enhancing the equipment's endurance. The latter is intrinsically aligned with the Ecodesign Directive from the new Circular Economy Action Plan (CEAP) [7], which is one of the main building blocks of the European Green Deal [8].

As the boundaries of performance and power consumption are extended, the shortcomings of existing cooling solutions become more evident. To illustrate, in data centers, the cooling features account for up to $40\,\%$ of total energy consumption [9], with air cooling representing a significant contributor to wasted heat power [10]. The amount of energy consumed, and the space required for air cooling to dissipate heat are increasing at an unsustainable rate. In order to overcome this challenge, the industry has shifted towards liquid cooling systems. Despite offering enhanced cooling efficiency, these systems still require significant energy consumption. This has given rise to a growing interest in new thermal control devices (TCDs), which enable effective heat flux control (by adjusting

their thermal resistance) and thus boost heat dissipation and prevent overheating [11–15]. Among the different TCDs, thermal switches have the potential to regulate temperature transients and to actuate on localized hotspots. In analogy to their electronic counterpart, these devices are capable of switching the heat flux propagation state (high/low thermal conductivity) between two elements at different temperatures. Thermal switches' actuation relies on the application of an external stimulus. For instance, when a magnetic field is considered for such, these novel devices benefit from a precise and fast switching ability.

The use of fluids as heat exchange materials in TCDs stands out for their increased performance, which is mainly linked to the notorious decrease in thermal resistance they promote between the different elements of the thermal circuit [13, 16]. In fluidic TCDs, the thermal conductivity of the working fluid is a critical operating parameter. For applications around room temperature, conventional liquids (such as water, ethylene glycol and oil) do not have thermal conductivities as high as those of room-temperature liquid metals (RTLMs). Gallium-based alloys emerge as one of the most promising RTLMs. Benefiting from the high solubility of Gallium (Ga), Indium (In) and Tin (Sn) within each other, it is possible to form a monophasic alloy known as Galinstan. The standard composition for Galinstan is Ga/In/Sn $(68:22:10)$ wt.% [17]. Notably, this liquid metal (LM) has a thermal conductivity which surpasses more than 38 times that of water ($0.607 \pm 0.004\,\mathrm{Wm^{-1}K^{-1}}$ [18]) [18–21]. The use of this technology as a thermal interface material is already mature, being employed in ASUS laptops [22] and in Sony Playstation 5 [23]. The thermophysical properties of this non-toxic liquid metal, in particular, its high boiling point and surface tension, ensure a reduced probability of leakage during its usage. This is a common issue in other liquid cooling systems which not only affects the cooling efficiency of the system, due to the decrease in the volume of the working fluid, but also endangers the integrability of the surrounding electronics. Besides its advantageous thermophysical properties, Galinstan is also renowned for its compatibility with magnetic materials [24]. This attribute enables the control of the motion of Galinstan-based magnetic liquid metals by applying external magnetic fields, prompting its use in magnetically actuated fluidic thermal switches (MAFTSs).

Keeping all these aspects in mind, the present work proposes the development of two different magnetic liquid metals, which synergistically combine the large heat conductivity of Galinstan with the ferromagnetism of Nickel micro (ferromagnetic microfluid) and nanoparticles (ferromagnetic nanofluid). The microfluid is designed to be incorporated into

a centimetre-thick MAFTS device. Here the fluid moves axially in the direction of the gravitational force. Application-wise, for example, centimetre-scaled electronic device cooling [25] and caloric-effect-based refrigeration [15] can be targeted with this 1D MAFTS. The nanofluid is intended for a planar actuation in a millimetre-thick MAFTS device, which is primarily designed for chip cooling applications. With this, we hope to present new wireless cooling alternatives that are able to control heat fluxes through the application of external magnetic fields.

2. State of the art in electronics thermal management

2.1. Thermal control devices

Controlling the thermal state at the device and die levels is a key challenge in modern technology [5, 15]. The high-level of integration and compact layout of these systems has created several electro-thermal obstacles. In specific, their non-uniform spatial and temporal heat dissipation can lead to the generation of temperature gradients and localised heat fluxes (which can reach values as high as $1\,\mathrm{kW\,cm^{-2}}$), that hinder the performance and reliability of the system. [16, 26] Current cooling methods cannot provide an efficient solution, forcing devices to rely on throttling to avoid irreparable damage [4, 5]. Therefore, in recent years, researchers have begun to look beyond the state of the art, by exploiting innovative TCDs [15, 27].

The implementation of TCDs in thermal circuits enables the effective control of the heat flux propagation between two elements at different temperatures. These devices limit the local and transient heat propagation by adjusting their thermal resistance. [4, 11–15, 28] Indeed, this capability has prompted research into the potential application of TCDs in areas beyond electronics thermal management. These devices have been proposed to implement adiabatic and isothermal processes within thermodynamic cycles, specifically those employed in electrocaloric or in magnetocaloric refrigeration [28]. Moreover, they have the potential to enhance the Carnot efficiency of thermal energy harvesting systems [13]. As illustrated in Figure 2.1, different types of TCDs can be considered for such applications, each with its own operating principle. In thermal diodes and thermal regulators, the thermal resistance changes in response to temperature variations. Conversely, the thermal resistance of thermal transistors and thermal switches is temperature independent. Instead, these TCDs only operate under variations of an external stimulus (pressure, electric field, magnetic field, etc.). [4, 13]

These systems can be further separated into two groups: solid-state TCDs and fluidic TCDs. The operation of solid-state TCDs relies on the phase transition of phase change materials. Usually, these devices do not possess any moving parts [29]. The absence of actuation mechanisms reduces the overall mass and size of the system, favoring the

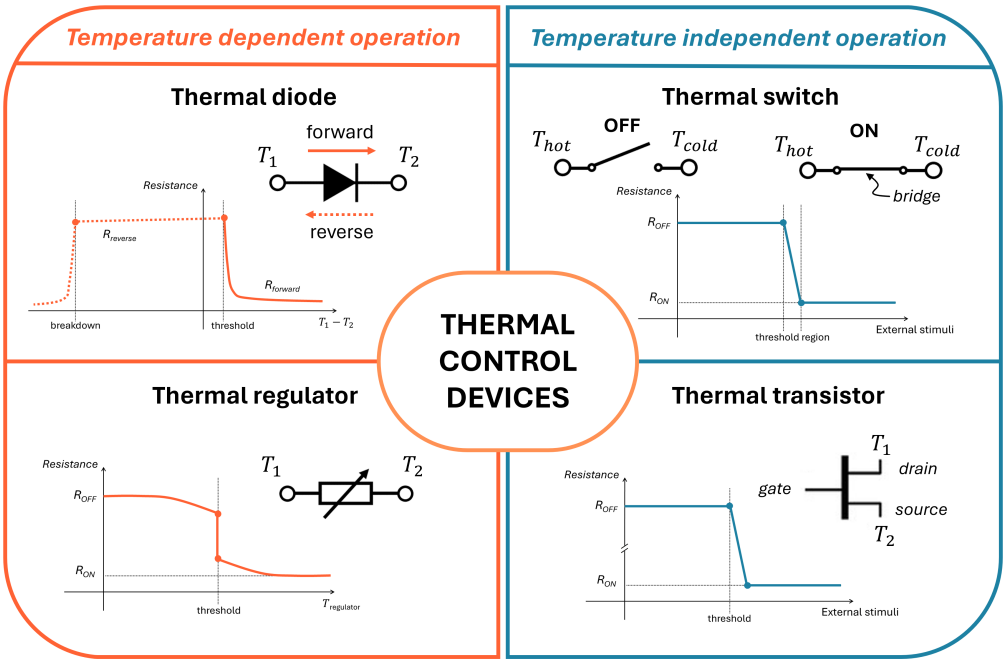

FIGURE 2.1: Types and operating principle of thermal control devices. Adapted from Ref. [4].

development of more compact designs [4]. However, the surface roughness in the interface between two solids constitutes a setback to heat conduction. The use of fluids as heat exchange material in fluidic TCDs represents a promising alternative. In fact, the adaptability of fluids to surfaces allows a significant decrease in the interface thermal resistance. [13, 16, 25] As a consequence, the use of fluidic TCDs comes with an enhancement in the heat flux across the contact surface [27]. In addition, the versatility of these devices offers a broader range of design possibilities.

Among the forementioned TCDs, thermal switches (TSs) provide the largest range of thermal control, being able to maintain an uniform temperature even during variations of the external thermal conditions. Furthermore, TSs are suitable for localized cooling. [25] Similarly to an electrical switch, a TS has two operating states (ON and OFF) and comprises three terminals (the hot end, the bridge and the cold end), as illustrated in Figure 2.1. Typically, in the absence of an external field, the TS rests in a state with higher thermal resistance - the OFF state - where the hot and cold ends are not thermally connected. As the external field surpasses a certain threshold, the bridge connects both terminals, and the TS transits to a lower resistance state - the ON state. This switching between states is accompanied by an increase in the heat transferred from the hot to the cold end. [30] Therefore, by controlling the applied stimulus intensity, one can effectively manipulate the heat flux through the device. In addition, conciliating the working principle

of TSs with the incorporation of fluids as heat exchange media can further boost their performance. [11]

The three most important performance metrics of TSs are: the switching time (τ), the switching ratio (SR) and the energy efficiency (ε) [31]. The switching time corresponds to the time necessary for the TS to transit between operating states. The switching ratio is defined as the ratio between the heat flux during the ON state $\left(\dot{Q}_{\mathrm{ON}}\right)$ and the heat flux during the OFF state $\left(\dot{Q}_{\mathrm{OFF}}\right)$, as can be depicted in Equation 2.1. The energy efficiency of a TS which requires an external power supply (P) is given by Equation 2.2. There, $\dot{Q}_{\mathrm{in}}$ is the input heat flow rate and $\dot{Q}_{\mathrm{out}}$ is the output heat flow rate. An ideal TS should have high switching ratio and energy efficiency. The switching time-scale is application-dependent. [4]

$$\mathrm{SR} = \frac{\dot{Q}_{\mathrm{ON}}}{\dot{Q}_{\mathrm{OFF}}} \tag{2.1}$$

$$\varepsilon = \frac{\dot{Q}_{\mathrm{out}}}{\dot{Q}_{\mathrm{in}} + P} \tag{2.2}$$

Based on their operating mechanism, fluidic TSs can be classified as mechanically-, electrically- or magnetically-actuated. Compared to mechanically-actuated fluidic TSs, electrically-actuated ones benefit from the absence of moving parts to promote the fluid manipulation. This diminishes the noise, vibration and friction during operation. Furthermore, the application of electric fields enables a precise control of the fluid motion. Nevertheless, the required electric field strengths can reach extreme values, unfeasible for applications. Another alternative relies on the application of magnetic fields. Actually, MAFTSs are reported to have the fastest switching response from the three, while maintaining the ability to precisely and remotely control the fluid motion. [4, 28]

The utilisation of MAFTSs has been proposed in a broad range of applications, spanning the realms of thermal management in spacecrafts [32–34] and caloric-effect refrigeration [31, 35]. Nevertheless, of utter interest in the context of this thesis, is their successful implementation in electronics cooling. For instance, Puga *et al* [25] proved the applicability of a MAFTS device in the thermal management of a $10\,\mathrm{W}$ LED. The developed experimental setup and the diagram of the MAFTS device are illustrated in Figures 2.2 (a) and (b), respectively. A set of permanent magnets rotating at a predefined frequency was considered as time-varying magnetic field source. As working fluid, a commercial ferrofluid, consisting of a colloidal mixture of $\mathrm{Fe_3O_4}$ nanoparticles dispersed in poly-α-olefin oil, was considered. In Figure 2.2 (c) are presented the experimental results obtained for

a MAFTS operating frequency of $10\,\mathrm{Hz}$ and different starting operation times ($t = 60\,\mathrm{s}$ and $t = 700\,\mathrm{s}$). As can be seen, independently of the starting operation time, the LED working temperature was reduced by $17\,^{\circ}\mathrm{C}$ (from $63\,^{\circ}\mathrm{C}$ to $46\,^{\circ}\mathrm{C}$), in comparison to the case where the LED heated with the MAFTS turned off. Moreover, this temperature variation was found to be frequency-independent for MAFTS operating frequencies in the range from $5\,\mathrm{Hz}$ to $30\,\mathrm{Hz}$.

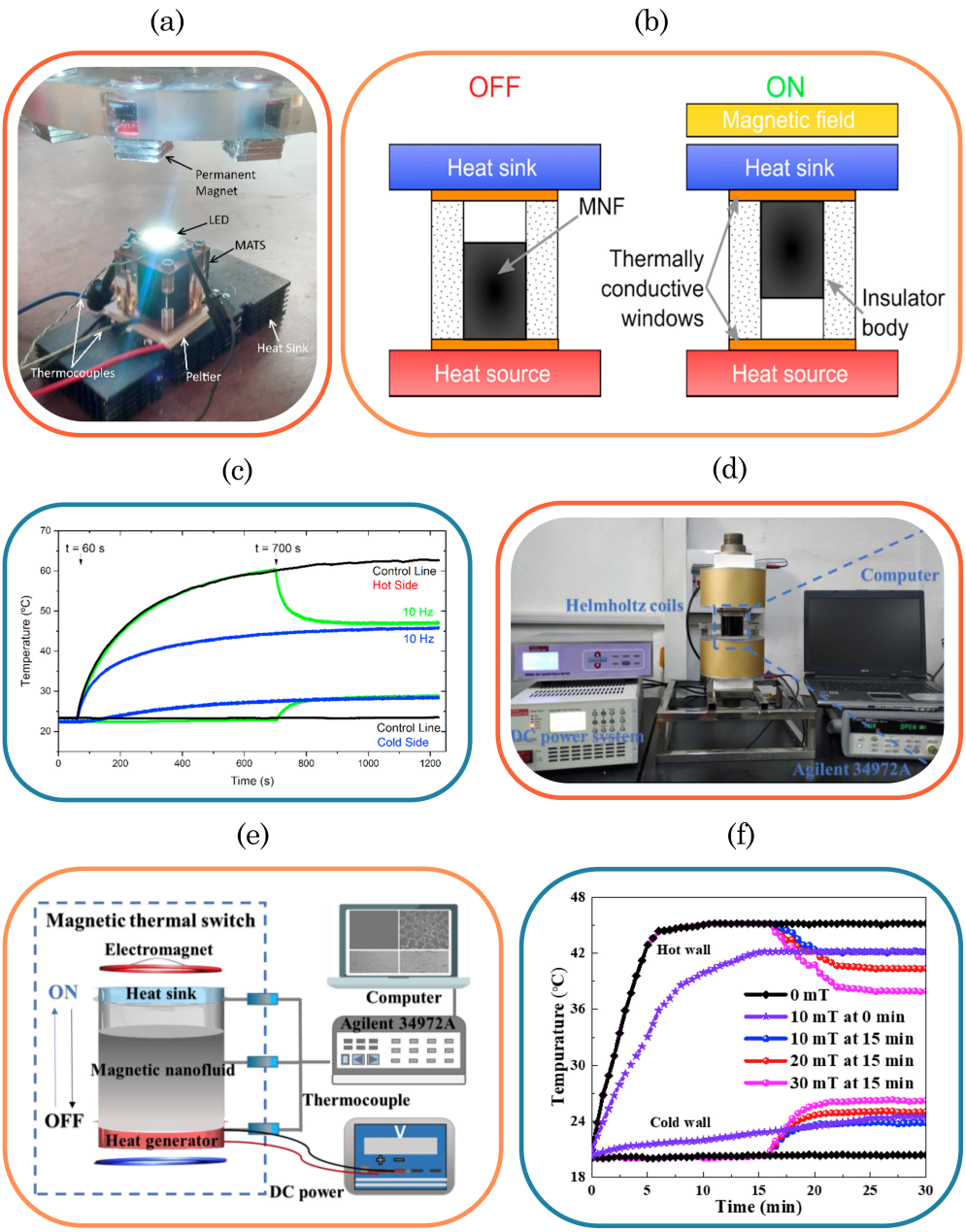

FIGURE 2.2: Illustration of the implementation of MAFTS devices in two different electronics cooling applications. The experimental setups (subfigures (a) and (d)), the schematic representation of the MAFTSs (subfigures (b) and (e)) and the time evolution of the temperature of the cooled electronic devices (sufigures (c) and (f)) are illustrated. Subfigures (a), (b) and (c) were obtained from Ref. [25], and subfigures (d), (e) and (f) from Ref. [14].

Another MAFTS system was proposed by Shi *et al* [14], where a pair of Helmholtz coils was considered instead as field source. An image of the setup and a diagram of the device are depicted in Figures 2.2 (d) and (e), respectively. By applying a magnetic field strength of $30\,\mathrm{mT}$, the temperature of a Peltier element (the hot wall), working with a heating power of $14\,\mathrm{W}$, was reduced by $8.1\,^{\circ}\mathrm{C}$ (from $45.3\,^{\circ}\mathrm{C}$ to $37.2\,^{\circ}\mathrm{C}$), as illustrated in Figure 2.2 (f).

2.2. Liquid metals

RTLMs are single or alloyed metals with melting points bellow or near room temperature and high boiling points, which enable them to manifest metallic characteristics in a fluidic state, even at ambient conditions [36]. Motivated by this unique advantage, during the last decades RTLMs have been an object of profound investigation, which led to the discovery of interesting physical, chemical, electronic and optical properties. Additionally, the response of LMs to different stimuli has prompted their utilisation as energy conversion sensitizers in a wide range of applications, from light sensitizers in photothermal therapy, to electro-thermal convertors for flexible electronics [36, 37]. In fact, due to their distinct chemical response, these fluids can even be considered as reaction solvents [38]. More importantly, the high thermal conductivity of LMs offers an unique cooling alternative for high density power sources in the most diverse realms, from nuclear reactors [39, 40] and solar cells [41], to electronic devices cooling [36, 42, 43].

In nature there are only five single-element RTLMs: Cesium (Cs), Rubidium (Rb), Francium (Fr), Mercury (Hg) and Ga. The first three (Cs, Rb and Fr) are not suitable for daily applications, due to their high reactivity with water, pyrophoricity and radioactivity, respectively [39, 44]. Even though Hg is the most well-known RTLM and can still be found in many day-to-day instruments (such as thermometers and electromechanical relays [45]) its toxicity has limited its use, motivating research on other alternatives [46]. Besides being non toxic, Ga has several properties (low vapor pressure, high boiling point, etc.) that highlight it as the best choice from these single-element RTLMs. However, the melting point of this metal (around $29.8\,^{\circ}\mathrm{C}$ [47]) is higher than that required for some room-temperature applications, specifically for chip cooling. Nevertheless, it is reported the existence of multi-elements LM alloys with feasible melting temperatures. Starting with NaK, in spite of being the lowest melting point LM ($-11\,^{\circ}\mathrm{C}$ [39]), it comes with the adversity of being reactive towards air and water, implying a possible fire hazard. Hence its use as coolant would require special safety considerations to prevent any leakage [39]. A promising alternative to all the aforementioned hazardous LMs is to benefit from the

solubility of Ga, In, Sn and Zinc (Zn) within each other to produce alloys with a melting point lower than that of Ga, whose value depends on the exact chemical stoichiometry. These alloys are typically referred to as Ga-based LMs.

Since the first proposal of Ga-based LMs as coolant for chip cooling in 2002 [42], they have been intensively investigated for incorporation in new thermal management technologies. In fact, besides their high thermal conductivity, these LMs present several characteristics that motivate their usage in such applications. First of all, Ga-based LMs are non-toxic, have low vapor pressure ($< 10^{-6}\,\mathrm{Pa}$ at $500\,^{\circ}\mathrm{C}$) and show low dissolution in water, assuring the safety of its users. The dynamic viscosity of Ga is about 1.5 times that of water ($1.002\,\mathrm{mPa\,s}$ [48]), ensuring seamless pumping of these LMs through small channels. Moreover, their high boiling point allows a single-phase operation, which, alongside with their high surface tension and low vapor pressure, reduces the leakage probability.

The most commonly used Ga-based LMs are the eutectic Ga-In (EGaIn), with a Ga/In $(75:25)$ wt.% composition [49], and the Ga-In-Sn monophasic alloy, also known as Galinstan, whose standard composition is Ga/In/Sn $(68:22:10)$ wt.% [17]. Other less used Ga-based LMs are reported, namely: Ga-Sn ($\mathrm{Ga_{86.5}Sn_{13.5}}$, where the subscript denotes the element wt.%), Ga-Sn-Zn ($\mathrm{Ga_{86}Sn_{11}Zn_3}$) and Ga-In-Sn-Zn ($\mathrm{Ga_{61}In_{25}Sn_{13}Zn_1}$) [49]. In Table 2.1 are summarized some thermophysical properties of these Ga-based LMs, as well as of other fluids typically used in thermal applications.

From the Ga-based alloys, $\mathrm{Ga_{61}In_{25}Sn_{13}Zn_1}$ has the lowest melting point with a reported value of $7.6\,^{\circ}\mathrm{C}$ [52], which could suggest its applicability as a fluidic coolant. However, this LM is more viscous, making it more suitable for usage as a thermal interface material [41]. Galinstan is the Ga-based LM with the second lowest melting temperature, with reported values ranging from $10.6\,^{\circ}\mathrm{C}$ to $13.2\,^{\circ}\mathrm{C}$. [17, 20, 57]. Moreover, Galinstan shows remarkable thermophysical properties that prompt its incorporation in fluidic circuits for electronic devices cooling. Deviations from the standard composition of Galinstan can alter its baseline thermal properties, specifically, its thermal conductivity, which lies within $24 \pm 1\,\mathrm{Wm^{-1}K^{-1}}$ [19–21]. Notably, these values exceed more than 38 times that of water ($0.607 \pm 0.004\,\mathrm{Wm^{-1}K^{-1}}$ [18]). If appropriate operating conditions are considered, this improvement in thermal conductivity can compensate the nearly half volumetric heat capacity of Galinstan (in the range $2.2 \pm 0.3\,\mathrm{MJ\,m^{-3}\,K^{-1}}$ [19–21]) relative to that of water ($4.183\,\mathrm{MJ\,m^{-3}\,K^{-1}}$ [49]), therefore resulting in an enhancement of the cooling performance.

TABLE 2.1: Thermophysical properties of fluids suitable for thermal applications, including the reported Gallium-based liquid metals. Except for those specifically identified, the values were obtained at room temperature conditions

Fluid	Thermal conductivity $\left(\mathrm{W\,m^{-1}\,K^{-1}}\right)$	Heat capacity $\left(\mathrm{MJ\,m^{-3}\,K^{-1}}\right)$	Melting point (°C)	Boiling point (°C)	Density $\left(\times 10^3\,\mathrm{kg\,m^{-3}}\right)$	Dynamic viscosity (mPa s)	Surface tension $\left(\mathrm{mN\,m^{-1}}\right)$	References
Water	0.607^a	4.183	0	100	0.998^b	1.002	72.8^b	[18, 47, 48, 50]
Ethylene glicol	0.258	2.659	−12.6	197.2	1.132	9	48.4	[47]
Mercury	8.34^c	1.883^c	−38.87	356.65	13.546^c	1.50 – 1.83	455^c	[47, 48, 50]
Gallium	29.4^d	2.186^d	29.8	2204.8	5.907^d	2.0	707^d	[47, 48, 50]
EGaIn	26.58^b	2.556^b	16	> 1300	6.280^b	1.69 – 2.50	624^b	[20, 47, 48]
Galinstan	23.03 – 25.25	1.874 – 2.481	10.6 – 13.2	> 1300	6.33	$1.89 – 2.40^e$	$587 – 605^b$	[17, 19–21, 38, 48]
$Ga_{86.5}Sn_{13.5}$	–	–	20.5	–	6.17	–	670	[49, 51]
$Ga_{86}Sn_{11}Zn_3$	–	–	14.9	–	6.14	–	–	[49]
$Ga_{61}In_{25}Sn_{13}Zn_1$	15 – 23.2	2.844 – 2.925	7.6	> 900	6.32 – 6.50	4.0	500 – 639	[52–56]

^{a} at 25 °C and 0.1 MPa; ^{b} at 20 °C ; ^{c} at 25 °C; ^{d} at 50 °C; ^{e} at 35 °C

In spite of its numerous advantages, the usage of Ga-based LMs, specifically, Galinstan, brings some challenges. For instance, under ambient conditions, or in any environment with oxygen levels above $1\,\mathrm{ppm}$, an oxide layer instantaneously forms on the surface of Galinstan in order to prevent the oxidation of its core. This nm-thick layer is mostly composed by Gallium oxides (Ga_2O_3 and Ga_2O), since Ga has the smallest reduction potential among the three constituent elements (Ga, In and Sn) [44, 58]. After oxidation, the surface tension and the wettability of the LM decrease, while its adhesion increases, thereby impeding fluidic motion. Consequently, different strategies have been developed to remove the oxide skin, including the utilization of chemical reactions. One potential method for removing the oxide layer is to expose the LM to concentrated HCl vapor. An alternative approach is to submerge the LM in either a highly acidic HCl or a highly alkaline NaOH chemical etchant bath. The choice of solution essentially influences the oxide removal timescale, as both solvent solutions effectively remove the oxide skin [46]. However, the highly corrosive effect of the reagents in discussion limits the applicability of these methods in thermal management. An intelligent alternative, from a technical perspective, is to accept the inevitability of the oxide formation and precisely leverage from a Galinstan oxide surface coating to reduce the adhesive effect of the LM [59, 60].

The compatibility of Galinstan with another material is intrinsically connected to the interactions between the oxide skin and the surface of that material. Actually, there are several reports of Galinstan's corrosive effect when in contact with metals commonly used in cooling devices, namely, Copper (Cu) and Aluminium (Al). [43, 52, 61] Therefore, when designing a device with Galinstan as working fluid, the choice of materials is critical. Even though it is possible to protect the metallic substrates with an anti-corrosion coating [62], sometimes it might be preferable to consider other metals, such as stainless steel [43]. In fluidic transport applications, the use of non-metals facilitates the development of microfluidic channels. In accordance, Polydimethylsiloxane (PDMS) [63–68], Poly(methyl methacrylate) (PMMA) [69] and Polymide [70, 71] have been considered in such applications.

The motion of Ga-based LMs can be induced by generation of external forces. These forces can derive from a mechanical source. However, the latter are linked to undesired noise and vibrations. Instead, one can benefit from the characteristics of these LMs to develop a noise- and vibration-free fluid transportation method. The high electrical conductivity of these LMs allows their manipulation under electromagnetic fields. For instance, due to exertion of an electric field one can induce a variation of the interfacial tension across the LM, to promote its movement. One can even achieve higher speeds for the same applied voltage if the LM is immersed in a liquid electrolyte (HCl or NaOH, e.g.) [46]. Another alternative is to induce the fluid movement through magneto-hydrodynamic (MHD) pumping, where a current is applied through the conducting fluid, and orthogonal to an external magnetic field, to generate a mutually orthogonal Lorentz force, thus fluid acceleration [39, 72, 73]. Moreover, Ga-based LMs can be successfully endowed with magnetic properties [24]. As evidenced in Table 2.2, in previous research, different magnetic particles have been added into a LM matrix to produce different magnetic LMs. This enables the control of the fluid motion only through application of external magnetic fields. Generally there are some mismatches between the LM and the magnetic particles, including differences in density and interfacial interactions, which can difficult the combination of their properties. Nonetheless, various production techniques have been developed to overcome these challenges. One strategy is to continuously break and renew the LM oxide layer, thereby leveraging the layer's high adhesive quality to mix the particles within the LM matrix. For instance, Castro *et al.* [17] manually grinded micrometer-sized Gadolinium particles into Galinstan in a N_2 atmosphere to produce composites containing up to 2.3 wt.% of Gd. In the case of magnetic particles that are heavier than the LM, the

particles' surface can be coated with a LM-compatible material. Xiong *et al.* [74] reported the mixing of silica-coated Nickel nanoparticles into Ga and the EGaIn alloy in air. An alternative approach is to exploit the LM ability to internalize particles that it can wet [75]. To allow the start of the wetting, the oxide layer must be removed with a suitable chemical etchant. For example, He *et al.* [76] produced Galinstan droplets with Fe and NdFeB microparticles, after treating the LM surface with HCl and proceeding with mixing in air.

TABLE 2.2: Characteristics of reported Gallium-based magnetic liquid metals

Liquid metal	Magnetic material (wt.%)	Particle size	Particle treatment	Type of structure	Production method	References
Galinstan	Gd $(0.2\% - 2.3\%)$	$425\,\mu\mathrm{m}$	none	fluid	Mehanical alloying in a N_2 atmosphere	[17]
	Fe $(-)$	$6\,\mu\mathrm{m}$	none	droplets	LM surface treatment with HCl and 5 min stirring of the mixture in air	[76]
	NdFeB $(-)$	$8\,\mu\mathrm{m}$ and $15\,\mu\mathrm{m}$	none	droplets		
Gallium	Fe (33%)	$9\,\mu\mathrm{m}$	none	fluid	no information	[77]
	Ni (33%)	$1\,\mu\mathrm{m}$	none	fluid		
	Ni (10%)	nanoparticles	SiO_2 coating	fluid	60 min stirring of the mixture in air	[74]
EGaIn	Ni $(5\%$ and $10\%)$	nanoparticles	SiO_2 coating	fluid		

2.3. Computer overheating solutions

The fast development of IT requires high performance computing. The spreading of cloud computing and the emergence of AI, to name a few, have undoubtedly impacted our life, but their impact in the technological evolution has been even more remarkable. [36] The need for faster processing speeds has established an ever-growing pressure in the computer components' industry. Current production trends involve the shrinkage of the transistor size to accommodate more transistors in the same chip area. This clearly enhances the number of operations performed, thus improving the computational capacity of the device. However, one cannot separate from the consequent power consumption and heat generation increase. [39, 78]

At the Central Processing Unit (CPU) level, overheating * events can be very harmful, causing considerable lifetime shortage, or even irreparable hardware damage. Computers can implement different strategies to reduce the CPU's temperature and prevent overheating. As it will be explored, these can be separated in two more general branches -

*State of the CPU where its temperature value reaches the maximum safe operating temperature [79].

software solutions and hardware solutions. On the one hand, software solutions are intrinsically related to modifications in the computer operation. On the other hand, hardware solutions are mostly linked to optimisation of the design of computer components or to the development of physical systems which can effectively dissipate the heat generated by integrated circuits.

2.3.1. Software solutions

When a CPU reaches an overheating state, the main software safety measures involve reducing the rate of operations executed by the processor, also known as throttling. For such, two mechanisms can be used: clock modulation and operating frequency adjustment. Clock modulation implies skipping some operating cycles, by temporarily turning off the processor clock, in order to reduce the activity of the CPU. Operating frequency adjustments force the processor to operate at its minimum frequency, during a time period that guarantees no overheating occurs immediately after returning to normal activity. [79, 80] Even though this throttling has a positive impact on the power dissipation, it increases the machine instruction execution time, which consequently worsens the performance of the CPU [81].

Software-wise, another alternative relies on predicting the occurrence of overheating events. Machine learning algorithms, based on the time evolution of the processor's temperature can be used for such. This allows the system to take some preventive actions, namely, a small anticipated operating frequency reduction. In multiprocessor systems, task migration from hotter nodes to colder ones is also possible. These actions can diminish the performance loss, in comparison to the previously mentioned ones. [79, 82]

Nevertheless, all the forementioned throttling strategies are associated to a decrease in the CPU operation rate. Therefore, to achieve the goal of maximum computing performance, they should not be applied. This reinforces the need for extra and effective hardware solutions.

2.3.2. Hardware solutions

Temperature regulation within computers is critical to maintain the temperature value of each component inside the optimum working temperature range and, therefore, achieve an efficient operation. Different means can be pursued. On the one hand, during the computer manufacturing, architecture designs and material choices are optimized to increase

the energy efficiency and the heat dissipation. On the other hand, additional systems can be added to promote device cooling. In these systems can coexist elements responsible for passive and active cooling, depending on whether they require or not further energy consumption to perform their cooling task, respectively. [83, 84]

2.3.2.1 Passive cooling

Passive cooling components are mainly employed to enhance the heat exchange between the computer hardware and the cooling fluid (air or a liquid, e.g.). To fulfill this goal, as will be explored in this section, different designs and structures were developed over the years. To further improve the heat transfer, usually, a thermally conductive paste is applied between these components and the cooled element.

Heat sink

A heat sink, as illustrated in Figure 2.3 (a), consists of a cooling block with extended surfaces which increase the surface area in contact with the fluid medium [83]. The main factors that affect the heat sink performance are the choice of material (its thermal conductivity) and the extruded surface design (shape, aspect ratio, spatial arrangement, etc.) [84]. In Figure 2.3 (b) are presented several heat sink design possibilities. The surface is designed to optimise the area in contact with the fluid. Some common shape designs include solid fins or hollow pipes. In general, the pipe geometry is an improvement in comparison to the fin one, since the hollow interior increases the area in contact with the fluid. [84] However, the performance enhancement does not compensate the complexity in the manufacturing process of hollow pipe structures. Therefore, the fin geometry ends up being more widely used.

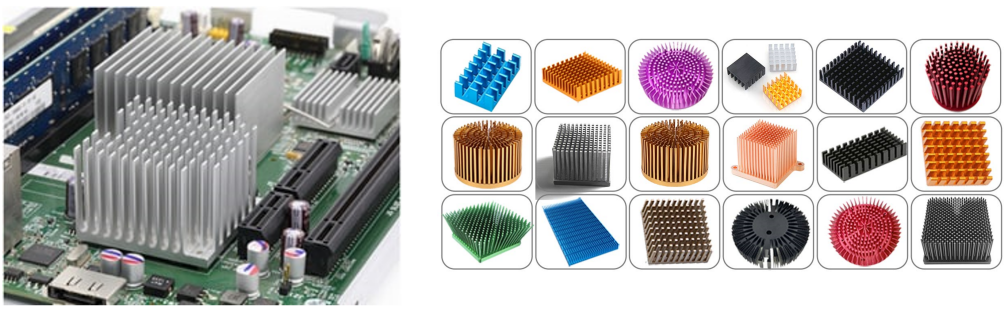

(a) (b)

FIGURE 2.3: Illustration of the heat sink designs used in computer cooling. (a) illustrates the implementation of different heat sink designs in the same motherboard, from Ref. [85]. (b) represents different heat sink designs commercially available, as promoted by Ref. [86].

Heat pipe

The heat pipe system contains a small amount of working fluid inside a fully-enclosed vacuum pipe. This fluid rests in the evaporation section, which is in thermal connection with the computer element to cool. As this element heats up, the fluid starts boiling, evaporates, and, eventually, due to the pressure gradient inside the pipe, it is transferred into the condensation section. This section is at a lower temperature to promote the condensation of the working fluid. As a consequence, the fluid returns to the evaporation section, through capillary action of the wick, at a temperature lower than the element's one, therefore cooling it down. [83, 84] This operation is depicted in Figure 2.4 (a).

The performance of this cooling system is mainly dependent on the properties of the working fluid, and on the temperature at the condensation section. Different strategies can be applied to decrease the temperature of this section. The most common one involves inserting it within a heat sink, as illustrated in Figure 2.4 (b), which is exposed to a fan's airflow. [78]

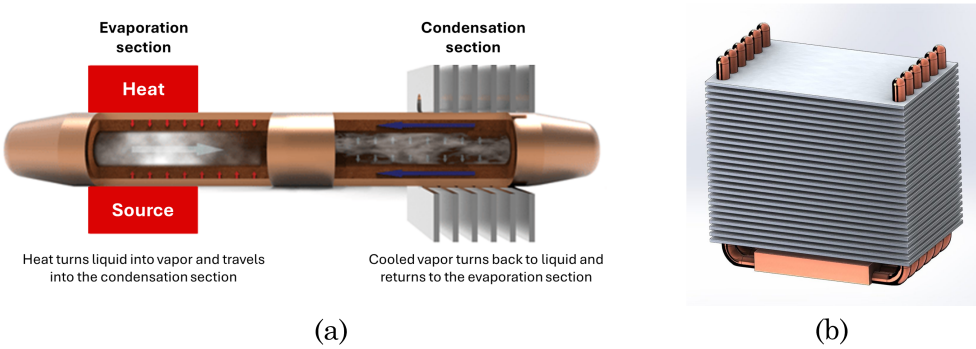

FIGURE 2.4: (a) Schematic illustration of the heat pipe operating principle, adapted from Ref. [87]. (b) Exemplification of a heat pipe combined with a heat sink system. Subfigure (b) was obtained from Ref. [88].

2.3.2.2 Active cooling

Active cooling components are developed to control the flux of heat inside a computer, in order to promote a proper heat dissipation. In spite of their additional power consumption, at the state of the art, the utilization of these components is essential to mitigate the nefarious effects induced by the heat produced at the computer processing and data storage units.

Among currently available active cooling methods, the two mostly used in today's computers are: air cooling and liquid cooling.

Air cooling

In air cooling, fans are powered on to pump air into cooled computer elements. The established airflow can indeed carry away some of the heat generated during the computer operation. [84] The airflow can be directed into the targeted computer component by placing the fan close to and facing that component. In current architectures, specifically, in laptops, the air cooling assembly is comprised by a fan, a heat sink, and a set of heat conducting pipes connected to a thermal block, which transmit heat away from the processor into the fan region. The schematic representation of this assembly and an example of a real structure are depicted in Figures 2.5 (a) and (b), respectively. This design not only facilitates the development of more compact devices, but also offers the possibility to cool different elements at once.

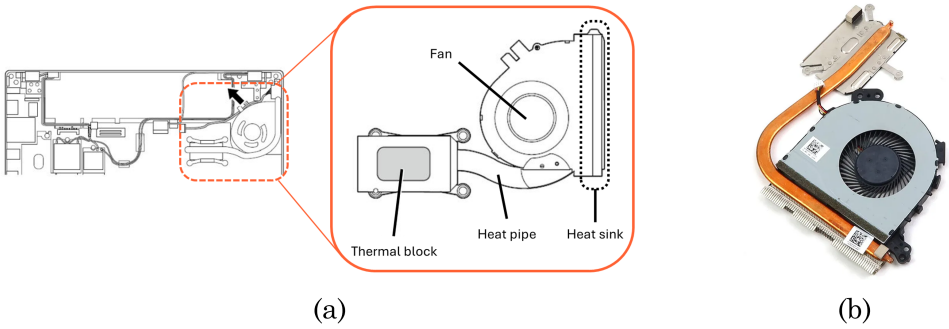

FIGURE 2.5: (a) Schematic illustration of the typical implementation of an air cooling system in a Lenovo ThinkPad X270 laptop, with a zoom-in of the cooling system. This figure was adapted from Ref. [89]. (b) Exemplification of the air cooling system used in a Lenovo IdeaPad laptop, comprising: fan, heat sink, heat pipe and thermal block. [90]

Liquid cooling

Liquid cooling systems benefit from the active flow of fluids to draw heat away from the computer hardware to the outside of the system. Actually, one can benefit from the working fluid guidance through pipes to develop architectures which simultaneously cool down several electronic components [83]. However, these systems need to be wisely engineered, since their performance is strongly dependent on the fluid's flow rate [78]. In addition, to assure a safe initiation and proper working conditions, the used coolants should have solidification and boiling points outside the components' working temperature range (typically from $0\,^{\circ}\mathrm{C}$ to $100\,^{\circ}\mathrm{C}$) [39].

A well-established liquid cooling system relies on the forced flowing of convective water. In Figure 2.6 (a), is schematically illustrated a water cooling system, constituted by:

a radiator, where the fluid is cooled, which is exposed to a constant airflow promoted by a fan; water guiding pipes; and a heat exchanger, where the heat generated by the cooled computer component is absorbed by water. In fact, water-based liquid cooling is an improvement to air cooling by more than a factor of 10 in the convective heat transfer coefficient [39]. Still, in many cooling systems, to compensate the low thermal conductivity of water, the heat exchanger is comprised by micro-channels, which optimise the heat transfer from the heat source [39]. Another alternative relies on considering higher thermal conductive fluids, such as oil-based ones or LMs. In fact, the usage of LMs can be very promising. In comparison to commonly used fluids, LMs have a substantially higher thermal conductivity, as depicted in Table 2.1. Therefore, their incorporation can result in an improvement on the heat transfer through the fluid [39, 72, 91]. Furthermore, their higher surface tension can reduce drastically the leakage probability, which is one of the main disadvantages of liquid cooling systems, since the leaked coolant could damage any electronic components it comes in contact with.

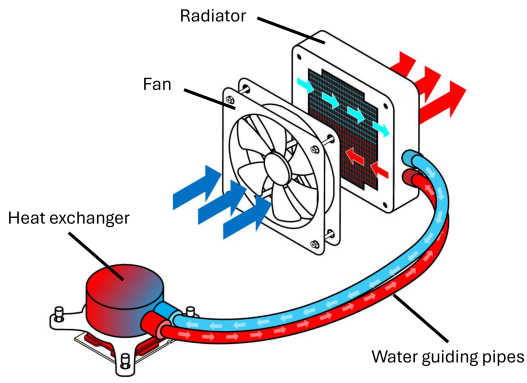

FIGURE 2.6: Schematic illustration of a common water-based liquid cooling system, adapted from Ref. [92].

2.3.3. Overview on current cooling systems

First of all, one needs to be aware that none of the discussed cooling methods is self-sufficient [93]. As a consequence, the cooling systems inside computers are comprised by both passive and active cooling elements. At the moment, in personal laptops, the active heat sink - heat sink exposed to a pumping airflow - is the most widely used method. Common strategies to enhance the cooling performance of these systems involve oversizing the cooling elements or considering hybrid solutions [94]. In passive cooling, the combination of a heat sink with a heat pipe system, as the one illustrated in Figure 2.4 (b), has proven to achieve a better cooling performance, for the same airflow rate, than any of

its constituents isolated [84]. Consequently, this enables an overall power consumption decrease. In active cooling, the combination of air cooling with liquid cooling is already employed in higher performance computing.

Despite their undeniable contribution to heat dissipation at the CPU and memory level, current hardware solutions will prove ineffective in meeting the upcoming thermal challenges. In the next few years, the maximum chip heat flux is expected to exceed $500\,\mathrm{W\,cm^{-2}}$, with localized heat fluxes possibly reaching values of $1\,\mathrm{kW\,cm^{-2}}$ [6]. Looking at the state of the art for active cooling, the relatively low heat transfer coefficient (HTC) for air cooling ($0.001 - 0.01\ \mathrm{W\,cm^{-2}\,K^{-1}}$ [6]) requires temperature differences from $100\,^{\circ}\mathrm{C}$ to $1000\,^{\circ}\mathrm{C}$ to achieve a heat flux of $1\,\mathrm{W\,cm^{-2}}$. For liquid cooling, HTC values range between $0.01 - 1\,\mathrm{W\,cm^{-2}\,K^{-1}}$ [6], allowing the temperature difference required to achieve a heat flux of $1\,\mathrm{W\,cm^{-2}}$ to be significantly reduced to $1\,^{\circ}\mathrm{C}$. However, to meet the predicted demanding chip heat fluxes, current solutions would require a significant increase in the heat transfer area or in the working fluid flow, which would ultimately lead to an unsustainable oversizing of their components, which would further increase their typical operating noise and vibration. This reinforces the need for alternative high performance thermal management methods.

In this work, a liquid cooling method that incorporates a magnetic liquid metal into a MAFTS prototype is proposed. The LM (Galinstan) matrix usage helps overcoming the thermal conductivity issue typically associated with liquid cooling. Moreover, the magnetic liquid metal can be remotely controlled through application of external magnetic fields, thus offering a wireless, noise-free, and vibration-free cooling alternative, with a low leakage probability, due to the high surface tension of the LM.

3. Experimental characterization techniques

This chapter will present the several techniques used to inspect the morphological, chemical, structural and magnetic properties of the materials produced in the scope of this thesis. These materials can be separated into three groups with different physical and magnetic properties: ferromagnetic particles, liquid metals and magnetic liquid metals. In Figure 3.1 it is summarized the techniques considered for the characterization of each of these groups.

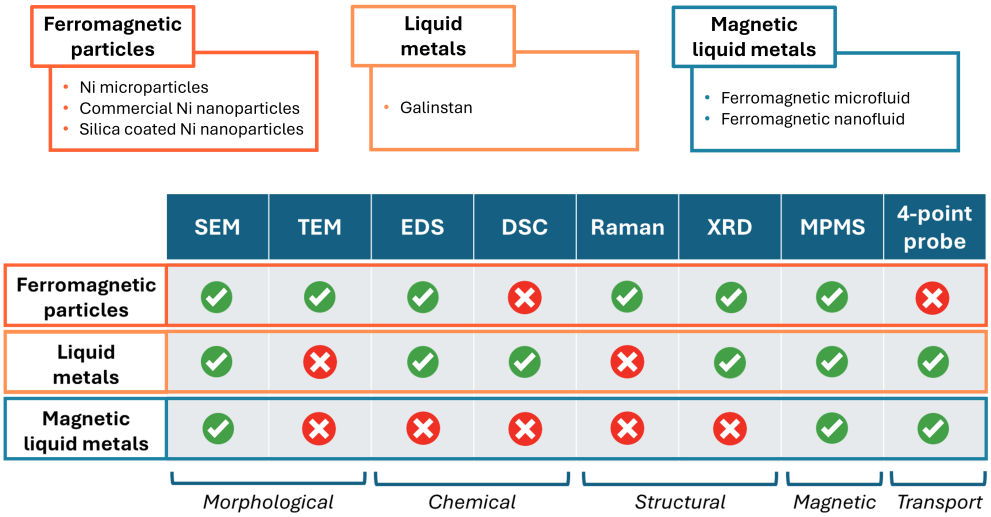

FIGURE 3.1: Diagram identification of the techniques considered for characterization of the morphological, chemical, structural, magnetic and transport properties of each of three group materials (ferromagnetic particles, liquid metals and magnetic liquid metals) produced throughout this thesis. For each entry of the table, the green circled tick or the red circled cross identifies if the technique of that column was or not used to characterize at least one element from the group of materials of that line, respectively. In the table: SEM, Scanning Electron Microscopy; TEM, Transmission Electron Microscopy; EDS, Energy Dispersive X-ray Spectroscopy; DSC, Differential Scanning Calorimetry; XRD, X-Ray Diffraction; MPMS, Magnetic Properties Measurement System.

3.1. Morphological and chemical characterization

3.1.1. Electron Microscopy

To analyze their morphology and chemical composition, the samples were inspected by room-temperature Scanning Electron Microscopy (SEM) combined with Energy Dispersive X-ray Spectroscopy (EDS). Additionally, the morphology of the ferromagnetic particles was also analyzed through room-temperature Transmission Electron Microscopy

(TEM). These techniques are based on electron-matter interaction, under high vacuum conditions. Depending on the type of interaction with the sample, photons or electrons with different energies are generated, which are collected by distinct detectors. Each acquired signal acquaints specific information about the sample.

Scanning Electron Microscopy (SEM)

In SEM measurements, an image is generated from the collection of the electrons emitted from the interaction of the incident electron beam with the sample. The emitted electrons exhibit differing energies, and can provide various insights about the sample. The secondary electrons (SE) are generated through the energy transfer from the beam to the specimen, which results in the ejection of an electron from the atom's outer shells. These low-energy SE are highly sensitive to changes in the sample topography. The backscattered electrons (BSE) arise from elastic scattering with the nuclei of the sample's atoms. The intensity of the BSE signal is strongly influenced by the atomic number of the elements in the sample, thereby rendering BSE particularly useful for identifying variations in chemical composition along the sample.

In the specific case of ferromagnetic particles samples, the generated images were analyzed using the software ImageJ to determine their mean particle size from the fitting of their particle size distribution.

Energy Dispersive X-ray Spectroscopy (EDS)

In EDS measurements, the sample irradiation with an high-energy focused electron beam ejects electrons from their atomic shells, creating holes which are then filled with higher level electrons. This relaxation process is accompanied by the emission of X-ray radiation. Since each chemical element has a characteristic X-ray signature, by analyzing this signal, one can quantify/identify the composition of the sample in a specific region.

Experimental details: The SEM and EDS characterizations were performed at the Materials Centre from the University of Porto (CEMUP). The SEM/EDS setup used was FEI Quanta 400FEG ESEM / EDAX Genesis X4M.

Transmission Electron Microscopy (TEM)

In TEM measurements, the electrons transmitted and diffracted through the sample are collected to create an image. Due to the shorter wavelength (λ) of these electrons, TEM images offer a greater spatial resolution than those obtained by SEM.

Experimental details: The TEM measurements were performed at the i3S Institute, in Porto, using the Transmission Electron Microscope Jeol JEM 1400.

3.1.2. Differential Scanning Calorimetry (DSC)

The Differential Scanning Calorimetry (DSC) technique was used to quantify the heat exchanged by the Galinstan samples, as their temperature was cycled between a specific interval. The LM samples absorb and release significant amounts of heat during their melting and solidification transitions, which can be readily identified in the obtained DSC scans from the surging endothermic and exothermic peaks, respectively. By comparing the temperature values at which these peaks onset with previously reported values obtained using this thermal analysis technique, it is possible to infer on the chemical composition of the analyzed samples.

Experimental details: The DSC measurements were done at the Institute for Energy Technology (IFE), in Norway. A TA Instruments® DSC25 calorimeter was used, together with alumina sample holders. The samples' temperature was cycled between $-100\,^{\circ}\mathrm{C}$ and $100\,^{\circ}\mathrm{C}$ at a constant rate of $10\,^{\circ}\mathrm{C}/\mathrm{min}$.

3.2. Structural characterization

3.2.1. Raman Spectroscopy

To evaluate the chemical structure of ferromagnetic powder samples, they were inspected by room-temperature Raman Spectroscopy. This technique examines the phonon vibrational modes produced between neighbouring atoms. Since each Raman mode is related to specific chemical bondings and coordinations, this technique provides vital information about the composition of the probing area. Thus, by comparing Raman spectra obtained at different locations within the same sample, one can assess its homogeneity. In this context, this technique was utilized during this work to ascertain the presence of silica in the synthesized silica-coated Ni nanoparticles.

Experimental details: The Raman spectra were recorded at IFIMUP with a Renishaw inVia Qontor spectrometer, in a backscattering geometry, using the $50\times$ objective lens of a Leica microscope. A 532 nm He-Ne laser line was used for excitation at $5\,\%$ and $10\,\%$ power. These conditions minimize fluorescencent contributions from silica in some samples. Each measurement comprised three $10\,\mathrm{s}$ scans for wavenumbers smaller than $3000\,\mathrm{cm}^{-1}$, to prevent sample oxidation due to in-situ laser heating.

3.2.2. X-Ray Diffraction (XRD)

The crystalline structure of different samples was evaluated through room-temperature X-Ray Diffraction (XRD). As X-rays interact with atoms in a crystal, they undergo diffraction, due to reflections of the atomic planes. As described by Bragg's law (Equation 3.1), constructive interference occurs when the path difference between two incident beams is an integer multiply of the wavelength (λ) [95].

$$\lambda = 2d_{hkl}\sin\theta \tag{3.1}$$

The constructive and destructive interference of the diffracted X-rays creates a diffraction pattern. This pattern contains information about the crystal structure of the sample. From the analysis of the X-ray diffractograms, through LeBail refinements, it was possible to identify and quantify the percentage of crystalline phases present in each sample.

Experimental details: The XRD measurements proceeded at IFIMUP using a Rigaku SmartLab Diffractometer ($\mathrm{Cu-k}\ \alpha$, $\lambda = 1.5406$ Å, $45\,\mathrm{kV}$ and $200\,\mathrm{mA}$) in a Bragg-Brentano $\theta - \theta$ geometry. For powder measurements, the sample was placed on top of a $\mathrm{Si}\,(100)$ substrate. For liquid measurements, a glass slide was covered with a thin sheet of the sample. The powder and liquid data were acquired with a $0.01°$ step for the $2\theta \in [30°, 110°]$ interval and for the $2\theta \in [10°, 85°]$ interval, respectively.

3.3. Magnetic characterization

The magnetization of the samples produced throughout this thesis work (ferromagnetic particles, LMs and magnetic liquid metals) was measured using a Superconducting Quantum Interference Device (SQUID) magnetometer. In this system, the sample is inductively coupled to the magnetic field, generating a current as it moves through the set of pick-up coils. These coils are inductively coupled through an input transformer to a DC SQUID, which essentially functions as an extremely sensitive current-to-voltage converter. The measured voltage is then digitally converted into the sample's magnetic moment, thereby constituting an indirect measurement of the sample's magnetization.

Experimental details: The Magnetic Properties Measurement System 3 (MPMS 3) SQUID Magnetometer from Quantum Design, available at IFIMUP, was used to study the magnetic behavior of every sample at different temperature values. In the magnetization versus magnetic field characterizations, the magnetization of the sample was measured for different magnetic fields, ranging from $-5\,\mathrm{T}$ to $5\,\mathrm{T}$, at a fixed temperature. The isofield magnetization as a function of temperature curves were measured at a field strength of $0.1\,\mathrm{T}$ and temperature rate of $5\,\mathrm{K/min}$.

For each group of samples, different protocols were considered. Still, all of them included at least one magnetization versus magnetic field $\left(M\left(H\right)\right)$ characterization. From this characterization, the saturation magnetization and the coercive field of the measured samples, at the measured temperature, were determined.

For the ferromagnetic particles, the $M\left(H\right)$ curves were acquired in the VSM mode at the temperature values of $10\,\mathrm{K}$ and $300\,\mathrm{K}$, using a brass sample holder. The geometric effects of these measurements were corrected according to the protocol proposed by Amorim *et al.* [96].

For the magnetic and non-magnetic liquid metal samples, the magnetization was measured in the DC mode. Otherwise, the fluid's movement inside the sample holder would invalidate the initial centering process, which is crucial for the voltage to magnetic moment conversion. In the case of the liquid metal (Galinstan) sample, only a $M\left(H\right)$ characterization at $300\,\mathrm{K}$ was performed. The magnetization of Galinstan is smaller than that of the Teflon liquid sample holder provided by Quantum Design [97]. Therefore, to measure Galinstan's magnetization, an alternative sample preparation was considered. As depicted in Figure 3.2, a gelatin capsule half-filled with Galinstan was wrapped with teflon

tape and inserted inside a punched plastic straw. In the case of the magnetic liquid metals, the magnetic susceptibility of the embedded magnetic material exceeds that of the liquid sample holder, enabling its use during the magnetization measurements. For this group of samples, $M(H)$ curves were acquired at the temperature values of $10\,\mathrm{K}$ and $300\,\mathrm{K}$. Additionally, their isofield magnetization as a function of temperature $(M(T))$ curves were measured, during cooling and heating, for temperature values ranging from $350\,\mathrm{K}$ to $5\,\mathrm{K}$ and from $225\,\mathrm{K}$ to $350\,\mathrm{K}$, respectively. This allowed the identification of some sample's transition temperatures.

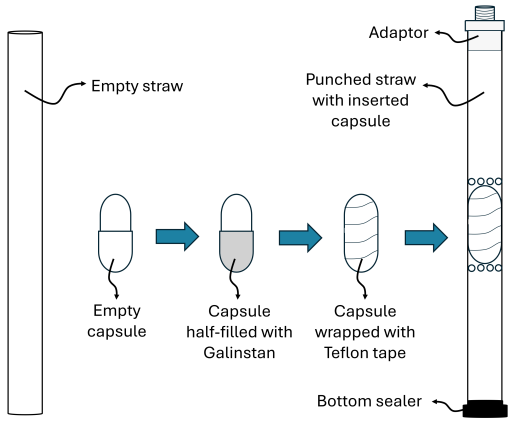

FIGURE 3.2: Schematic illustration of the preparation steps for the magnetization measurements of Galinstan samples in the MPMS 3 SQUID Magnetometer.

3.4. Transport properties characterization

The four-point probe technique was used to measure the electrical resistivity (ρ) of liquid metal and magnetic liquid metal samples. This technique is particularly well-suited to metals (which feature a low ρ), as it circumvents the resistance of the measuring equipment, in contrast to the two-point probe technique [98]. Despite being more common for measuring the electronic properties of solid samples, this technique has already been utilized for liquid metals, as reported in [38, 99].

Figure 3.3 (a) schematically illustrates the setup considered for this measurement technique. There, a liquid metal-based sample is injected into a channel with length $l = 3\,\mathrm{cm}$, width $w = 3.5\,\mathrm{mm}$ and height $h = 3.5\,\mathrm{mm}$. In Figures 3.3 (b) and (c) are depicted the channel filled with liquid metal without and with the connections established, respectively.

A current source (Aim TTi EX355P Programmable Bench Power Supply) forces an electrical current (I) to flow through the sample. The value of I is measured using the source's incorporated ammeter. A multimeter (Agilent 34405A 5 1/2 digit multimeter) is used as

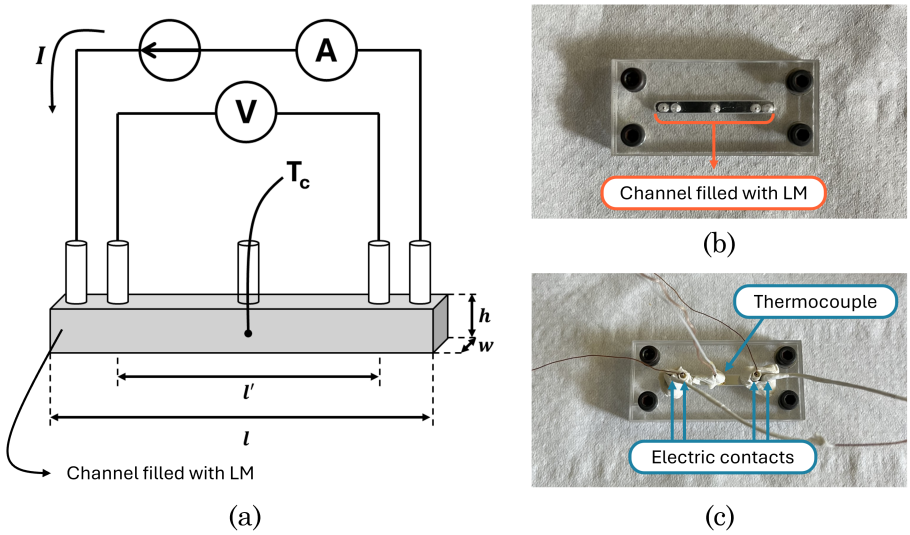

FIGURE 3.3: (a) Schematic illustration of the setup considered for the measurement of the transport properties of the liquid metal-based samples. (b) and (c) Illustration of the channel filled with LM without and with the connections established, respectively.

voltmeter to measure the voltage (V) within a sample's section with length $l' = 2.03\,\mathrm{cm}$. Additionally, the temperature at the center of the sample (T_c) is monitored using a thermocouple (TC), which is covered with GE-varnish to protect it from being alloyed with the liquid metal. This TC is connected to a TC-08 thermocouple data logger (Pico Technology). The data acquisition is controlled by homemade programs.

From the measurement of V as a function of I, one can extrapolate the value of ρ, by considering Ohm's law:

$$V = \rho \frac{l'}{w\,h} I\,. \tag{3.2}$$

Considering the Wiedemann-Franz law approximation (Equation 3.3), it is possible to determine the thermal conductivity (λ) of liquid metals, from the measurement of their ρ, with an accuracy of $1 - 10\%$ [100]. In Equation 3.3, $L_0 = \frac{1}{3}\left(\frac{\pi k_B}{e}\right)^2$, where k_B is the Boltzmann constant, and e is the elementary charge value.

$$\lambda \approx \frac{L_0}{\rho}\, T_c \tag{3.3}$$

Experimental details: The electrical resistivity measurements were conducted with a $100\,\mathrm{mA}$ step for the $I \in [100, 700]\ \mathrm{mA}$ interval. The upper current limit was selected to prevent a significant increase in T_c within the time frame of the experiments. The measurements were conducted in two modes: a stationary mode, wherein I was maintained at the desired value for approximately $100\,\mathrm{s}$ before being deactivated; and a sweep mode, wherein the value of I was increased in $100\,\mathrm{s}$-long steps. The objective was to obtain the greatest amount of data for a given (I, V, T_c) point.

4. Galinstan-based magnetic liquid metals: production and characterization

In the present work, two different magnetic liquid metals, which synergistically combine the excellent heat conductive properties of Galinstan with the ferromagnetism of Ni micro (ferromagnetic microfluid) and nanoparticles (ferromagnetic nanofluid), were fabricated. Before producing the ferromagnetic fluids, the liquid metal and the magnetic particles were independently synthesized and characterized. In this chapter, for each material, the methods used in their production will be presented, and their characterization results will be discussed.

4.1. Galinstan

4.1.1. Production method

Galinstan was synthesized using Ga, In and Sn purchased from Alfa Aesar (Ga, In) and Thermo Scientific (Sn) with $99.99\,\%$ purity. The setup used to produce the Galinstan is depicted in Figure 4.1 (a). The fabrication procedure followed the one reported by Castro *et al.* [17].

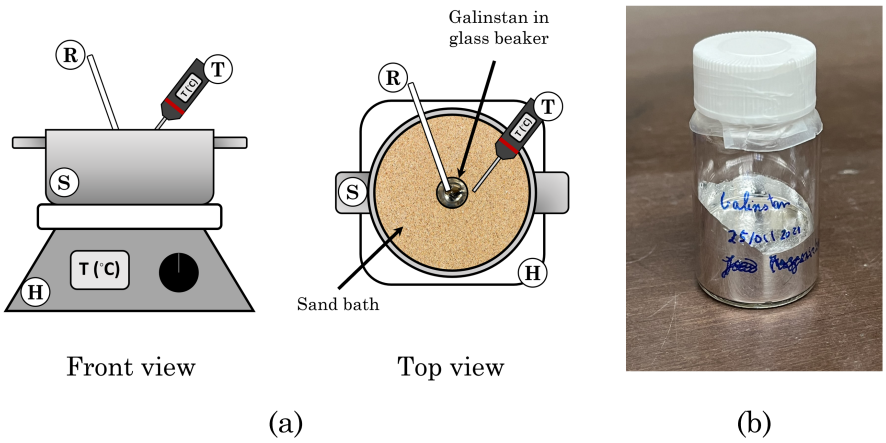

FIGURE 4.1: (a) Illustration of the setup used to produce Galinstan, where: H, hot plate; S, steel pan; R, glass rod; T, digital thermometer. (b) Illustration of Galinstan's storage, after production, in a glass container.

The first step in fabricating the Ga/In/Sn $(68:22:10)$ wt.% (target composition) alloy was to determine the target batch mass. Subsequently, the mass of each precursor was

calculated based on the desired final composition. After being weighed on a Kern ® ABT-5M analytical balance, the reagents were transferred to a glass beaker. To synthesize the alloy, the beaker was heated up in a sand bath within a steel pan, using a hot plate as the heat source. The temperature of the hot plate was kept at $300\,^{\circ}\mathrm{C}$, and the temperature of the sand bath was monitored with a digital thermometer, placed close to the beaker. During the melting process, the mixture was thoroughly mixed with a glass rod until becoming fully liquid. This procedure lasted one hour. During that period of time, the thermometer's temperature started at the room temperature value and finished slightly bellow $150\,^{\circ}\mathrm{C}$. Even though these values are lower than the highest melting point of the precursors ($231\,^{\circ}\mathrm{C}$ for Sn [101]), the mixture was already molten. This can be explained by the dissolution of Indium and Tin within the liquid Gallium [38].

Finally, the mixture was cooled down to room temperature. Afterwards, the Galinstan was transferred to a small glass container (Figure 4.1 (b)), using a plastic pipette, with the special care to avoid transferring the oxide layer formed in the surface of the liquid metal.

4.1.2. Characterization

Chemical characterization

The chemical composition of Galinstan was estimated through EDS. The measurements were conducted on three different zones of the same Galinstan sample. The element wt.% distribution results are summarized in Table 4.1. The average value yielded an experimental Ga/In/Sn composition of $(65.5 : 23.7 : 10.8)$ wt.%, which exhibited a slight deviation from the target Ga/In/Sn $(68 : 22 : 10)$ wt.% composition.

TABLE 4.1: Element wt.% distribution in each zone of the Galinstan EDS measurements

Zone	Element wt.%		
	Ga	In	Sn
1	66.0	23.3	10.7
2	65.9	23.6	10.5
3	64.6	24.1	11.3

In Figure 4.2 is depicted the DSC scan of one Galinstan sample, in the temperature interval from $-100\,^{\circ}\mathrm{C}$ to $100\,^{\circ}\mathrm{C}$. The endothermic peak during heating (whose onset occurs at $P1$) signals the melting of the alloy. The three exothermic peaks during cooling (with onsets at $P2$, $P3$ and $P4$) are indicative of a multiple step solidification process. The temperatures at which these peaks onset, as well as the associated reported values, are

summarized in Table 4.2. From Figure 4.2, it is also notorious the supercooling behavior of the alloy, with clearly distinct melting and solidification temperatures, as previously reported in [17, 20, 48, 57].

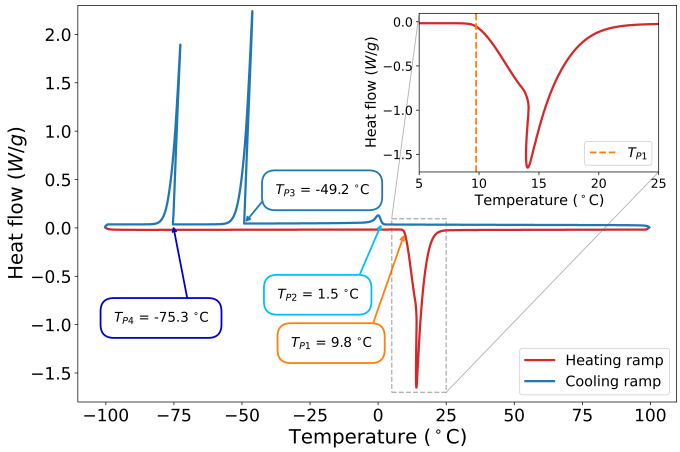

FIGURE 4.2: Thermogram obtained for a Galinstan sample with the endothermic $(P1)$ and exothermic $(P2, P3, P4)$ transitions identified. The inset corresponds to a zoom-in of the melting transition associated to $P1$.

TABLE 4.2: Experimental and reported values for the endothermic ($P1$) and exothermic ($P2$, $P3$ and $P4$) peaks of Galinstan's DSC thermogram

Peak	Experimental (°C)	Reported (°C)	References
$P1$	9.8	$[10.6, 13.2]$	[17, 20, 57]
$P2$	1.5	–	–
$P3$	-49.2	$[-30.5, -26.4]$	[20, 57]
$P4$	-75.3	$[-38.5, -35.8]$	[20, 57]

Regarding the melting of the alloy, the obtained melting temperature, $T_{P1} = 9.8\,°\mathrm{C}\ (282.95\,\mathrm{K})$ is slightly lower than previously documented values, which range from $10.6\,°\mathrm{C}$ to $13.2\,°\mathrm{C}$ [17, 20, 57]. The inset in Figure 4.2 illustrates the zoom-in of this phase transition, showing that it rather corresponds to the superposition of two endothermic peaks. This phenomenon has already been reported in the literature, with the appearance not only of overlapped peaks [20], but also of a completely bimodal peak structure [57], when considering a lower heating rate.

On cooling, the observed stepwise solidification process is expected for the Galinstan sample, since it is characteristic of alloys made from materials with significantly different melting points [57]. The peak $P2$ which onsets at $T_{P2} = 1.5\,°\mathrm{C}\ (274.65\,\mathrm{K})$ can be attributed to a small-scale solidification process, specifically to the nucleation of $\mathrm{Sn_2}$-like clusters [20]. The peaks $P3$ and $P4$, whose onset occur at $T_{P3} = -49.2\,°\mathrm{C}\ (223.95\,\mathrm{K})$ and $T_{P4} = -75.3\,°\mathrm{C}\ (197.85\,\mathrm{K})$, respectively, are indicative of the solidification of different metal phases at different temperatures. Still, these phase change temperatures are

much lower than already documented ones. While for $P3$ the reported values lie within $-30.5\,^{\circ}\mathrm{C}$ and $-26.4\,^{\circ}\mathrm{C}$, for $P4$ they can range between $-38.5\,^{\circ}\mathrm{C}$ and $-35.8\,^{\circ}\mathrm{C}$ [20, 57]. This deviation can be explained by the contribution of the Ga_2O_3 nanometer-thick layer that forms around Galinstan as it makes contact with air [46]. This oxide layer works as a barrier to the heterogeneous nucleation observed during solidification, which enhances the supercooling effect of the sample [102].

Structural characterization

In Figure 4.3 (a) is depicted the room-temperature X-ray diffractogram of the Galinstan, with 2θ ranging from 10° to 85°. The broad diffraction peaks evidenced in this diffractogram illustrate the expected low crystalline nature of the LM sample. The XRD diffractogram shows a prominent peak at $2\theta = 34.6^{\circ}$ with a small shoulder centered at $2\theta = 44^{\circ}$, and a less pronounced peak at $2\theta = 66.1^{\circ}$. This XRD profile is similar to the one reported by Wang *et al.* [103] (illustrated in Figure 4.3 (b)). The latter was obtained for a Ga liquid thin film sample at a temperature of $50\,^{\circ}\mathrm{C}$. In comparison to Figure 4.3 (a), in Figure 4.3 (b), the diffraction peaks positions are slightly shifted to the right. This can be simply related to different zero point shifts. Nevertheless, being aware that the surface of both samples instantly oxidizes under ambient conditions, the similarity between their diffraction peaks suggests that the measured XRD diffractogram must be representative of the thin oxide layer of the Galinstan, which is mostly composed by Gallium oxides [44, 58, 102].

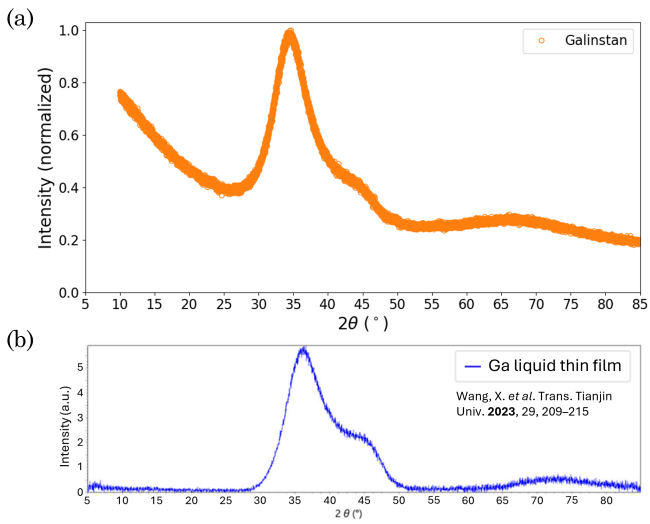

FIGURE 4.3: (a) X-ray diffractogram of a Galinstan sample, obtained at room temperature. (b) X-ray diffractogram of a Gallium thin film sample, obtained at $50\,^{\circ}\mathrm{C}$. This subfigure was adapted from Ref. [103].

Magnetic characterization

The magnetization curve of the Galinstan, at a fixed temperature of $300\,\mathrm{K}$, is depicted in Figure 4.4. The linear response of the fluid, for higher magnetic field strengths, illustrates its diamagnetic behavior. From the slope obtained after fitting the data to a linear regression, it was possible to calculate an experimental mass magnetic susceptibility of $-6.23 \times 10^{-10}\,\mathrm{m^3kg^{-1}}$. To the best of our knowledge, there are no reported values for Galinstan's magnetic susceptibility. Nevertheless, taking into account the Ga/In/Sn wt.% composition in our EDS measurements and the mass magnetic susceptibility of each of Galinstan's constituents (Ga, In and Sn), it is feasible to estimate a susceptibility of $-3.38 \times 10^{-10}\,\mathrm{m^3kg^{-1}}$ for this LM alloy. The absolute experimental value exceeded the estimated one, since the diamagnetic contribution of the sample holder to the measured magnetic moment was not removed in the former.

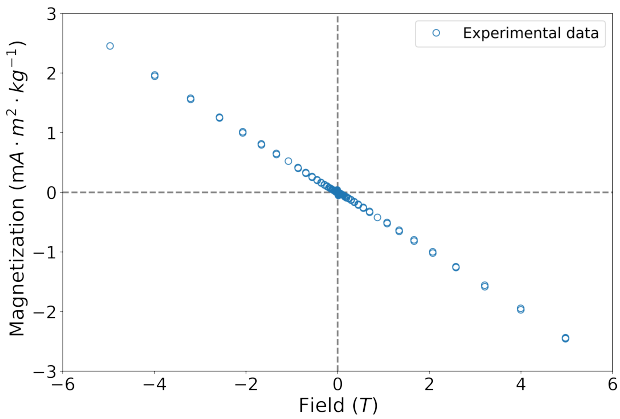

FIGURE 4.4: Magnetic response of the Galinstan fluid to varying magnetic fields within the range $[-5, 5]\ \mathrm{T}$, at $300\,\mathrm{K}$.

Transport properties characterization

The ρ measurement results obtained in the stationary and sweep modes are depicted in Figures 4.5 (a) and (b). In both figures, each data point of the V and temperature (T) versus I plots, corresponds to the average value of V or T over the respective electric current step. The errorbars in these plots correspond to the standard deviation of V or T over the corresponding electric current step.

Concerning the $V(I)$ measurements, it is observed a linear behavior, as expected from Ohm's law (Equation 3.2). As suggested from this law, from the slope obtained after fitting the data to a linear regression, it was possible to calculate the electrical resistivity associated to each measurement mode. In the stationary mode, a ρ value of $(2.851 \pm 0.004) \times$

$10^{-7}\,\Omega\mathrm{m}$ was obtained. In the sweep mode, ρ took a value of $(2.849 \pm 0.004) \times 10^{-7}\,\Omega\mathrm{m}$. The values reported here are slightly lower than those reported by Handschuh-Wang *et al.* [48], which lie within the range $\rho \in [2.89, 3.04] \times 10^{-7}\,\Omega\mathrm{m}$.

Regarding the $T(I)$ measurements, the increased standard deviation for the higher current value of $700\,\mathrm{mA}$ indicates the greater effect of the Joule heating on the temperature value. In both measurement modes, the average temperature value $\left(\overline{T}\right)$ was calculated. Combining the obtained value for $\overline{T}$ with the expression of the Wiedemann-Franz law (Equation 3.3), the λ of the sample was determined. In the stationary mode, it was calculated a value of $(25.48 \pm 0.04)\ \mathrm{W\,m^{-1}\,K^{-1}}$ for λ. In the sweep mode, an experimental λ of $(25.51 \pm 0.03)\ \mathrm{W\,m^{-1}\,K^{-1}}$ was obtained. The calculated values are slightly higher than those previously reported ($\lambda \in [23.03, 25.25]\ \mathrm{W\,m^{-1}\,K^{-1}}$ [17, 19–21, 38, 48]), as depicted in Table 2.1. This suggests that the produced LM exhibits a higher concentration of In than the documented alloys, given that of the three elements that constitute Galinstan (Ga, In and Sn), Indium is the most thermally conductive [48]. This finding aligns with the outcomes of the EDS measurements of Galinstan.

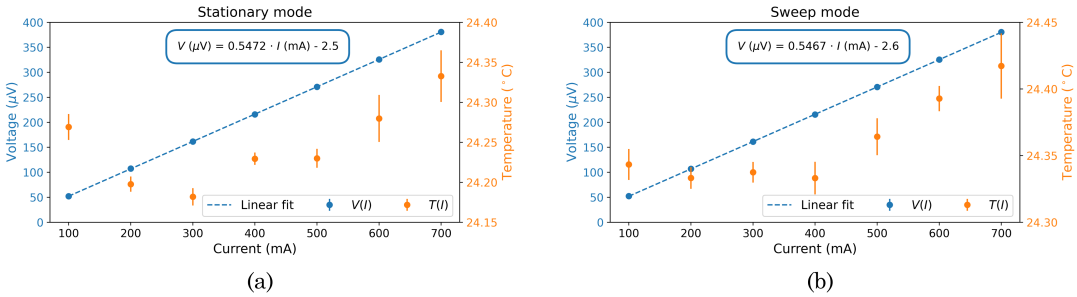

FIGURE 4.5: Electric resistivity measurements obtained for a Galinstan sample in the stationary mode (a) and in the sweep mode (b).

4.2. Nickel microparticles

4.2.1. Production method

As illustrated in Figure 4.6, the production of the ferromagnetic Ni microparticles started with the mechanical grinding of a Ni bulk piece ($99.9+$ % purity, purchased from Alfa Aesar) with a steel file. To further reduce the particle size, the grinding was followed by two hours of orbital ball milling in a Mini-Mill PULVERISETTE 23. The milling was performed at a vertically oscillating frequency of $50\ \mathrm{Hz}$, with zirconium oxide balls at a ball-to-powder mass ratio of $2.6:1$.

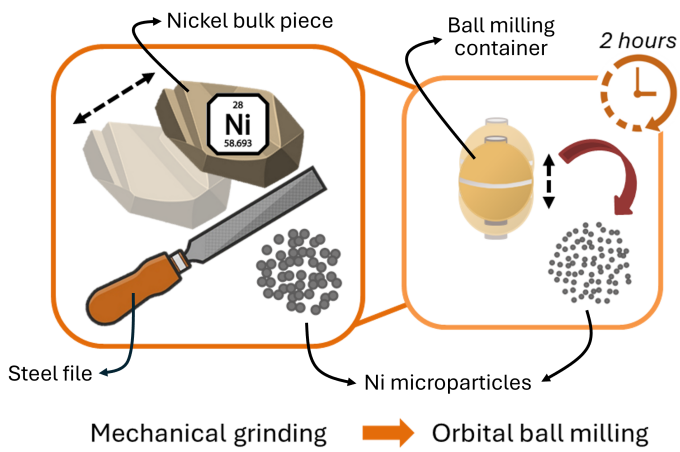

FIGURE 4.6: Illustration of the steps (mechanical grinding and orbital ball milling) considered in the production of the Ni microparticles.

4.2.2. Characterization

Morphological characterization

In Figure 4.7 is depicted the SEM image obtained to analyze the size and morphology of the produced Ni microparticles. It is possible to observe particles with an irregular shape and a broad particle size distribution. These characteristics are typically associated with top-down processes such as the ones used here [104, 105].

Using the software ImageJ, the size of each particle in the image (approximately 300 in total) was estimated from the measurement of their area, and the particle size histogram shown as inset in Figure 4.7 was obtained. This histogram illustrates the profile of the fitted size distribution, which follows a lognormal function, characteristic of particles that went through mechanical grinding and milling [104, 106]. From the parameters obtained after fitting the particle's size distribution, a mean particle size of $(16 \pm 8)\ \mu\mathrm{m}$ was estimated.

Structural characterization

In Figure 4.8 (a) is presented the room-temperature X-ray diffractogram of the Ni microparticles, ranging $2\theta = 30^\circ - 110^\circ$. The Bragg peaks evidenced in this diffractogram denote the polycrystalline nature of the produced powder. The observed peaks were indexed to the Ni structure, specifically at $2\theta = 44.5^\circ\ (111)$, $51.9^\circ\ (200)$, $76.4^\circ\ (220)$, $93.0^\circ\ (311)$ and $98.4^\circ\ (222)$. No additional phases were detected, showing that the mechanical grinding and ball milling did not modify the crystallographic structure. In this context, structural Le

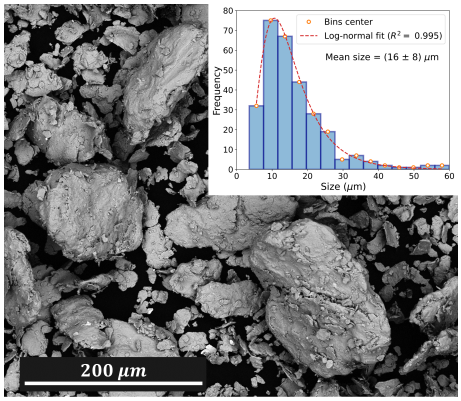

FIGURE 4.7: SEM top-view of the Ni powder with $500\times$ magnification and obtained in backscattered mode, and histogram of the corresponding particle size distribution (inset).

Bail refinements were carried out using the FullProf software [107]. The refinement considered a face centered cubic phase ($\mathrm{Fm\overline{3}m}$ space group), and yielded a lattice parameter of 3.5 Å and a unit cell volume of 43 Å^3, in accordance with Bradley *et al.* [108].

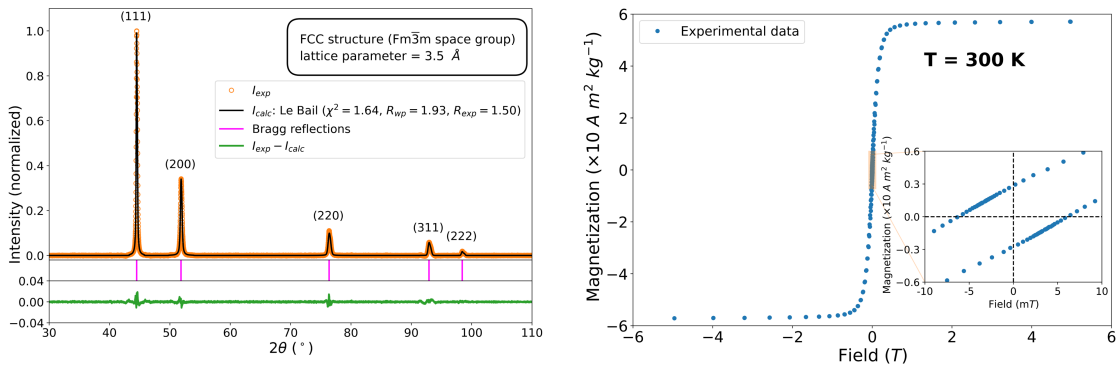

(a) (b)

FIGURE 4.8: (a) X-ray diffractogram of Ni microparticles showing the experimental (I_{exp}: orange circles) and the Le Bail refined (I_{calc}: black line) data, along with the expected Miller indexes for each reflection (vertical pink lines). The difference between the experimental and refined data $\left(I_{exp} - I_{calc}\right)$ is also represented by the green line. (b) Ferromagnetic response of the Ni microparticles to varying applied magnetic fields in the range $[-5, 5]$ T, at $300\,\mathrm{K}$. The inset corresponds to a zoom-in of the low-field range between $-10\,\mathrm{mT}$ and $10\,\mathrm{mT}$.

Magnetic characterization

The magnetization hysteresis curve at $300\,\mathrm{K}$ is represented in Figure 4.8 (b), demonstrating the ferromagnetic response of the Ni microparticles. From the experimental data it was possible to determine a saturation magnetization of $(57.1 \pm 0.2)\ \mathrm{Am^2kg^{-1}}$. This value is close to those reported by Crangle *et al.* [109] at $293\,\mathrm{K}$, which lie within the range of $54.3\,\mathrm{A\,m^2\,kg^{-1}}$ and $55.2\,\mathrm{A\,m^2\,kg^{-1}}$. Additionally, the microparticles show no exchange

bias, and have a coercive field of $6.3\,\mathrm{mT}$. This low coercivity not only favors their utilization in high frequency applications, due to their intrinsic smaller heat dissipation in each hysteretic cycle, but, most importantly, also reduces their probability of cluster formation.

4.3. Silica-coated Nickel nanoparticles

As indicated in Section 2.2, one common technique in the production of Ga-based magnetic LMs involves the surface coating of the magnetic particles, previously to their mixture with the LM. Specifically, coating the magnetic material (Ni) with silica $(\mathrm{SiO_2})$ improves the compatibility with the oxide layer of the LM, favouring its incorporation within the LM matrix [75]. Therefore, after acknowledging that the commercial Ni nanoparticles used throughout this work could not be embedded into the Galinstan, the decision to perform a silica coating on those particles was made.

4.3.1. Production method

The surface coating of the Ni nanoparticles ($99+\,\%$ purity, with an average particle size smaller than $100\,\mathrm{nm}$, purchased from Sigma Aldrich) was achieved through $\mathrm{SiO_2}$ deposition after the hydrolosis reaction of tetrathyl orthosilicate (TEOS) [$98\,\%\mathrm{w/w}$, purchased from Sigma Aldrich] in alkaline conditions. The synthesis procedure is schematically presented in Figure 4.9 (a), and was adapted from the ones followed by Xiong *et al.* [74], and by Dodbiba *et al.* [110], where they silica-coated Ni, and FeNbVB nanoparticles, respectively.

Before proceeding with the coating itself, the particles were dispersed in an Ethanol $(70\,\%\,\mathrm{v/v})$ and deionized (DI) water solution, as depicted in Figure 4.9 (b). Firstly, $300\,\mathrm{mg}$ of Ni nanopowder were weighed and added into a glass beaker with $50\,\mathrm{mL}$ of DI water. This mixture was stirred, and then sonicated during 35 minutes. Afterwards, the Ni and water dispersion was transferred into a round-bottom three-necked flask, and $360\,\mathrm{mL}$ of Ethanol were added into it. The obtained dispersion was placed in an ultrasonic bath during three hours. After each hour, the bath was cooled down with ice, to avoid particle oxidation due to heating.

To proceed with the silica coating of the Ni particles, the setup illustrated in Figure 4.9 (c) was considered. There, the mechanical stirrer was rotating at a speed of $700\,\mathrm{rpm}$, to minimize particle cluster formation, and the hot plate was set at a temperature of $50\,^{\circ}\mathrm{C}$, to decrease the time needed for silica deposition. The three-necked flask was placed

inside an oil bath to heat the mixture homogeneously. During the heating process, $3\,\mathrm{mL}$ plus 2 or 3 drops of Ammonia hydroxide ($28\,\%\,\mathrm{w/w}$, from Alfa Aesar) were added into the three-necked flask, in order to adjust the mixture's pH to slightly above 10 (as confirmed with a pH measuring tape). Moreover, a solution with $3\,\mathrm{mL}$ of TEOS and $57\,\mathrm{mL}$ of Ethanol $(96\,\%\,\mathrm{v/v})$ was slowly added into the flask using a burette. After finishing the addition of the TEOS solution, the oil bath was kept at a temperature of $50\,^{\circ}\mathrm{C}$ during one hour. Afterwards, the three-necked flask was removed from the oil bath, and cooled down to room temperature.

Finally, to eliminate unwanted silica clusters which are formed during the hydrolysis process, the particles were washed with Ethanol $(70\,\%\,\mathrm{v/v})$ and filtered as depicted in Figure 4.9 (d). In this filtering technique, a magnet is used to attract only the magnetic particles, thereby ensuring the disposal of the less magnetic material (more silica concentrated). This procedure was repeated 10 times. It is important to note that the longer each filtration takes, the greater will be the silica concentration, the mass of the final powder, and consequently the reaction yield. To complete the process, the particles were dried overnight in an oven at a temperature of $40\,^{\circ}\mathrm{C}$. The final powder was weighed to determine the reaction yield, which averaged between $60\,\%$ and $70\,\%$.

4.3.2. Characterization

During this discussion, to evaluate the influence of the silica coating on the properties of the magnetic material, the results from the characterization of the commercial Ni nanoparticles will also be included. Actually, the changes in the properties of the Ni particles were very similar for each of the 12 coatings produced. Therefore, except when specifically stated, the comparison with the commercial powder will be done considering the results from the coating number 10. In Appendix B are summarized the characterization results of all the fully-characterized batches.

Morphological characterization

In Figures 4.10 (a), (b) and (c) are depicted the SEM images obtained to analyze the size and morphology of the commercial Ni nanoparticles. The Figures 4.10 (b) and (c) correspond to a zoom-in of the zone Z1 identified in Figure 4.10 (a), and were acquired in backscattered (BSE) and secondary electron (SE) modes, respectively. From these figures, it is possible to observe soft-edged particles, typically associated with bottom-up fabrication methods [111, 112].

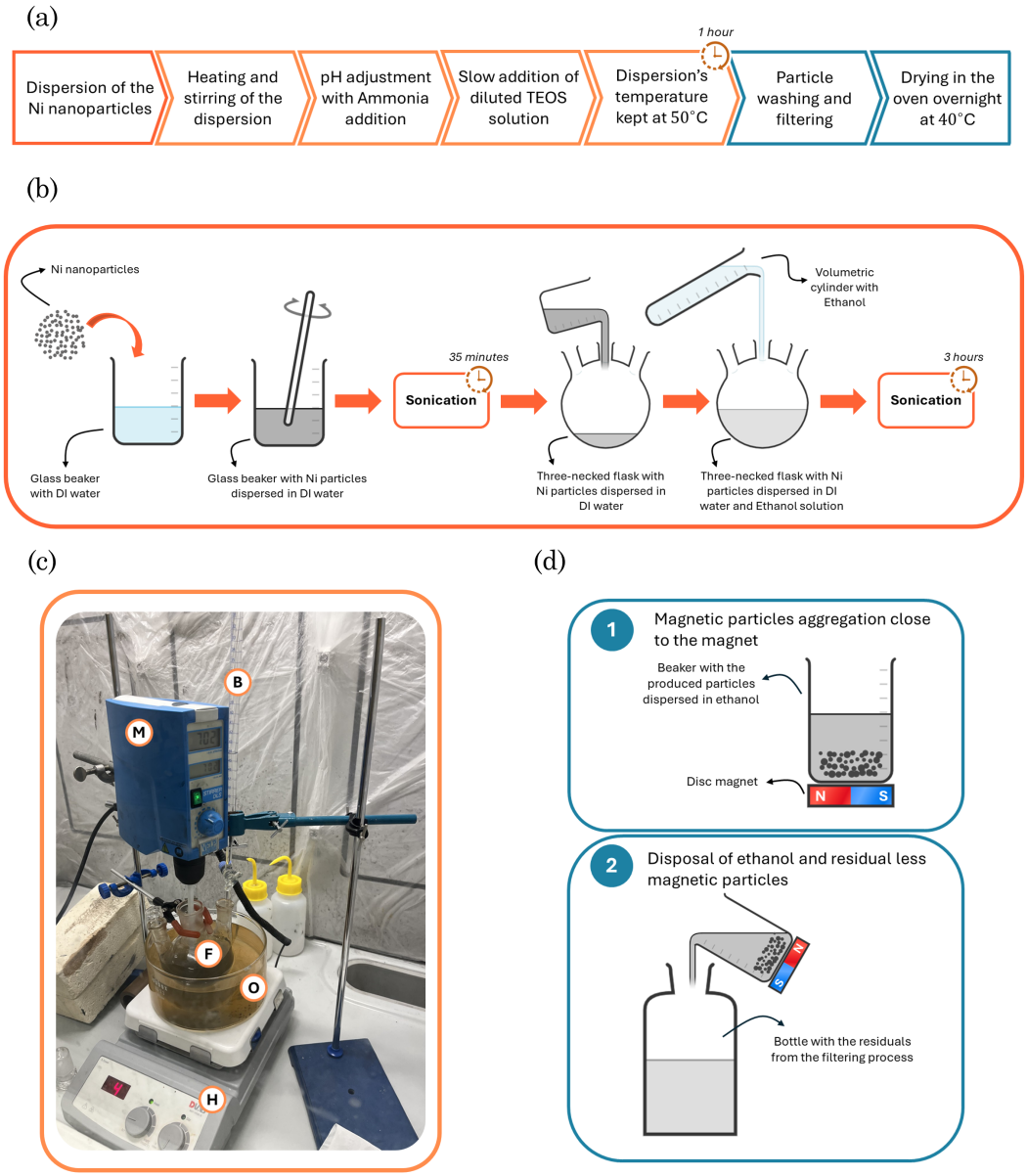

FIGURE 4.9: (a) Experimental procedure for preparing silica-coated Ni nanoparticles. (b) Illustration of the Ni nanoparticles' dispersion process in an Ethanol and deionized (DI) water solution. (c) Illustration of the setup used to deposit silica on the surface of the Ni nanoparticles, where: M, mechanical stirrer; B, burette with the diluted TEOS solution; F, round-bottom three-necked flask with the dispersion containing the Ni nanoparticles; O; oil bath; H, hot plate with digital thermometer. (d) Illustration of the particle washing and magnetic filtering procedure.

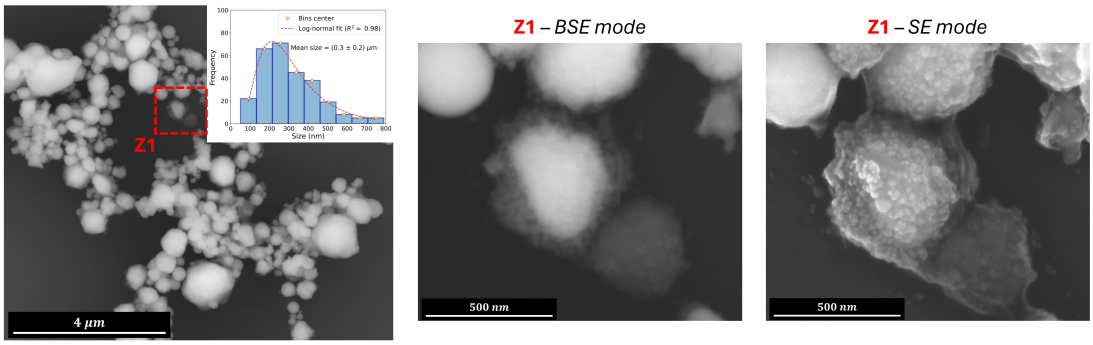

(a) (b) (c)

FIGURE 4.10: (a) SEM top-view image of the commercial Ni nanoparticles with $25000\times$ magnification and obtained in backscattered (BSE) mode, and histogram of the corresponding size distribution (inset). (b) and (c) SEM images of the zone Z1 (identified in subfigure (a)), obtained in BSE and secondary electron (SE) modes, respectively, and with $200000\times$ magnification.

Using the software ImageJ, the size of each particle in Figure 4.10 (a) (approximately 280 in total) was estimated from the measurement of their area, and the particle size histogram shown as inset was obtained. This histogram illustrates the profile of the fitted size distribution, which follows the commonly used log-normal function [106, 113]. From the fitted parameters, a mean particle size of $(0.3 \pm 0.2)\ \mu\mathrm{m}$ was estimated. This is significantly bigger than the average size documented by Sigma Aldrich (smaller than $100\,\mathrm{nm}$). Nevertheless, as can be realized from the histogram, these particles show a broad particle size distribution. In fact, from the zoom-in to zone Z1 shown in Figure 4.10 (c), it is possible to see that the bigger particles have smaller ones attached to their surface. The size of these smaller particles can be measured either using an higher magnified SEM image (as the case of Figures 4.10 (b) and (c)), or by considering TEM images (e.g. Figure A1 presented in the Appendix A1). However, this way, the analyzed sample would be restricted to the smaller sized particles. Therefore, the scale and size heterogeneity of the commercial Ni powder do not allow a representative measurement of their particle size distribution, neither using SEM, nor using TEM microscopy images. Alternatively, laser light diffraction techniques, such as dynamic light scattering (DLS) [114], could have been used.

The different color shading observable in Figure 4.10 (b), highlight the existence of another material covering the Ni particles. During its acquisition, the image's brightness was strongly dependent on the scanning rate. This behavior suggests the existence of an oxide layer (thicker than $10\,\mathrm{nm}$) covering the magnetic material.

The morphological properties of the silica-coated Ni particles were analyzed through inspection of the SEM images depicted in Figures 4.11 (a), (b) and (c). Figure 4.11 (b) corresponds to a zoom-in of zone Z2, identified in Figure 4.11 (a). From Figure 4.11 (b), it is possible to observe two distinctively-looked zones: zone Z3, with a more amorphous appearance, attributed to an increased amount of silica, the siliza zone; and zone Z4, more brightly colored, and similar to the Ni particles presented in Figure 4.10, the Ni particle zone. From these two figures it becomes clear that the material produced consists mostly of a silica matrix with embedded Ni nanoparticles. This is even more evident in Figure 4.11 (c), which illustrates a less magnified view of the silica-coated powder. In the latter, bearing in mind the appearances of zones Z3 and Z4, one can identify the existence of different silica clusters, with brighter particles (the Ni particles) crusted to their surface. In Figure 4.11 (c), some of these clusters are indeed identified with orange boxes.

Using the same methodology as before, the size distribution of the particles in Figure 4.11 (a) (approximately 250 particles in total) was fitted to a log-normal function [115], as illustrated in the histogram shown as inset. From the fitted parameters, a mean particle size of $(0.3 \pm 0.2)\ \mu\mathrm{m}$ was estimated. The similarity between the profile of the particle size distribution, and the obtained mean particle size, suggests that the silica deposition did not introduce many size modifications to the magnetic particles. This reinforces the hypothesis that the silica did not deposit directly on the surface of the particles, but rather was mixed and deposited within the particles dispersion during the fabrication process.

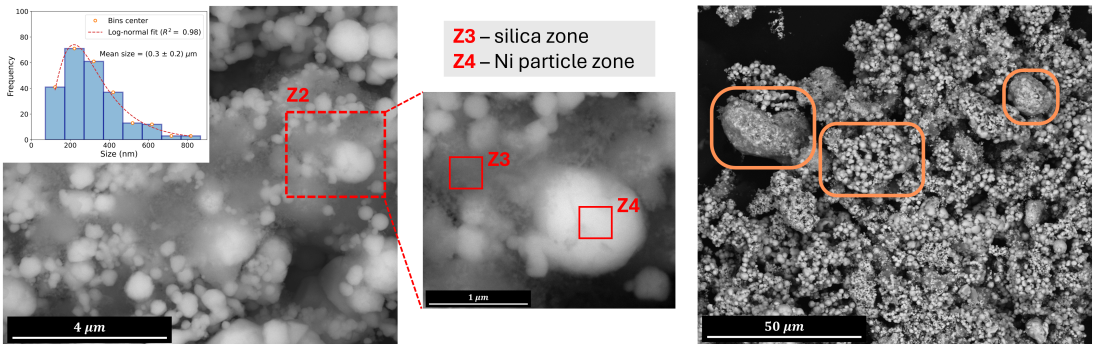

(a) (b) (c)

FIGURE 4.11: (a) SEM top-view image of the silica-coated Ni nanoparticles with $25000\times$ magnification and obtained in backscattered (BSE) mode, and histogram of the corresponding size distribution (inset). (b) SEM image of the zone Z2 (identified in subfigure (a)) with $100000\times$ magnification and obtained in BSE mode. (c) SEM top-view image of the same particles, with $2000\times$ magnification and obtained in BSE mode. The orange boxes identify some silica clusters with Ni particles crusted to their surface.

Structural characterization

In each sample, the Raman measurements were consistently performed in two different zones (identified as $Z1$ and $Z2$), each of them evaluated with two increasing laser powers (first with $5\,\%$ and then with $10\,\%$ power). After every measurement, the existence of any laser-induced oxidation was visually evaluated, using the instrument's integrated microscope. In Figures 4.12 (a) and (b) are depicted the Raman spectra obtained for the commercial and silica-coated Ni particles, respectively. A moving average filter was applied to the data, to smooth the signal acquired and facilitate the identification of the Raman peaks. Moreover, the spectra were trimmed as to show the range at which peaks can be identified $\left(100 - 2000\,\mathrm{cm}^{-1}\right)$. The abrupt drop observed in the Raman spectra close to $100\,\mathrm{cm}^{-1}$ results from a filter the instrument possesses, which limits the measured spectra to values above this threshold.

Regarding the commercial Ni nanoparticles results presented in Figure 4.12 (a), two different behaviors are shown in zones $Z1$ (top plot) and $Z2$ (bottom plot). After the measurements performed in zone Z1, no oxidation was observed. As a consequence, the peak identified at $1629\,\mathrm{cm}^{-1}$ for $10\,\%$ laser power (P_{laser}) must be intrinsic from the sample's properties. If the sample was purely made of metallic Ni, no vibrations should be detected through Raman measurements. It was previously reported by Mironova-Ulmane *et al.* [116] the existence of two-magnon (2M) scattering in NiO at a Raman shift around $1500\,\mathrm{cm}^{-1}$. Therefore, this peak suggests the existence of NiO in the commercial Ni powder. The slight deviation from the reported value can be justified by the dependence of the Raman peak position on the particle size [116]. On the other hand, zone $Z2$ was oxidized through laser heating. In this case, the peaks centered at $533\,\mathrm{cm}^{-1}$ and $1089\,\mathrm{cm}^{-1}$ correspond to one-phonon (1P) and two-phonon (2P) vibrational modes associated to NiO, as reported in [116].

As can be seen in Figure 4.12 (b), the deposition of silica introduced new and more pronounced vibration modes in the Raman spectra of the magnetic particles. In some zones, the vibration modes could be detected with both laser powers, as is the case of zone $Z1$ (top plot). While in others, e.g. in zone $Z2$ (bottom plot), one needed a stronger P_{laser} to detect the signal associated to those vibrations. For the latter, this can be related to a smaller amount of silica in the laser measuring spot.

The Raman peaks typically ascribed to the silica-coated Ni particles are identified in Figure 4.12 (b) with vertical dashed lines with the same color as that of the corresponding zone

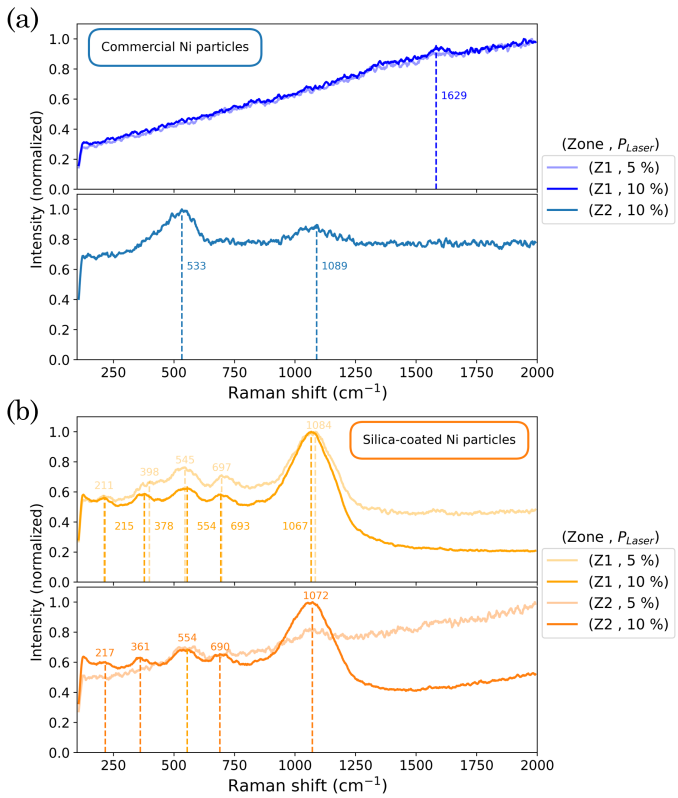

FIGURE 4.12: Normalized Raman spectra of the commercial (a) and silica-coated (b) Ni nanoparticles. In each subfigure, the Raman peaks are identified with vertical dashed lines with the same color as that of the corresponding experimental data, i.e. zone and laser power (P_{laser}).

and P_{laser} data. The smaller wavenumber modes, specifically, those located in the ranges $211 - 217\,\mathrm{cm}^{-1}$ and $361 - 398\,\mathrm{cm}^{-1}$, are originated from phononic vibrations between Ni and Si, as reported by Donthu *et al.* [117] for NiSi powders. The Raman peaks located around $550\,\mathrm{cm}^{-1}$ are related to 1P NiO vibrational modes, as observed in zone $Z2$ for the commercial Ni powder [116]. The $690 - 697\,\mathrm{cm}^{-1}$ band is associated with Si-O-Si linkages in SiO_3 groups [118]. Finally, the highest wavenumber mode, with peaks located at $1067 - 1084\,\mathrm{cm}^{-1}$ is a superposition of two vibrational modes. On the one hand, there is a contribution from the 2P mode from NiO [116]. On the other hand, asymmetric vibrations between Si and O neighboring atoms also contribute to this peak [118].

In Figures 4.13 (a) and (b) are presented the room-temperature X-ray diffractograms of the commercial and silica-coated Ni nanoparticles, respectively, with 2θ ranging from $30°$ to $110°$. The polycrystalline nature of both powders is evidenced by the Bragg peaks presented in those diffractograms. Moreover, in both cases, the position of these peaks is identical, denoting that the silica deposition did not modify the crystalline structure of the magnetic material.

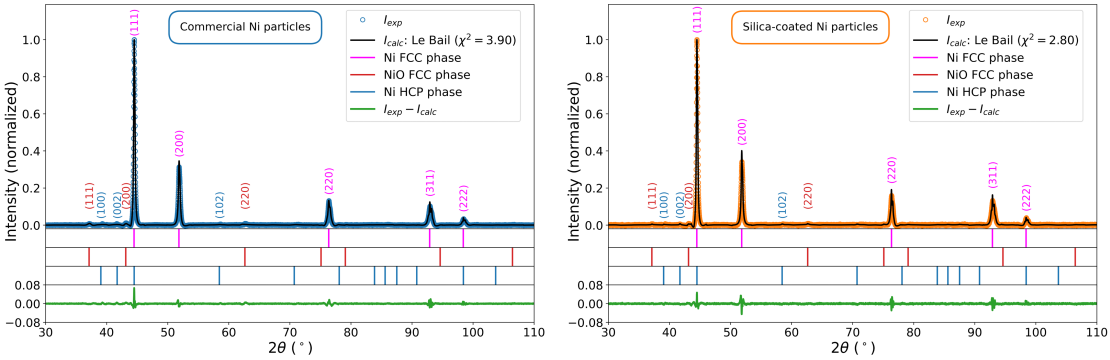

(a) (b)

FIGURE 4.13: Room-temperature X-ray diffractograms of the commercial (a) and silica-coated (b) Ni nanoparticles. Each diffractogram shows the experimental (I_{exp}: blue circles in (a) and orange circles in (b)) and the Le Bail refined (I_{calc}: black line) data, along with the expected Miller indexes for each reflection (colored as the attributed crystallographic phase). The Bragg peaks of each identified crystallographic phase are identified with vertical colored lines: the Ni face centered cubic (FCC) phase in pink, the NiO FCC phase in red and the Ni hexagonal close packed (HCP) phase in blue. The difference between the experimental and the refined data $\left(I_{exp} - I_{calc}\right)$ is also represented by the green line.

The Bragg peaks were attributed to the contribution from three different crystallographic phases. Firstly, a dominant Ni face centered cubic ($\mathrm{Fm\overline{3}m}$ space group) phase [108] was indexed to the peaks at $2\theta = 44.5°$ (111), $51.8°$ (200), $76.4°$ (220), $92.9°$ (311) and $98.4°$ (222). This phase is identical to the one previously attributed to the Ni microparticles. Secondly, a NiO face centered cubic (FCC) phase [112] was associated with the peaks at $2\theta = 37.1°$ (111), $43.1°$ (200) and $62.6°$ (220). Finally, the peaks at $2\theta = 39.0°$ (100), $41.7°$ (002) and $58.4°$ (102), were attributed to a Ni hexagonal close packed ($\mathrm{P6_3/mmc}$ space group) structure [119]. Using the FullProf software [107], structural Le Bail refinements were carried out. The refinements considered the three crystallographic phases already identified. In each phase, the refinements yielded the same lattice parameters for the commercial and silica-coated powders. Table 4.3 summarizes the lattice parameters obtained after the refinement. Additionally, from the fits it was possible to estimate the wt.% of each phase in the analyzed powders. For the commercial Ni powder, a 91.6% of Ni FCC phase, 6% of NiO FCC phase and 2.4% of Ni hexagonal close packed (HCP) phase was estimated. The considerable percentage of the NiO phase restates the existence of NiO on the commercial powder, corroborating with the conclusions from the Raman characterization. For the silica-coated Ni powder, the results were of approximately 89.7% for the Ni FCC phase, 0.4% for the NiO FCC phase, and 9.8% for the Ni HCP phase.

TABLE 4.3: Lattice parameters yielded from the Le Bail refinement of the commercial and silica-coated Ni nanoparticles. The refinement was comprised by a Ni FCC phase, a NiO FCC phase and a Ni HCP phase

Crystallographic phase	Lattice parameters					
	a (Å)	b (Å)	c (Å)	α (°)	β (°)	γ (°)
Ni FCC	3.52	3.52	3.52	90	90	90
NiO FCC	4.19	4.19	4.19	90	90	90
Ni HCP	2.66	2.66	4.33	90	90	120

Magnetic characterization

The magnetization hysteresis curves, at $10\,\mathrm{K}$, of the commercial (blue circles) and silica-coated Ni nanoparticles (orange circles) are represented in Figure 4.14. As can be seen from the inserted plot, in the low magnetic field regime, these particles manifest different magnetic behaviors. Still, for them both, there was no evidence of exchange bias. The commercial Ni particles have a coercivity of $3.3\,\mathrm{mT}$, while the silica-coated ones' coercivity value is of $19\,\mathrm{mT}$. This increase in the coercive field after the coating of Ni particles with silica has already been reported by Tago *et al.* [112]. With the silica deposition, the vibrations between the Ni, Si and O atoms (detected in the Raman measurements) enhance the stress applied in the particles. Consequently, their magneto-elastic anisotropy increases, and so does their coercivity [120]. This is further enhanced due to the smaller wt.% of NiO in the silica-coated nanoparticles in comparison to the commercial ones, as suggested by our Le Bail refinements. Specifically at low fields, this reduces the contribution from NiO to the coercivity *, thereby increasing the measured value.

At high fields, for both samples, the magnetization did not saturate asymptotically to a fixed value. This results from the antiferromagnetic contribution of the NiO present in both samples, as previously disclosed by the Raman and XRD measurements. Even though the NiO does magnetize in the field direction, it does not saturate in a $5\,\mathrm{T}$ field [121]. Thus, to remove this antiferromagnetic behavior, a linear fit to the high-field (above $2\,\mathrm{T}$) magnetization versus magnetic field was done, and the calculated slope (m_H) was subtracted to the magnetization. It is important to notice that the low-field magnetic response did not substantially change after this treatment.

From the treated experimental data it was possible to determine saturation magnetizations of $(47.4 \pm 0.2)\ \mathrm{Am^2kg^{-1}}$, and $(45.1 \pm 0.2)\ \mathrm{Am^2kg^{-1}}$ for the commercial, and silica-coated powders, respectively. The small decrease in the saturation value results from the

*NiO is expected to reduce the measured coercivity value (H_c) due to its anti-ferromagnetic behavior $(H_c = 0)$.

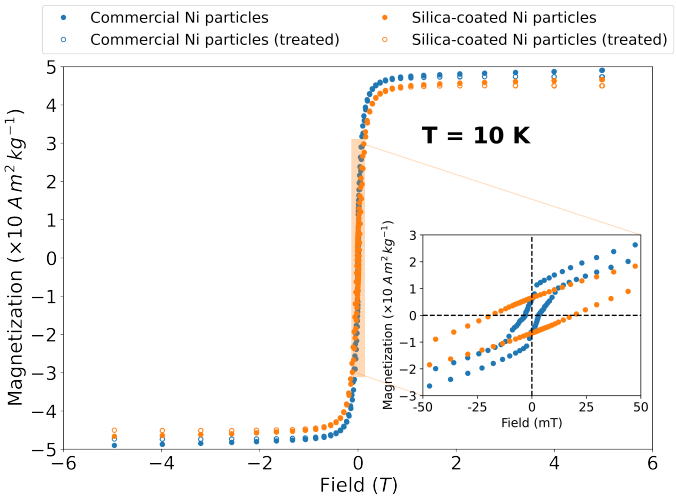

FIGURE 4.14: Magnetic response of the commercial (blue circles) and silica-coated (orange) Ni particles to varying magnetic fields within the range $[-5, 5]$ T, at $10\,\mathrm{K}$. The filled points correspond to the raw data, and the unfilled ones to the treated data, without the antiferromagnetic contribution from NiO. The inset corresponds to a zoom-in of the low-field range between $-50\,\mathrm{mT}$ and $50\,\mathrm{mT}$.

diamagnetic contribution from silica. From the ratio between the saturation magnetization values of the silica-coated sample $\left(M_{sat}^{\text{sample}}\right)$, and that of commercial Ni particles $\left(M_{sat}^{\text{Ni}}\right)$, it is possible to estimate the wt.% of silica in the fabricated sample. By considering the expression * presented in Equation 4.1, a 4.9 wt.% of silica was determined.

$$\text{wt.\%}\,(\text{SiO}_2) = \left(1 - \frac{M_{sat}^{\text{sample}}}{M_{sat}^{\text{Ni}}}\right) \times 100 \tag{4.1}$$

4.4. Magnetic liquid metals

The magnetic liquid metals produced in the scope of this thesis result from the combination of Galinstan and Ni particles. Depending on the average size of the embedded particles, two different fluids can be distinguished: the ferromagnetic microfluid, which considered Ni microparticles; and the ferromagnetic nanofluid, which incorporated silica-coated Ni nanoparticles into the liquid metal matrix. In this section, these fluids will be explored independently.

*This expression assumes that the magnetization of silica is negligible.

4.4.1. Ferromagnetic microfluid

4.4.1.1 Production method

The batches of the ferromagnetic microfluid were produced using the setup depicted in Figure 4.15 (a). The fabrication of each batch started by filling and weighing a $2\,\mathrm{mL}$ Eppendorf recipient with Galinstan. Then, the Ni micropowder was weighed to match the target magnetic material concentration - $4\,\mathrm{wt.\%}$ of Ni.

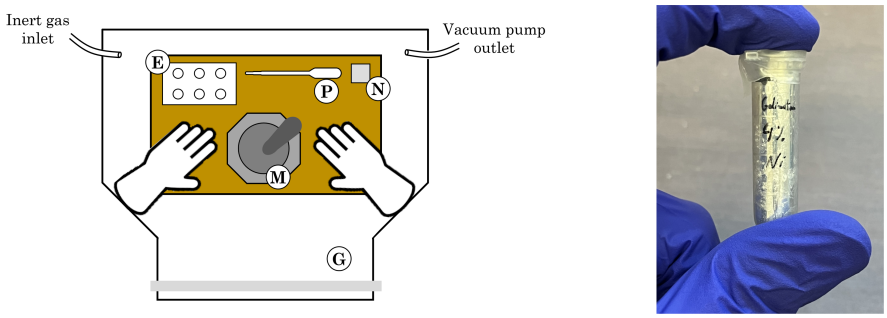

(a) (b)

FIGURE 4.15: (a) Illustration of the setup used to produce the ferromagnetic microfluid batches, where: G, Aldrich ® AtmosBag globe bag; M, mortar, and pestle; E, set of clean, filled with Galinstan and filled with Ni powder Eppendorf tubes; P, Pasteur pipettes; N, NdFeB magnets. (b) Exemplification of the storage of the ferromagnetic microfluid in a Parafilm-sealed Eppendorf recipient.

The mixture of Ni microparticles into the Galinstan matrix was made inside an Aldrich ® AtmosBag glove bag with a four-time purged * inert Argon atmosphere. The ferromagnetic material was mixed in the liquid metal using an agate mortar and pestle until the mixture became homogeneous [17, 73]. Using this method, the LM oxide layer is successively being broken and renewed. This promotes the LM adhesion to the magnetic particles, due to the oxide's great adhesive properties [75].

Finally, the magnetic susceptibility of the fluid was pre-evaluated by observing its response to the presence of permanent magnets. These tests are demonstrated in Videos V1 † and V2 ‡. The produced fluids were stored in Eppendorf recipients sealed with parafilm tape, as illustrated in Figure 4.15 (b).

*The purging protocol consisted of alternately establish a low pressure environment (down to below $10\,\mathrm{mbar}$ with a vacuum pump), and filling the glove bag with high purity Argon gas (99.9999% pure).

†Video V1 demonstrating the first pre-evaluation of the magnetic susceptibility of the ferromagnetic microfluid is available at: `https://drive.google.com/file/d/1SJudwg9nza8KsZcX9l4q47Wk_VmS3zgy/view?usp=sharing`

‡Video V2 demonstrating the second pre-evaluation of the magnetic susceptibility of the ferromagnetic microfluid is available at: `https://drive.google.com/file/d/1A5jgU8TDHer8yWxRsnH_MJkvcGjOjewO/view?usp=sharing`

4.4.1.2 Characterization

Morphological characterization

In Figure 4.16 is depicted the SEM image of the ferromagnetic microfluid. In this figure there are two distinguishable zones: zone $Z1$, corresponding to the Galinstan matrix; and zone $Z2$, showing a Ni piece incorporated in the liquid metal base. This illustrates the nature of the produced microfluid: during the fabrication process, instead of dissolving in Galinstan, the Ni microparticles were embedded into the liquid metal, forming nucleation sites with the liquid metal wrapping the magnetic particles.

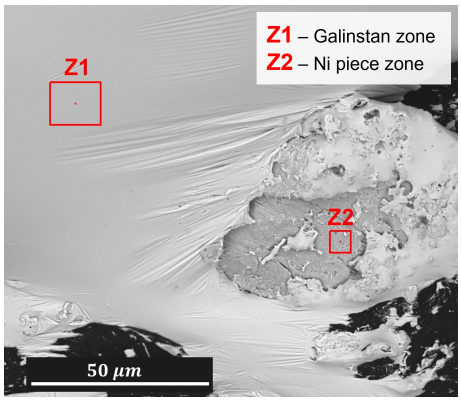

FIGURE 4.16: SEM top-view of the Galinstan and Ni microfluid with $2000\times$ magnification and obtained in backscattered mode.

Magnetic characterization

The magnetization of the ferromagnetic microfluid as a function of applied magnetic field curve results at $300\,\mathrm{K}$, two months after its production, are presented in Figure 4.17. At this temperature, the major contribution to the magnetization comes from Ni, as its magnetic susceptibility is orders of magnitude larger than that of the diamagnetic Galinstan matrix (as confirmed by the magnetization curve of Galinstan at $300\,\mathrm{K}$ depicted in Figure 4.4). Consequently, it is the incorporation of the Ni microparticles that provides the mixture with a ferromagnetic behaviour. The ratio between the saturation magnetization of the microfluid, and the saturation value of the Ni microparticles at $300\,\mathrm{K}$ should account for the wt.% of Ni in the mixture. Hence, from the experimental data, it was possible to calculate a Ni concentration of $2.6\,\mathrm{wt.\%}$. This value is smaller than the target Ni concentration of $4\,\mathrm{wt.\%}$. This is primarily originated by the adhesion of Ni particles to the Galinstan oxide layer that sticks to the agate mortar during the fabrication of the microfluid. As a result, these particles are not extracted by the Pasteur pipette, during the fluid's transference to the Eppendorf recipient.

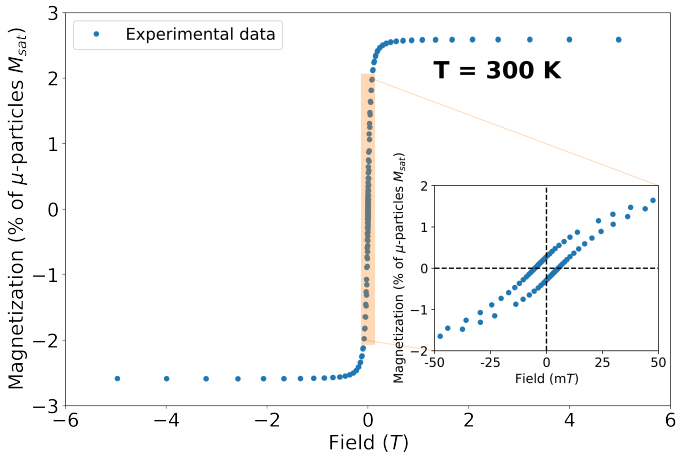

FIGURE 4.17: Magnetic response of the Galinstan and Ni (2.6) $\mathrm{wt.\%}$ fluid to varying magnetic fields within the range $[-5, 5]$ T, at $300\,\mathrm{K}$. The inset corresponds to a zoom-in of the low-field range between $-50\,\mathrm{mT}$ and $50\,\mathrm{mT}$.

As explained in Section 4.4.1.1, the adhesion of the Galinstan to the magnetic material is promoted through mechanically induced oxidation of the LM matrix. Moreover, Galinstan instantly oxidizes as it makes contact with air. It is therefore interesting to study the influence of particle oxidation on the durability of the magnetic properties of the microfluid. For such, the fluid Ni concentration was calculated from the magnetization curve results of different samples, in different time periods after its production. Table 4.4 summarizes the results from this study. It is important to clarify that, between its two measurements, the sample number 2 was not removed from the liquid sample holder. This assures that, in both measurements, the actual fluid Ni concentration is the same. Therefore, the decrease in the Ni $\mathrm{wt.\%}$ of sample number 2 shown in Table 4.4 suggests the presence of particle oxidation.

TABLE 4.4: Results of the ferromagnetic microfluid Ni $\mathrm{wt.\%}$ experimental determination for different samples, and different after-production time spans

Sample number	Sample mass (mg)	Time after production (months)	Experimental Ni wt.%
1	95.29	2	2.59
2	54.49	6	2.25
		7.5	2.09

Transport properties characterization

In Figures 4.18 (a) and (b) are presented the electric resistivity measurements performed for a ferromagnetic microfluid sample, in the stationary and sweep modes, respectively. In those figures, each (V, T, I) point corresponds to an averaged value over the respective electric current step. The errorbars correspond to the associated standard deviations.

Concerning the $V(I)$ measurements, a linear behavior was observed, as anticipated from Ohm's law (Equation 3.2). The slope obtained after fitting the data to a linear regression enabled the calculation of the electrical resistivity associated with each measurement mode. In the stationary mode, a value of $(3.429 \pm 0.007) \times 10^{-7}\,\Omega\mathrm{m}$ for ρ was obtained. In the sweep mode, ρ took a value of $(3.445 \pm 0.004) \times 10^{-7}\,\Omega\mathrm{m}$.

Regarding the $T(I)$ measurements, the sweep mode plot presented in Figure 4.18 (b), clearly demonstrates the heating of the sample in response to an increase in current. In both measurement modes, the mean temperature value $\left(\overline{T}\right)$ was calculated. The λ of the sample was determined by combining the obtained value for $\overline{T}$ with the Wiedemann-Franz law expression (Equation 3.3). In the stationary mode, a value of $(21.26 \pm 0.05)\ \mathrm{W\,m^{-1}\,K^{-1}}$ was calculated. In the sweep mode, an experimental value of $(21.17 \pm 0.03)\ \mathrm{W\,m^{-1}\,K^{-1}}$ for λ was obtained. These values are smaller than those obtained for the Galinstan sample, which can be attributed to the oxidation induced by the mixing of the Ni particles within the Galinstan matrix, during the fabrication process of the ferromagnetic fluid [75].

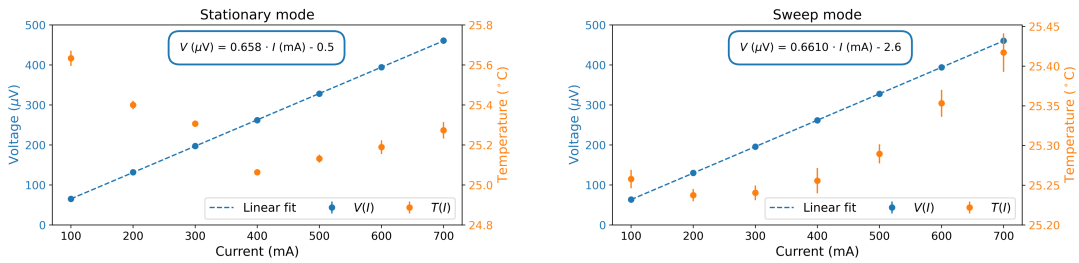

(a) (b)

FIGURE 4.18: Electric resistivity measurements obtained for a ferromagnetic microfluid sample in the stationary mode (a) and in the sweep mode (b).

4.4.2. Ferromagnetic nanofluid

4.4.2.1 Production method

The incorporation of the silica-coated Ni nanoparticles into the Galinstan matrix was successfully achieved considering the same production method as the one described for the ferromagnetic microfluid, in Section 4.4.1.1. However, in contrast to the microfluid, the nanofluid suffered a fast performance decrease with time, with a decrease of its magnetic response, and an increase of its viscosity. In Video V3 * are compared two tests to the nanofluid's magnetic susceptibility, right after and one week after its production. From

*Video V3 illustrating the ferromagnetic nanofluid's magnetic susceptibility tests over time is available at: `https://drive.google.com/file/d/1vSSesiv3ylCinXREZkcL3S47GN1Lqw91/view?usp=sharing`

there, it is possible to see that in the second test, even with a greater amount of permanent magnets (nine magnets instead of six), they needed to be much closer to see the eppendorf tube move. Moreover, the magnetic force could not overcome the gravitational force to pick up the sample using only magnetic attraction. This clearly evidences a lost on the magnetic properties of the fluid. Therefore, alternative production methods were attempted.

Since fluid oxidation might be the main source of magnetic weakening, oxide removal was attempted. To do so, a nanofluid droplet was submerged in an acidic solution of $1\,\mathrm{mol\,L^{-1}}$ of HCl. As described in Section 2.2, this strategy is commonly employed [46]. In Video V4 * is illustrated the fluid behavior after being 5 minutes, and 1 hour submerged in the HCl solution. In both cases it is possible to see a stream of bubbles being released from the droplet. Comparing these videos, the stream's flow decreased, and the droplet shape became more round with time. This denotes the incremental removal of the oxide layer wrapping the droplet.

To successfully embed the silica-coated nanoparticles within the Galinstan matrix, while producing a long-lasting nanofluid, the forementioned methods were adapted to develop an hybrid solution. The mixture of the particles into the LM was made in a controlled atmosphere (six-time purged with Argon), using an agate mortar and pestle. However, in this case, the addition, and mixture of the magnetic nanopowder was performed stepwise. Firstly, half of the target powder mass was added and mixed during one hour, until the mixture became homogeneous. Afterwards, the rest of the powder was poured into the mortar, and mixed for another hour. In the end, the produced fluid was transferred into a glass flask with a $0.01\,\mathrm{mol\,L^{-1}}$ HCl solution, and its response to the presence of permanent magnets was evaluated. This test is demonstrated in Video V5 †. Comparing to the previously described methods, the latter seemed to produce a more magnetic responsive fluid.

*Video V4 illustrating the time evolution of the ferromagnetic nanofluid oxide removal is available at: `https://drive.google.com/file/d/1BlVu3TJrBhuxd6eSEtez1CxkVPZuJ3Lm/view?usp=sharing`

†Video V5 illustrating the ferromagnetic nanofluid magnetic susceptibility test for the hybrid production method is available at: `https://drive.google.com/file/d/11HvfTSFGmM0uF2e2UrR0d_zHybYTfq8x/view?usp=sharing`

4.4.2.2 Characterization

Magnetic characterization

The magnetic characterization results presented in this section are relative to a ferromagnetic nanofluid, produced using the same method as that of the ferromagnetic microfluid. During the time period (one month) between the three measurements to be discussed, the sample was kept stored inside the Quantum Design liquid sample holder, wrapped with teflon tape. The target magnetic material concentration of this sample was of $3\,\mathrm{wt.\%}$ of silica-coated Ni nanoparticles, which belonged to the fifth batch produced. As depicted in Table B3, presented in Appendix B, for these particles it was determined an experimental $8.9\,\mathrm{wt.\%}$ of silica.

In Figure 4.19, are presented the magnetization of the ferromagnetic nanofluid as a function of applied magnetic field curve results, at $300\,\mathrm{K}$, one day, one week and one month after production. Similarly to the microfluid, due to the negligible magnetic susceptibility of the Galinstan matrix, here it was the incorporation of the silica-coated particles that provided the mixture with a ferromagnetic behavior. Nevertheless, the successive decrease in the saturation magnetization with time confirms the magnetic strength loss, as previously predicted from the susceptibility tests presented in Video V3. From the ratio between the saturation magnetization of the nanofluid, and the saturation value of the nanoparticles at $300\,\mathrm{K}$ $\left(45.3 \pm 0.2\,\mathrm{Am^2kg^{-1}}\right)$, it is possible to estimate the $\mathrm{wt.\%}$ of silica-coated particles in the mixture. The calculated fluid nanoparticles concentration results are summarized in Table 4.5.

TABLE 4.5: Results of the ferromagnetic nanofluid nanoparticles $\mathrm{wt.\%}$ experimental determination for three after-production time spans: one day, one week, and one month

Sample mass (mg)	Time after production	Experimental nanoparticles wt.%
164.79	one day	0.53
	one week	0.42
	one month	0.26

During a time span of one month, the estimated fluid concentration decreased $51\,\%$, from a $0.53\,\mathrm{wt.\%}$ to a $0.26\,\mathrm{wt.\%}$ of silica-coated particles. This constitutes a direct measurement of the nanofluid's magnetic loss. Comparing with the microfluid results, presented in Table 4.4, here the downwards trend is more intensified. Taking into account the sample's storage conditions, this suggests an intrinsic fluid oxidation. The oxygen present in the silica composition can be reacting with the Galinstan matrix, therefore speeding up

the fluid oxidation process. As a consequence, the fluid's magnetic susceptibility diminishes much faster, as evidenced. Moreover, the experimental fluid concentration values are much smaller than the target one. This is primarily due to the magnetic material and Galinstan slurry that adheres to the agate mortar during the production of the nanofluid, and that could not be extracted.

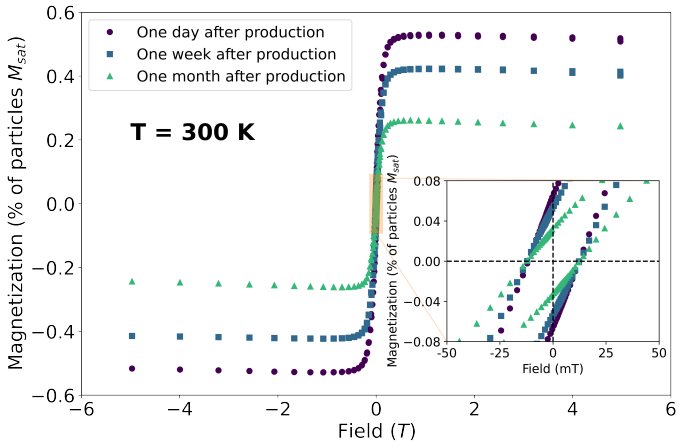

FIGURE 4.19: Magnetic response of the Galinstan and silica-coated Ni nanoparticles fluid to varying magnetic fields within the range $[-5, 5]$ T, at $300\,\mathrm{K}$, for different time spans (one day, one week and one month) after its production. The inset corresponds to a zoom-in of the low-field range between $-50\,\mathrm{mT}$ and $50\,\mathrm{mT}$.

Even though Galinstan's contribution to the magnetization of the ferromagnetic nanofluid can be neglected in the analysis of the hysteresis curves, the same does not apply for their isofield magnetization as a function of temperature $(M(T))$ curves. The $M(T)$ curves, during cooling and heating, of the nanofluid sample are depicted in Figure 4.20, for the three after-production time spans in discussion. In that figure, for each time span, an orange dashed box identifies the temperature range between $240\,\mathrm{K}$ and $300\,\mathrm{K}$, where two abrupt variations of the magnetization value are observable. The zoom-ins of these regions are illustrated in the $M(T)$ plots on the right side of Figure 4.20. These magnetization variations have already been reported in other Galinstan-based magnetic fluids [73, 99, 122]. In specific, Keerthivasan Rajamani [122] attributed these sharp variations to the fluid's solid state phase transitions. Through inspection of the local maxima of the module of the magnetization derivative relative to the temperature $(|\partial_T M|)$, it was possible to determine the temperature value associated with these transitions. During cooling, temperatures in the range $T_S = [252, 254]$ K were determined, corresponding to the solidification of the fluid. During heating, the melting temperature (T_M) was found to have values ranging between $294\,\mathrm{K}$ and $295\,\mathrm{K}$. However, these values do not coincide with the solidification and melting points determined for Galinstan through DSC analysis (see

Figure 4.2 in Section 4.1.2). There are two main reasons for such phenomenology. On the one hand, the silica-coated Ni nanoparticles, which are embedded in the liquid metal, create additional nucleation sites, that accelerate the heterogeneous solidification process, therefore culminating in a higher solidification temperature. On the other hand, the temperature measured in the magnetometer corresponds to the chamber's temperature, and not specifically to the sample's temperature, as is the case of the DSC calorimeter. As a consequence, the real sample temperature lags behind the measured temperature, resulting in a higher measured melting temperature on heating.

As illustrated in Figure 4.20, the $M(T)$ cooling curves exhibit a peak in the value of magnetization at lower temperatures, which are indicated by dashed blue boxes. The aforementioned peaks reach their maximum value at a temperature of approximately $6\,\mathrm{K}$. These peaks can be attributed to the superconductive behavior of Galinstan for temperatures bellow $6.6\,\mathrm{K}$ as previously reported by Ren *et al.* [123].

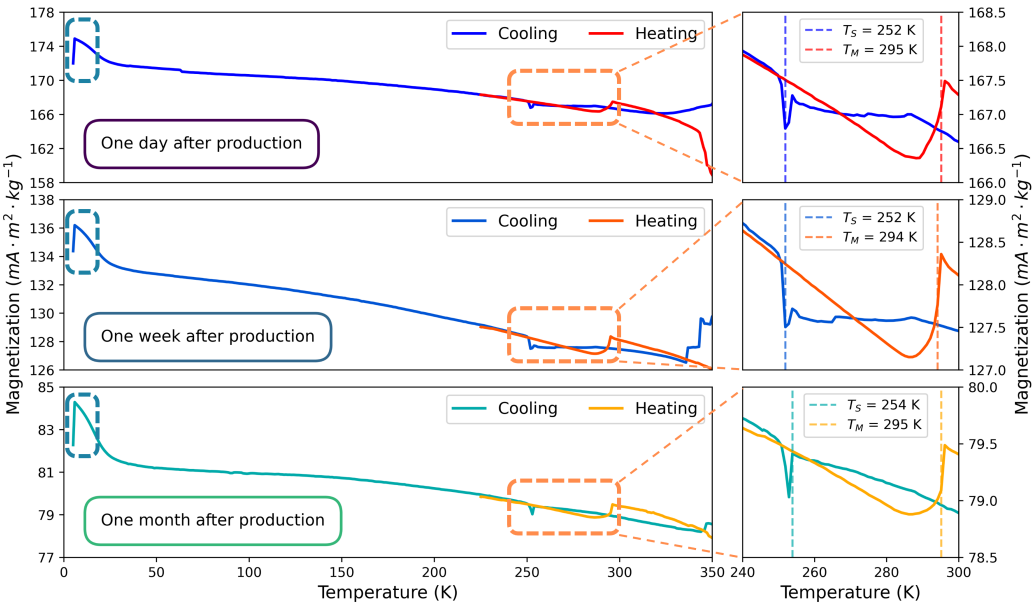

FIGURE 4.20: Isofield magnetization versus temperature curves obtained for the Galinstan and silica-coated Ni nanoparticles fluid, during cooling and heating, for different after-production time spans - one day, one week, and one month. The blue dashed boxes identify the peaks associated to the superconductive transition of the Galinstan. The plots on the right side correspond to a zoom-in of the zones identified with orange dashed boxes $(T \in [240, 300]\ \mathrm{K})$ on the plots on the left side. The nanofluid solidification (T_S) and melting (T_M) temperatures, determined in each measurement, are identified with vertical dashed lines on the right-side plots.

5. 1D cooling performance *

The ferromagnetic microfluid, resulting from the combination of Galinstan and Ni microparticles at a $2.6\,\mathrm{wt.\%}$ concentration, was synthesized for incorporation in a centimeter-thick MAFTS device. There the fluid is intended to move axially, in the direction of the gravitational force, to promote a 1D cooling operation.

In this chapter, the experimental setup used to evaluate the 1D MAFTS cooling performance will be presented. In addition, the results from its performance evaluation will be discussed. In particular, the influence of the loading filling ratio (FR) and the device operating frequency will be assessed.

5.1. Experimental setup

The performance of the ferromagnetic microfluid was evaluated in a home-made MAFTS device, as reported in [25, 124], and illustrated in Figures 5.1 (a) and (b). As depicted in Figure 5.1 (b), the ferromagnetic microfluid is stored inside a cylindrical container made of PMMA, with $1 \times 1\,\mathrm{cm}$ height and diameter. On its top and bottom surfaces, two copper plates - thermally conductive windows for the heat source (bottom) and sink (top) - are physically attached to the cage with non-magnetic screws.

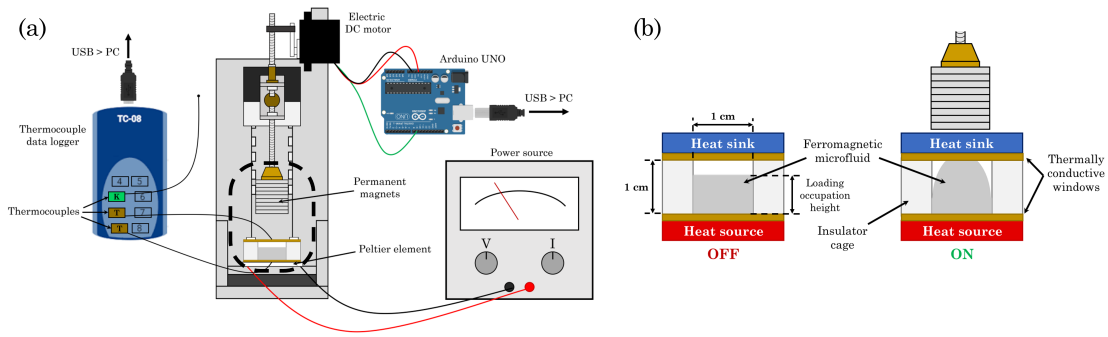

FIGURE 5.1: (a) Illustration of the setup used in the experiments conducted with the developed ferromagnetic microfluid incorporated into the 1D MAFTS, with the device outlined by the dashed box. (b) Schematic of the device used and its operating states (ON and OFF). [25]

As can be seen from the setup of Figure 5.1 (a), the fluid is controlled by applying a varying external magnetic field. The field variation is promoted by the vertical movement of a

*Adapted from **J. P. Maganinho**, R. M. C. Pinto, V. Andrade, B. G. F. Eggert, C. Frommen, J. P. Araújo, J. O. Ventura, J. Oliveira, A. L. Pires and J. H. Belo - "Engineering a Galinstan-based Ferromagnetic Fluid for Heat Management", *Energy Conversion and Management*, vol. 322, 2024.

set of nine $20 \times 20 \times 3\,\mathrm{mm}$ NdFeB block magnets purchased from Supermagnete. This movement is driven by an electric DC motor digitally controlled by an Arduino program. As measured using a Lakeshore 455 DSP gaussmeter placed at the top surface of the container, the field intensity varies periodically between 12 and $438\,\mathrm{mT}$ (magnets at the top and bottom position, respectively, of their range of motion).

The device operates between two states, as illustrated in Figure 5.1 (b). In the OFF state, the magnetic field strength is insufficient to overcome the gravitational force and the fluid remains only in contact with the heat source - a Peltier element (TEC1-12706, 12 V). In the ON state, as the strength of the applied magnetic field increases, the fluid is attracted to the magnets, creating a thermal bridge with the heat sink - a copper plate in contact with the ambient. Videos V6 * and V7 † demonstrate the MAFTS operation for low and high magnet movement frequencies, respectively. These videos illustrate the cyclical formation and breaking of the thermal bridge, as the MAFTS transitions between its ON and OFF states. The temperature of the heat source and heat sink is monitored using two TCs, which are attached to the conductive windows, using thermal paste and copper tape. The ambient temperature is measured with another thermocouple. These TCs are connected to a TC-08 thermocouple data logger (Pico Technology), and the data acquisition is controlled by a homemade software.

The device starts operating when the heat source reaches a constant temperature value $\left(T_{\text{source}}^{\text{start}}\right)$ during the heating process. This triggers the motor, starting the magnets vertical movement at a predefined frequency, during a certain time span. Following this time, the device is cooled, using an electrical fan. All these processes are fully automated with custom-developed software programs.

5.2. Performance evaluation

The 1D MAFTS prototype presented in the previous section was used to demonstrate the feasibility of the produced ferromagnetic microfluid in thermal management applications. The influence of the FR, i.e. the volume percentage occupied by the ferromagnetic fluid inside the cylindrical container, and the frequency of the magnets' vertical motion (operating frequency) on the performance of the device were studied. With that purpose, for

*Video V6 demonstrating the 1D MAFTS operation for a lower magnet movement frequency is available at: `https://drive.google.com/file/d/1Dycx48W5kkwS14x-SY0tOeFDxZOCAGRO/view?usp=sharing`

†Video V7 demonstrating the 1D MAFTS operation for a higher magnet movement frequency is available at: `https://drive.google.com/file/d/1FCcZCzjvfNKUyLFXYzRaSuywjNE37QDQ/view?usp=sharing`

each FR ($65\,\%$ and $85\,\%$), several operating frequencies (0.014 Hz, 0.05 Hz, 0.1 Hz and 0.5 Hz) were studied.

5.2.1. Performance evaluation trials

In Figure 5.2 (a), for a FR of $65\,\%$, the temperature variation of the heat source and sink during a complete trial is illustrated. Each trial comprises three steps: heating up until the heat source reaches a constant temperature value $\left(T_{\text{source}}^{\text{start}}\right)$, device operating (at a specific operating frequency, 0.05 Hz in this case) and cooling.

In Figure 5.2 (b), it is emphasized the effect of the MAFTS operation on the temperature difference between the heat source and sink $\left(\Delta T^{so-si} = T_{\text{source}} - T_{\text{sink}}\right)$. As can be seen from the inserted plot representing the first $100\,\text{s}$ of operation, in the ON state (high-field state) there is a decrease in ΔT^{so-si}. This indicates that the heat produced by the source is exchanged through the fluid and absorbed by the sink, as illustrated in Figure 5.2 (c). In the OFF state (low-field state), the previously absorbed heat is released by the sink, thus decreasing its temperature (T_{sink}) and, consequently, increasing ΔT^{so-si}. Nevertheless, the cycle overall variation in ΔT^{so-si} is negative, because the ΔT^{so-si} decrease in the ON state over-matches its increase in the OFF state. As a result, the sequential occurrence of these cycles ends up resulting in a decrease of the average temperature difference with time. This behavior was manifested in every trial, which highlights the proof of principle of the ferromagnetic microfluid-based MAFTS device.

5.2.2. Influence of the FR and operating frequency on the performance

To evaluate the influence of the experimental parameters on the performance of the 1D MAFTS device, a set of figures of merit is considered. Firstly, it is considered the evolution of the temperature span (ΔT_S) with operating time (t), given by:

$$\Delta T_S\,(t) = \left(1 - \frac{\Delta T\,(t)}{\Delta T^{so-si}\,(0)}\right) \times 100 \tag{5.1}$$

where $\Delta T^{so-si}\,(0)$ corresponds to the starting value of ΔT^{so-si}, and $\Delta T\,(t)$ is the value of ΔT^{so-si} averaged over a cycle centered at time t. The higher the value of this figure of merit, the larger is the decrease of the temperature gradient between the heat source and heat sink, in comparison to its initial value. In addition, it is also considered the minimum ΔT^{so-si} rate achieved in each trial. This value corresponds to the minimum of

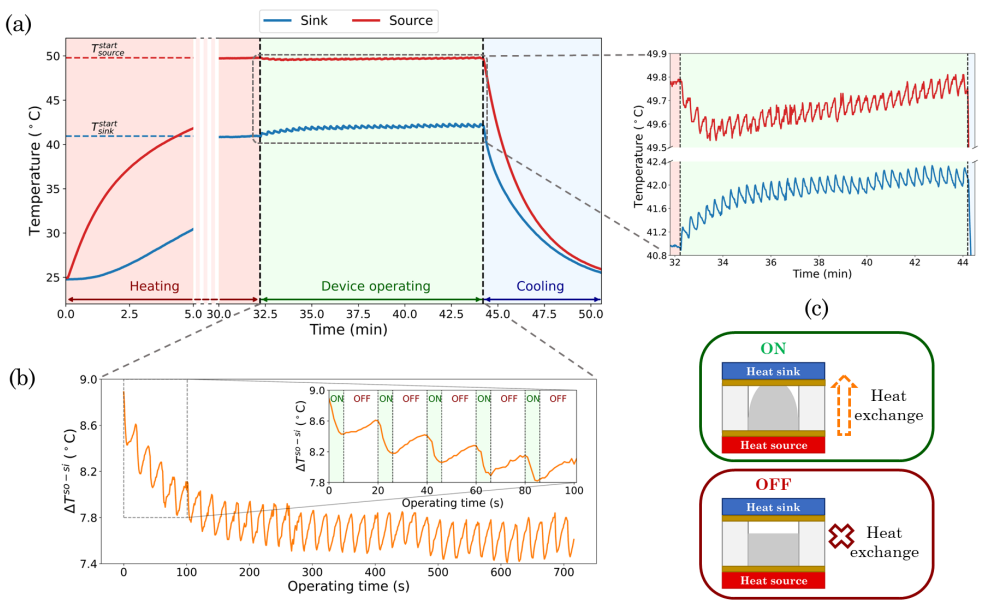

FIGURE 5.2: (a) Illustration of the temperature variation of the heat source (solid red line) and heat sink (solid blue line) throughout a complete trial, for a filling ratio of $65\,\%$, and a magnet movement frequency of $0.05\,\mathrm{Hz}$. The red and blue dashed horizontal lines identify the temperature values of the heat source $\left(T_{\text{source}}^{\text{start}}\right)$ and heat sink $\left(T_{\text{sink}}^{\text{start}}\right)$ at the start of the device operation, respectively. The subplot on the right corresponds to a zoom-in of the device operation period of time. (b) Temperature difference between source and sink $\left(\Delta T^{so-si}\right)$ time dependence during the device operation, in the same trial. The subplot identifies the different operating states of the device. (c) Diagrams illustrating the fluid shape in each operating state and its relation to the high and low heat exchange between both terminals.

the derivative of ΔT^{so-si} with respect to the operating time. The more negative the value of ΔT^{so-si} rate is, the more efficient is the sink's heat absorption. Furthermore, the SR, as defined by Equation 5.2, is taken into consideration. This parameter quantifies the enhancement in the device's effective thermal conductivity during its operation $\left(k_{eff}^{ON}\right)$, in comparison to its value when deactivated $\left(k_{eff}^{OFF}\right)$. To calculate k_{eff}^{ON} and k_{eff}^{OFF}, the system was modeled as a stationary one-dimensional thermal circuit. The details of this model are presented and explained in greater depth in the Appendix C. Finally, to quantify the heat flux dissipation through the sink (ϕ_{sink}), the same model was considered. The value of ϕ_{sink} obtained in each trial was calculated using Equation 5.3, where ΔT_f^{so-si} is the value of ΔT^{so-si} at the end of the MAFTS operation, and L is the thickness of the 1D MAFTS device $(L = 1\,\mathrm{cm})$.

$$\mathrm{SR} = \frac{k_{eff}^{ON}}{k_{eff}^{OFF}} \qquad (5.2)$$

$$\phi_{sink} = \frac{k_{eff}^{ON}}{L} \cdot \Delta T_f^{so-si} \qquad (5.3)$$

Concerning the influence of the FR on the MAFTS performance, from the plots in Figure 5.3 (a), it is clear that, despite the similar ΔT_S time dependence for both FRs, at each

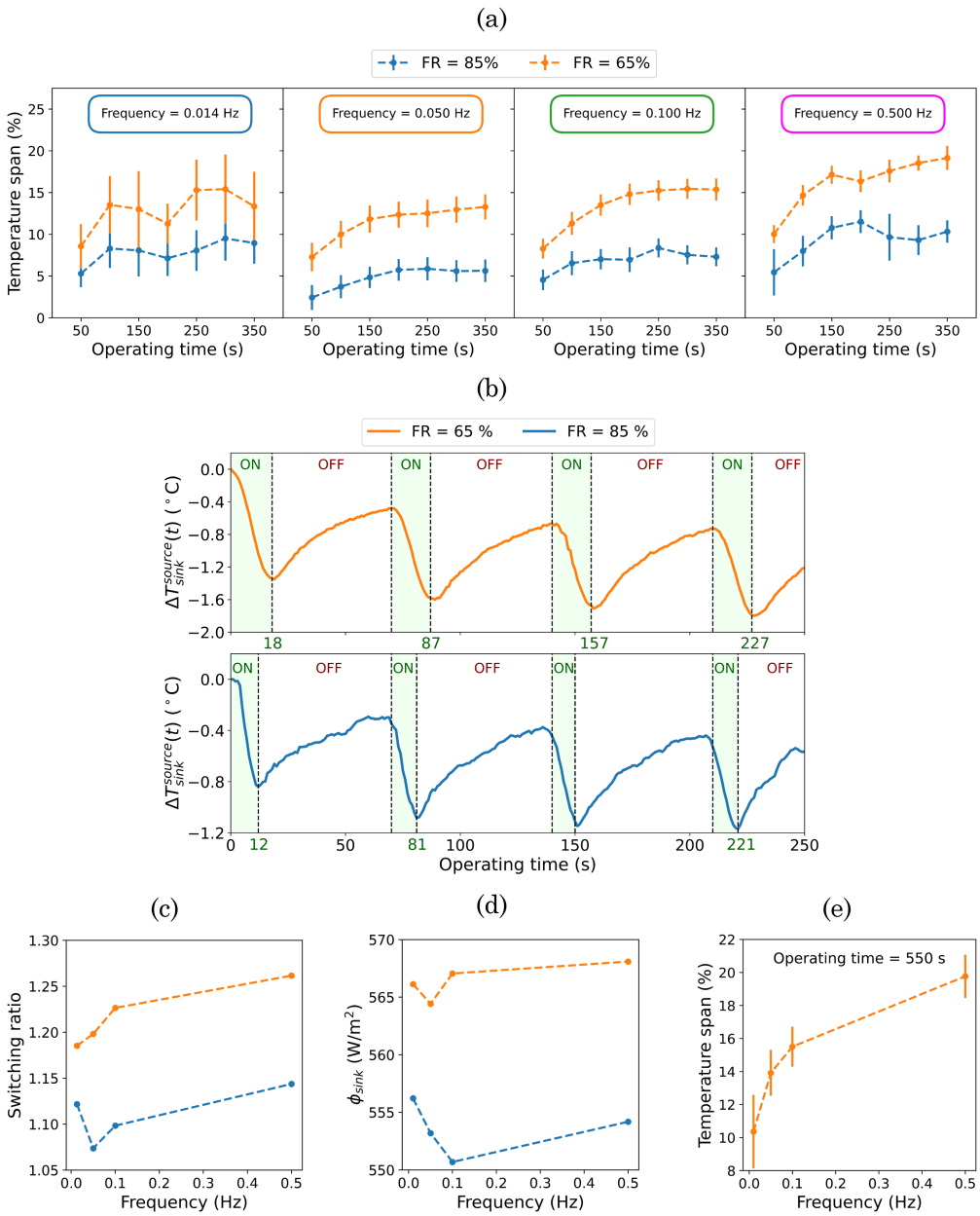

FIGURE 5.3: (a) Temperature span (ΔT_S, as defined in Equation 5.1) time evolution for the FRs and operating frequencies tested on the 1D MAFTS. (b) Illustration of the variation in the temperature difference between the heat source and heat sink $\left(\Delta T_{\text{sink}}^{\text{source}}\right)$ during the first $250\,\text{s}$ of the MAFTS operation for both FRs and a magnet movement of $0.014\,\text{Hz}$ frequency. The different operating states of the device (ON and OFF) are identified, as well as the ON to OFF transition times (green numbers). (c) and (d) Switching ratio (SR) and heat flux dissipation through the sink (ϕ_{sink}) obtained for each FR and operating frequency tested, respectively. (e) Temperature span obtained after $550\,\text{s}$ of MAFTS operation, at a FR of $65\,\%$, for every operating frequencies tested.

operating frequency, higher ΔT_S values were achieved for a FR of $65\,\%$. This effect is primarily related to the longer ON state time spans experienced for this FR. The MAFTS is in the ON state during the time period in which a thermal bridge is established between the heat source and heat sink terminals by the ferromagnetic fluid. At a specific operating frequency, the time dependence of the magnetic field is identical for both FRs, as the movement of the magnets is identical. However, the magnetic field strength required to attract the ferromagnetic microfluid and establish the thermal bridge is higher for the $85\,\%$ FR, due to the larger volume of fluid that must be attracted. Consequently, the time period in which the magnetic field satisfies this condition will be reduced. To illustrate, when an operating frequency of $0.014\,\mathrm{Hz}$ is considered, for a FR of $85\,\%$, the transfer of heat between the heat source and sink, and through the microfluid, on average, during $13\,\mathrm{s}$ in each cycle. In contrast, for a FR of $65\,\%$, this thermal connection lasts, on average, $17\,\mathrm{s}$ per cycle. These ON state time span differences are illustrated in Figure 5.3 (b). This phenomenon culminates in a greater heat dissipation from the source, precisely, for the $65\,\%$ FR. This conclusion is corroborated by the higher values of SR and ϕ_{sink} yielded for the $65\,\%$ FR across all tested frequencies, as depicted in the plots in Figures 5.3 (c) and (d), respectively.

Regarding the plots depicted in Figure 5.3 (a), it is also important to clarify the considerable uncertainty associated with the ΔT_S values at $0.014\,\mathrm{Hz}$ frequency. At this frequency, the duration of the heat rejection (OFF state) and heat adsorption (ON state) periods is longer. Consequently, the temperature fluctuations within each cycle are more pronounced, resulting in a higher standard deviation for each ΔT_S.

To evaluate the effect of the operating frequency, in Figure 5.3 (e) is depicted the temperature span obtained after $550\,\mathrm{s}$ of device operation, for every frequency tested, when considering a FR of $65\,\%$. From there, it becomes clear that, for longer operating times, there is a tendency for ΔT_S to increase with frequency. This is mostly due to the enhancement of the number of heat exchange cycles between the two terminals. Nevertheless, this increase in the temperature span with the operating frequency is expected to be verified only until a certain frequency threshold (f_{TH}), as previously observed by Puga *et al.* [25]. Above this threshold, due to its viscosity, the fluid does not have time to make a thermal bridge between the heat source and heat sink terminals. Consequently, the obtained temperature spans will be smaller than or equal to the ones achieved for frequencies bellow f_{TH}.

In light of the aforementioned phenomena, it is possible to conclude that the tested ferromagnetic microfluid-based MAFTS device exhibited optimal performance for a FR of $65\,\%$ and an operating frequency of $0.5\,\mathrm{Hz}$. Under these working conditions, the MAFTS achieved a maximum ΔT_S value of $19.8\,\%$, a minimum ΔT^{so-si} rate of $-0.27\,^{\circ}\mathrm{C/s}$, and a SR of 1.26. This resulted in a ϕ_{sink} of $568\,\mathrm{W\,m^{-2}}$, corresponding to a heat dissipation efficiency of $62.4\,\%$. As stated by Klinar *et al.* [4], the most appropriate metric for performance comparison in thermal switches is the SR. Therefore, under these optimal working conditions, the 1D MAFTS device demonstrated superior performance compared to the results reported by Shi *et al.* [14] and by Sütterlin *et al.* [32], where $\mathrm{Fe_3O_4}$-based ferrofluids were employed as working fluid, with maximum values for SR of 1.12 and 1.04, respectively. In contrast, the $\mathrm{MnFe_2O_4}$-based MAFTS developed by Andrade *et al.* [11] attained a maximum SR of 7.33 for a fully filled $3\,\mathrm{cm}$-thick device and an operating frequency of $0.3\,\mathrm{Hz}$. The latter yielded a notable improvement in performance in comparison to our work, primarily due to the significant enhancement in k_{eff}^{ON}, resulting from the magnetically-induced anisotropy, which aligned the magnetic particles along the field direction to thermally connect the heat source and heat sink. Nevertheless, the lower boiling point of the $\mathrm{MnFe_2O_4}$-based working fluid, in comparison to Galinstan ($> 1300\,^{\circ}\mathrm{C}$ [17, 19–21, 38, 48]), suggests that the 1D MAFTS device may operate for a longer period of time at the same performance level.

In conclusion, the outcomes of the 1D MAFTS experiments suggest the possibility of employing this device not only for the cooling of electronic components, but also as a critical component in thermal circuits. The operation of the device resulted in an increase in its effective thermal conductivity. This demonstrates the device ability to facilitate the dissipation of the heat produced by the heat source, thereby reducing the latter's temperature. Conversely, the decrease in ΔT^{so-si} in the ON state and its subsequent increase in the OFF state clearly illustrate the ability of the device to regulate the heat exchange between its terminals, dependent upon the strength of the applied magnetic field. This substantiates the potential for the incorporation of such a device in thermal circuits.

6. 2D cooling performance

The ferromagnetic nanofluid, consisting of silica-coated Ni nanoparticles embedded in a Galinstan matrix, was fabricated to be incorporated into a millimeter-thick 2D MAFTS device. The dimensions of the device were primarily designed to target chip cooling applications. The objective is to achieve a planar actuation, which will facilitate a 2D cooling operation. This chapter will detail the design of the 2D MAFTS device, which was created from the ground up. Consequently, the methodology employed for the design development, fabrication and experimental evaluation of the cooling performance of the device will be explored. Subsequently, the findings of the performance evaluation will be presented and discussed.

6.1. Development of the 2D MAFTS device

6.1.1. Device design

The compatibility issues of Galinstan with metals commonly used in cooling devices, namely its corrosive effect on Cu and Al [43, 52, 61], raised several questions about the choice of materials for the 2D MAFTS device. However, in fluid transport applications, the use of non-metals facilitates channel development. In particular, PDMS has been widely used in such applications, where Ga-based LMs are considered as the working fluid [63–68]. Moreover, the use of PDMS enables easy replication of the developed structures, always considering the same mold [64].

The configuration of the 2D MAFTS device is depicted in Figure 6.1 (a). The device is constructed from PDMS, and comprises four essential components: the cold reservoir, the cold-to-hot channel, the hot reservoir and the hot-to-cold channel. As schematically illustrated in Figure 6.1 (b), the device operates in four distinct steps. In step 1 - the OFF state - the fluid is cooled by remaining in contact only with the cold reservoir. Subsequently, in step 2, a magnetic field gradient is applied to promote the fluid's movement from the cold to the hot reservoir, and through the cold-to-hot channel. In step 3 - the ON state - the fluid is in the hot reservoir, absorbing the heat generated by the heat source. In step 4, the fluid is transferred through the hot-to-cold channel, and returns to the cold reservoir.

Consequently, the operation resumes to step 1, where the fluid can cool down, and release the heat previously absorbed. These four steps are repeated cyclically throughout the 2D MAFTS operation.

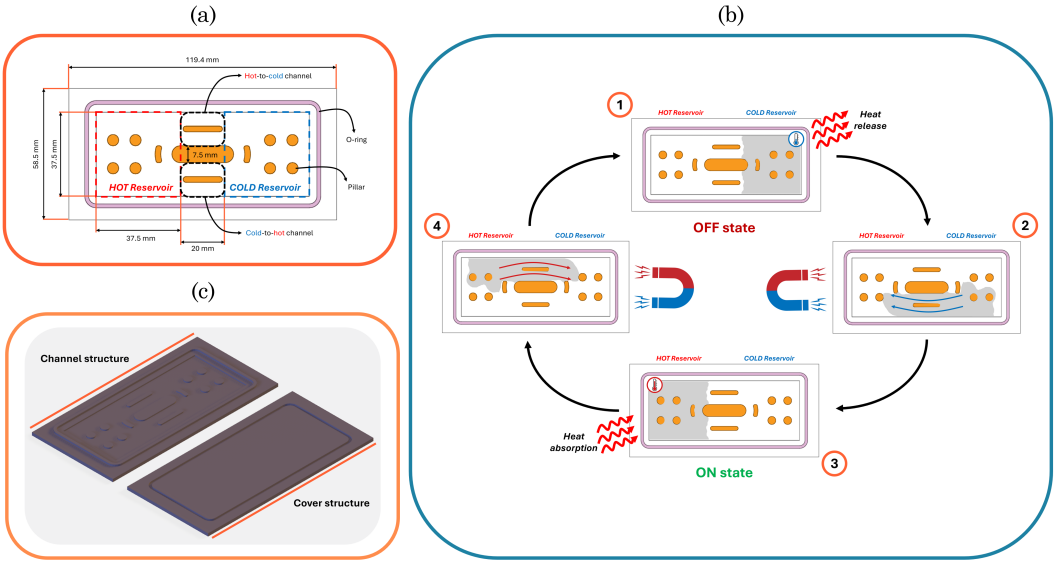

FIGURE 6.1: (a) Illustration of the structure design of the 2D MAFTS device. There are identified its six components, as well as their dimensions. The cold and hot reservoirs are denoted by blue and red dashed boxes, respectively. The cold-to-hot and the hot-to-cold channels are identified with black dashed boxes. The pillars and the o-ring are colored in orange and light pink, respectively. (b) Schematic illustration of the working principle of the device, consisting on a four-step cyclic operation. The blue and red arrows, depicted in steps 2 and 4, respectively, illustrate the fluid flow in those steps. (c) Illustration of the final 3D design of the two structures - channel and cover - that compose the 2D MAFTS device.

In the course of developing the channel design, a number of parameters required consideration. As primary requirement, the dimensions of the reservoirs were selected with the objective of successfully covering the entire surface of a typical chip package. As reference, the dimensions of an Intel Core i5 chip package, which measures $37.5\,\mathrm{mm} \times 37.5\,\mathrm{mm}$, were taken into account [125]. Secondly, the length of the cold-to-hot and hot-to-cold channels was selected to be $20\,\mathrm{mm}$, with the objective of minimizing the impact of the heat generated by the heat source on the temperature of the cold reservoir. Furthermore, pillar structures (depicted in orange in Figure 6.1 (a)) were incorporated into the reservoirs and channels, to prevent the collapse of the PDMS assembly over time [126]. The final design of the pillars was the result of successive refinements, to facilitate the reproducible production of the PDMS structure. The o-ring (depicted in pink in Figure 6.1 (a)) was introduced to prevent fluid leakage.

The 2D MAFTS device is composed of two different PDMS structures - the channel and cover structures. In Figure 6.1 (c) are depicted the final 3D models of these two structures.

Regarding the channel structure, a $0.8\,\mathrm{mm}$ height for the channel walls was determined, in order to accommodate $1\,\mathrm{mL}$ of fluid in each reservoir. The thickness of the o-ring was chosen to be of $1.2\,\mathrm{mm}$. In the cover structure, the hollow structure was designed to perfectly fit the o-ring.

6.1.2. Production method

The fabrication of a 2D MAFTS device necessitates the synthesis of two distinct PDMS structures (illustrated in Figure 6.1 (c)). The mechanical properties of PDMS enable the replication of each structure using suitable 3D-printed molds [127]. Once the structures have been produced, they are assembled together to form the device. The fluid is then introduced into the device through inlets punctured in the PDMS structures.

This section will present the complete fabrication procedure of a 2D MAFTS device. As depicted in Figure 6.2 (a), this procedure is comprised by four different stages: mold fabrication, PDMS structures fabrication, device assembly, and device fluid filling.

Mold fabrication

The design of the PDMS molds was developed using the functionalities of the AutoCAD software. The generated drawings were 3D-printed in a Snapmaker Artisan 3D printer, using polyactic acid (PLA) as filament. The melting point of this material ($150 - 160\,^{\circ}\mathrm{C}$ [128]), ensures the durability of the molds for repeated fabrication of the same PDMS structure. Subsequently, the molds were manually sanded to reduce their surface roughness.

PDMS structures fabrication

The PDMS was prepared by mixing the prepolymer and curing agent (SYLGARD 184 Silicone Elastomer Kit, from Dow) at a weight ratio of $7.5 : 1$. The mixture was degassed in a desiccator purged with a vacuum pump, to remove the air bubbles. Then, the PDMS was poured onto the 3D-printed molds. The PDMS-filled molds were once again degassed to remove air bubbles resultant from the pouring. After a thermal curing of $85\,^{\circ}\mathrm{C}$ for two hours, the PDMS was cut (using a sterile surgical blade) and peeled from the molds. In Figure 6.2 (b), is schematically illustrated the procedure for the fabrication of the PDMS structures. That figure also shows the molds filled with PDMS after curing, and the final PDMS structures.

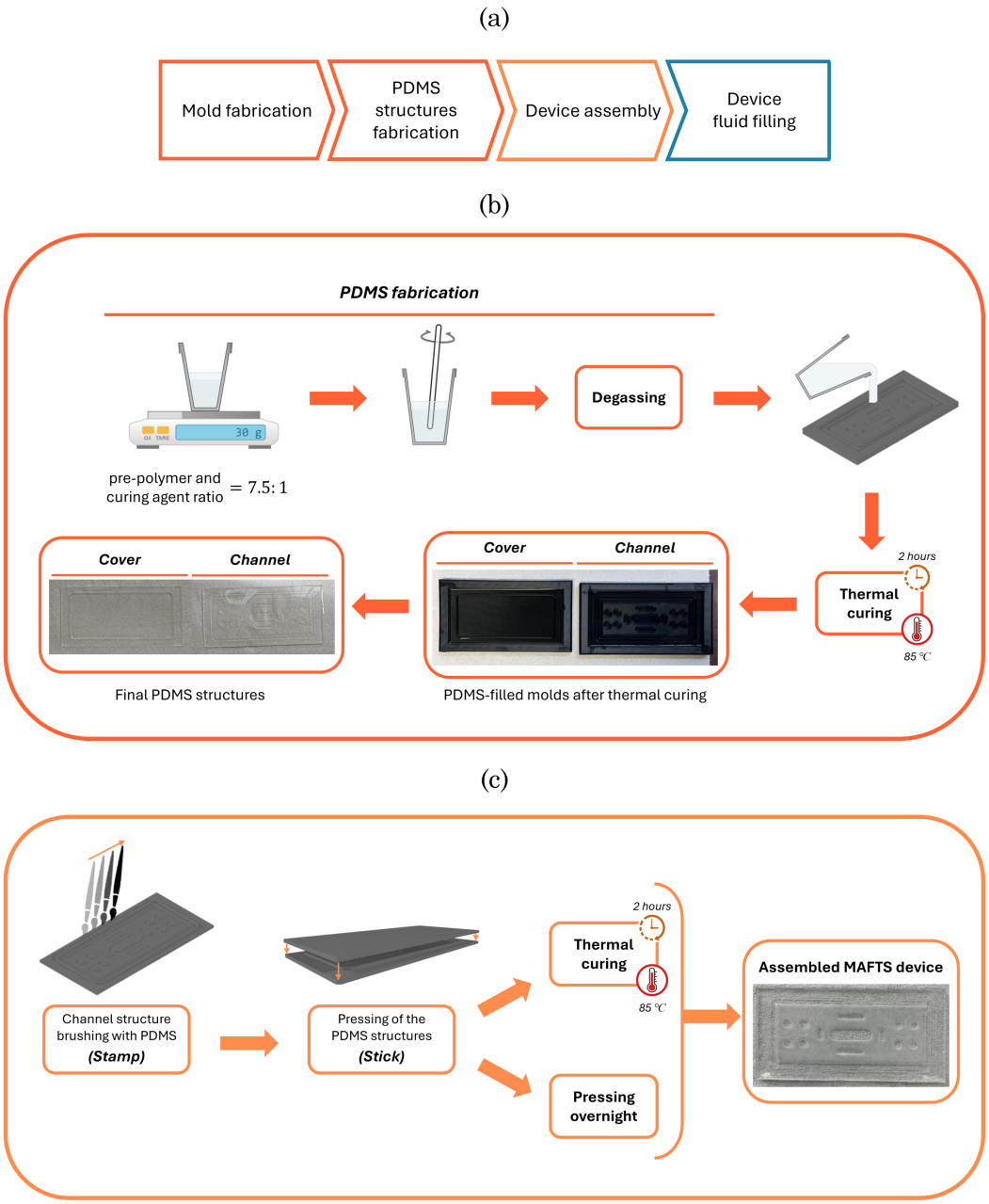

FIGURE 6.2: (a) Fabrication procedure of the 2D MAFTS device. (b) Illustration of the fabrication of the two PDMS structures: the channel and the cover. (c) Illustration of the 2D MAFTS device assembly procedure.

Device assembly

To complete the assembly of the MAFTS device, the two produced PDMS structures - the channel and the cover - must be bonded together. To achieve this, two (PDMS-PDMS) bonding techniques were tested: corona discharge surface treatment [129, 130], and stamp and stick (SAS) bonding [131].

The corona treatment was conducted in the CEMUP clean room facilities, using the Corona Plasma Treater from Everflow. Initially, the PDMS structures were rinsed with isopropyl alcohol, and wiped with paper towels. Afterwards, the electrode of the plasma treater was swept over each dried PDMS surface for a period of 6 minutes, with a distance of approximately $5\,\mathrm{mm}$ above the surface. The treated surfaces were then pressed together and left undisturbed overnight to ensure complete bonding took place. Nevertheless, some zones of the PDMS exhibited ineffective bonding, due to their considerable surface roughness. Thus, an alternative method was necessary.

The SAS treatment is a bonding technique which employs uncured PDMS as an adhesive. Figure 6.2 (c) illustrates the steps required to perform this technique, including an example of an assembled 2D MAFTS device. To start, the aforementioned PDMS production procedure was followed once again. Then, the surface of the channel structure that will be in contact with the cover structure was coated with a thin layer of PDMS by means of brushing - the stamp process. Afterwards, the cover structure was aligned with and placed on top of the coated channel - the stick process. Finally, the assembly was subjected to thermal curing at $85\,^{\circ}\mathrm{C}$ for two hours. Alternatively, as was tested, the two structures could be left pressed together overnight at room temperature, and still achieve a successful bonding. It is also noteworthy that this method offers the possibility of using uncured PDMS leftovers from the structures' fabrication.

Device fluid filling

In order to allow the filling of the device with the magnetic fluids, one inlet and one outlet were punctured through the cover structure and between the pillars situated in the cold and hot reservoirs, respectively. The desired volume of fluid is then transferred into the device using a syringe. Fluid removal is also conducted with a syringe.

6.2. Experimental setup

The performance of the 2D MAFTS device was evaluated in a home-made setup, which is schematically illustrated in Figures 6.3 (a) and (b). Figure 6.3 (a) presents a front view of the experimental apparatus, and a top view of the 2D MAFTS device (depicted within the orange dashed box). A Peltier element (TEC1-12706, 12V) with a heat sink is positioned on top of the hot reservoir, and serves as a heat source. The Peltier element is powered by a DC source (Aim TTi EX355P Programmable Bench Power Supply), whose output is controlled via serial communication. The temperature of the hot and cold reservoirs is monitored using two TCs, which are attached to the device surface with thermal paste and copper tape. The ambient temperature is also monitored with a thermocouple. These TCs are connected to a TC-08 thermocouple data logger (Pico Technology), and the data acquisition is controlled by a homemade software. In addition, a thermal image is recorded from the top of the device, using an Optris Xi 400 infrared (IR) camera, which is connected to the computer (PC).

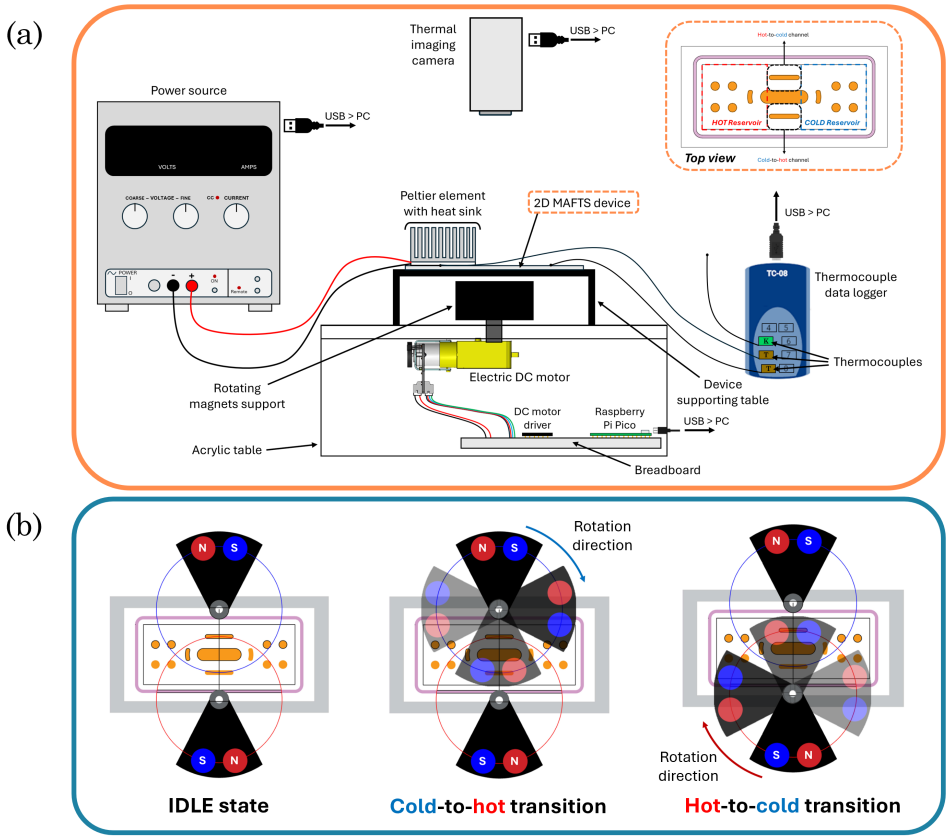

FIGURE 6.3: (a) Illustration of the setup used in the experiments conducted with the 2D MAFTS device. A top view scheme of the device is depicted in the top right orange dashed box. (b) Schematic of the magnet supports' three possible rotating states (IDLE, cold-to-hot transition, and hot-to-cold transition).

As previously outlined in Section 6.1.1, the 2D MAFTS device has a four-step cyclic operation. The aforementioned steps are identified based on the position of the fluid inside the device, as illustrated in Figure 6.1 (b). The position of the fluid is regulated by means of the rotational movement of two 3D-printed supports, with their top surface aligned parallel to and located $4\,\mathrm{mm}$ bellow the device base. The supports comprise two cavities, separated by an arc length of $5.2\,\mathrm{mm}$. Each one contains five N45 NdFeB disc magnets ($15 \times 3\,\mathrm{mm}$ in diameter and height) purchased from Supermagnete. In each cavity, the magnets exhibit the same polarity, which is opposite to that of the neighboring pile of magnets. The magnetic polarities considered for each magnet set are illustrated in Figure 6.3 (b). The intensity and the field line distribution of the magnetic field generated by diverse magnet arrangements were simulated using the software COMSOL Multiphysics. The analysis revealed that the presented magnetic configuration (whose simulated magnetic field distribution is illustrated in Figure A2, in Appendix A) is optimal for generating the requisite magnetic field gradient, which enables the directional movement of the fluid in accordance with the rotational motion of the magnets. This is in line with previous findings by Dogonay *et al.* [132]. This allows the fluid to transition between the hot and cold reservoirs. The rotation of each magnet support is driven by an electric DC motor (FIT0450 Micro DC Motor with Encoder-SJ01), whose actuation is controlled by a Raspberry Pi Pico microcontroller. The electrical circuit diagram is presented in Figure A3, in Appendix A. As illustrated in Figure 6.3 (b), there are three possibilities for the rotating states of the magnet supports. In the IDLE state, both supports are static. When a cold-to-hot reservoir fluid transition is intended, the top support rotates clockwise. When the fluid needs to move from the hot to the cold reservoir, the bottom support rotates clockwise.

The device starts operating when the hot reservoir reaches a constant temperature value $\left(T_{\mathrm{hot}}^{\mathrm{start}}\right)$. This triggers the top motor, starting the rotational motion of the top magnet support at a predefined speed - the cold-to-hot transition. Following a specific number of complete rotations, the motors return to the IDLE state for a certain period of time. Subsequently, the bottom motor initiates operation - the hot-to-cold transition, and the bottom support performs a specific number of rotations. Thereafter, the motors return to the IDLE state. This sequence is repeated over a specified time interval. Following this period, the power source is turned off, and the device is cooled down. All of these processes are fully automated with custom-developed software programs.

6.3. Performance evaluation

The two methods described in Section 4.4.2.1 were employed to produce ferromagnetic nanofluids, which were successfully injected into the 2D MAFTS device, as illustrated in Figure 6.4 (a). Immediately following the injection, the magnetic response of the fluid was evaluated by moving a set of permanent magnets over the surface of the device. The results of these tests are presented in Video V8 *. Although this video demonstrates some response of the fluid to the movement of the magnets, the extent of fluid motion was insufficient to facilitate a transition between the hot and cold reservoirs. Consequently, when tested in the performance evaluation setup, the fluid demonstrated no motion. This is primarily attributable to the magnetic force † strength being insufficient to overcome the viscous forces experienced by the fluid.

To augment the magnetic force experienced by the fluid, there are two potential avenues. On the one hand, the magnetization of the fluid can be augmented by embedding a greater mass of silica-coated Ni nanoparticles within the LM matrix. However, increasing the particle fraction in the LM can lead to an undesired enhancement of the fluid's viscosity and yield stress ‡ [75]. On the other hand, the magnetic field gradient can be enhanced by increasing the number of magnets in the setup. Reducing the intensity of the viscous forces can be more challenging. The primary contributor to these forces are the fluid's viscosity and its adhesion to the PDMS walls. In comparison to the ferromagnetic microfluid, the nanofluid demonstrated to exhibit significantly higher viscosity. This can be attributed to the higher weight percentage of Ga oxides present in the latter, resulting from the reaction of Ga with the oxygen present in the silica, which involves the Ni nanoparticles. Therefore, an alternative particle coating, such as silver [134], could potentially result in a less viscous ferromagnetic nanofluid. Alternatively, to reduce the adhesion of the fluid to the channel walls, another material could be considered for the development of the 2D MAFTS device. The utilization of PMMA could be a viable option for replication of the design. Moreover, the height of the channel walls could be increased to facilitate the motion of the fluid.

*Video V8 illustrating the ferromagnetic nanofluid magnetic tests after injection in the 2D MAFTS device is available at: `https://drive.google.com/file/d/1FLJJyTT9yrMb7_j1zpnd0-vmblZplr0T/view?usp=sharing`

†The magnetic force $\left(\vec{F}_m\right)$ felt by the particles is given by $\vec{F}_m = \mu_0 \nabla \left(\vec{H} \cdot \vec{M}\right)$, where μ_0 is the magnetic permeability of vacuum, $\vec{H}$ is the external field, and $\vec{M}$ is the magnetization of the particles [133].

‡The yield stress corresponds to the minimum force required to make the fluid flow.

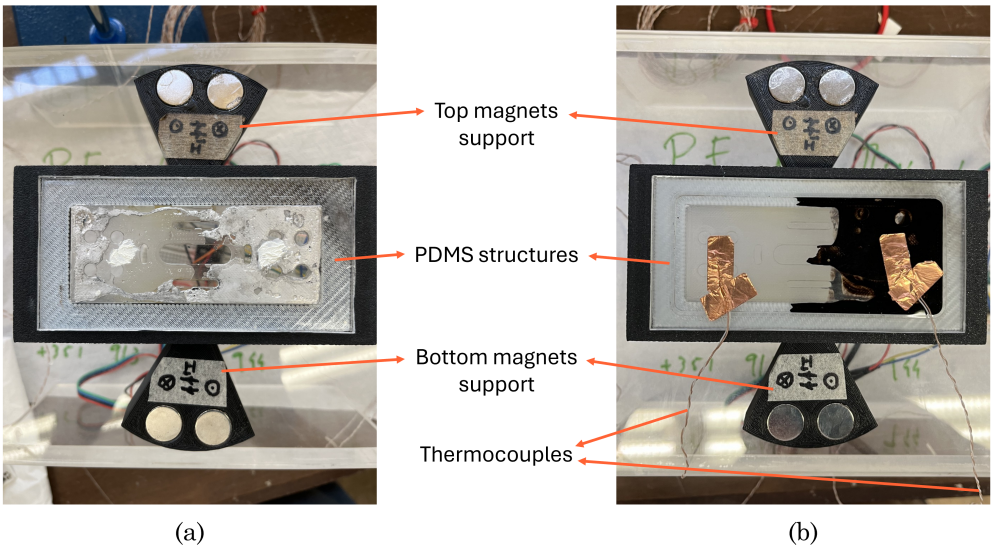

FIGURE 6.4: Illustration of the ferromagnetic nanofluid (a) and commercial ferrofluid (b) inserted within the 2D MAFTS device.

Although the performance of the 2D MAFTS device could not be evaluated using the produced ferromagnetic nanofluids, this was successfully achieved with a magnetite-based ferrofluid (M-FER-10 ferrofluid purchased from Supermagnete). A volume of $1\,\mathrm{mL}$ of this ferrofluid was incorporated into the device, as depicted in Figure 6.4 (b). The high fluidity and magnetic susceptibility characteristic of this ferrofluid enabled its movement between both reservoirs using the designed setup. Video V9 * provides an exemplification of the transition of this fluid from the cold to the hot reservoir, and vice versa.

Two different studies were performed for the ferrofluid-filled 2D MAFTS device. The first study examined the impact of the heat source average power $\left(\overline{P}\right)$ on the thermal performance of the device. For that purpose, trials were conducted for each $\overline{P}$ value ($0.32\,\mathrm{W}$, $1.12\,\mathrm{W}$ and $2.32\,\mathrm{W}$). In these trials, in order to ensure that the ferrofluid was completely transferred from one reservoir to the other, the associated motor was kept rotating during each device state. During the ON state, the top motor completed 10 full clockwise rotations, each one with an average time period of $5.5\,\mathrm{s}$ †. The same parameters were applied to the rotation of the bottom motor during the OFF state. Once the 10 rotations had been completed, both motors returned to the IDLE state for a period of $3\,\mathrm{s}$. This motor rotation mode is referred to as the no feedback mode. In addition, the performance of the device was also assessed for a different motor rotation mode - the feedback mode, at the

*Video V9 exemplifying the cold-to-hot and hot-to-cold transitions during a ferrofluid-filled 2D MAFTS device operation is available at: `https://drive.google.com/file/d/1KhzHchk_OPHQGD5FbbjC-w_44XxkwxEA/view?usp=sharing`

†This is the requisite time for the motors to complete a full clockwise rotation at their minimum rotational speed.

maximum studied $\overline{P}$ value of $2.32\,\mathrm{W}$. The differences between the operation of this mode, and the former, will be explained in greater detail in Section 6.3.3.

6.3.1. Performance evaluation trials

In Figure 6.5 (a), for a heat source average power $\left(\overline{P}\right)$ of $2.32\,\mathrm{W}$, is illustrated the temperature variation of the cold and hot reservoirs during a complete trial. Each trial is comprised of three stages: heating up until the hot reservoir reaches a constant temperature value $\left(T_{\text{hot}}^{\text{start}}\right)$, device operating (with a specific motor operating mode, in this case, the no feedback mode) and cooling. It is notorious that, during heating, the temperature variation of the cold reservoir is negligible in comparison to that of the hot reservoir. This demonstrates that, while the device is not operating, the reservoirs are thermally isolated from one another. This can be attributed to the low thermal conductivity of the PDMS ($0.15\,\mathrm{Wm^{-1}K^{-1}}$ [135]), combined with the length of the channels separating the reservoirs ($20\,\mathrm{mm}$).

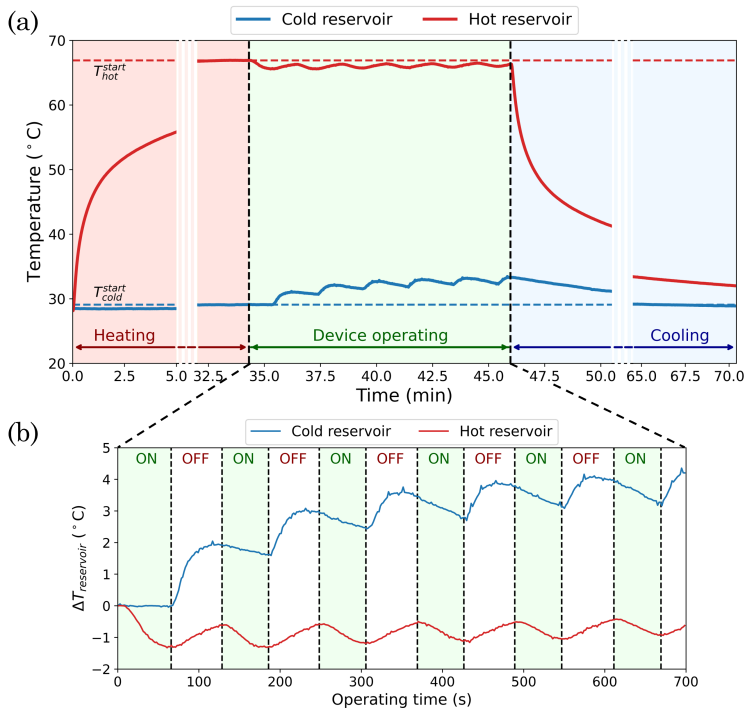

FIGURE 6.5: (a) Illustration of the temperature variation of the cold (solid blue line) and hot (solid red line) reservoirs throughout a complete trial, for the no feedback motor rotation mode, and for a heat source average power of $2.32\,\mathrm{W}$. The red and blue dashed horizontal lines identify the temperature values of the hot $\left(T_{\text{hot}}^{\text{start}}\right)$ and cold $\left(T_{\text{cold}}^{\text{start}}\right)$ reservoirs at the start of the device operation, respectively. (b) Temperature variation of each reservoir $(\Delta T_{\text{reservoir}})$ time dependence during the device operation, in the same trial. The different operating states (ON and OFF) of the device are identified.

In Figure 6.5 (b), it is emphasized the effect of the 2D MAFTS operation on the temperature variation of each reservoir ($\Delta T_{\text{reservoir}}(t) = T_{\text{reservoir}}(t) - T^{\text{start}}_{\text{reservoir}}$, where reservoir can correspond to hot or cold). As illustrated in that figure, in the ON state (ferrofluid within the hot reservoir) there is a decrease in ΔT_{hot}. This indicates that the heat generated by the heat source is being absorbed by the fluid. In the OFF state (ferrofluid within the cold reservoir), ΔT_{hot} increases due to the heating power from the heat source. On the other hand, in this state, initially ΔT_{cold} increases, denoting the release of the heat previously absorbed by the fluid, through the PDMS layer and to the environment. This behavior was consistently observed across all experimental trials, highlighting the proof of principle of the 2D MAFTS device. Nevertheless, for this particular value of $\overline{P}$, in the end of the OFF state it becomes evident that ΔT_{cold} begins to decline. This provides further evidence that the cold reservoir is only exchanging heat with the surroundings, not being directly influenced by the thermal power of the heat source. Furthermore, this final decrease in ΔT_{cold}, combined with the consistent increase in ΔT_{hot}, increases the amount of heat potentially absorbed * by the ferrofluid in the following ON state.

As a final note, the temperature variation of the hot and cold reservoirs during the cooling stage allows the specific heat of the device to be calculated. The methodology for this calculation can be found in the Appendix D. For this particular trial, a specific heat of $(1.69 \pm 0.03)\ \mathrm{kJ\,kg^{-1}K^{-1}}$ was determined. The value obtained is $16\,\%$ higher than that of PDMS ($1.46\,\mathrm{kJ\,kg^{-1}K^{-1}}$ [137]). This is due to the higher specific heat of the ferrofluid contained inside the device.

6.3.2. Influence of the heat source power on the performance

Analogously to the analysis in Section 5.2.2, to evaluate the influence of the heat source average power $\left(\overline{P}\right)$, it is considered the evolution of the ΔT_S with the operating time (t). This figure of merit quantifies the decrease of the temperature difference between the hot and cold reservoirs, in comparison to its initial value. In this case, ΔT_S is given by:

$$\Delta T_S\,(t) = \left(1 - \frac{\Delta T\,(t)}{\Delta T^{hot-cold}\,(0)}\right) \times 100 \tag{6.1}$$

where $\Delta T^{hot-cold}\,(0)$ corresponds to the starting value of $\Delta T^{hot-cold} = T_{hot} - T_{cold}$, and $\Delta T\,(t)$ is the value of $\Delta T^{hot-cold}$ averaged over a cycle centered at time t. In addition, it

*Considering a one-dimensional approximation to the Fourier's law of heat conduction [136], the heat absorbed will be proportional to the temperature difference between the hot and cold reservoirs $\left(\Delta T^{hot-cold}\right)$.

is also considered the minimum $\Delta T^{hot-cold}$ rate achieved in each trial. This constitutes a measure of the maximum heat exchange speed during the device operation.

The plots in Figure 6.6 (a) illustrate that the higher ΔT_S values were achieved for a $\overline{P}$ value of $2.32\,\mathrm{W}$. This effect is primarily related to the higher $\Delta T^{hot-cold}$ values achieved for the latter. For instance, at the start of the device operation the $\Delta T^{hot-cold}$ value was of $37.8\,^{\circ}\mathrm{C}$, while for the $\overline{P}$ values of $1.12\,\mathrm{W}$ and $0.32\,\mathrm{W}$, $\Delta T^{hot-cold}$ took a starting value of $22.2\,^{\circ}\mathrm{C}$ and $7.8\,^{\circ}\mathrm{C}$, respectively. As a consequence, the heat absorbed by the ferrofluid in each ON state is higher for the trial with $\overline{P} = 2.32\,\mathrm{W}$. In fact, the heat absorption is not only higher, but also faster, for increasing values of $\overline{P}$, as disclosed by the $\Delta T^{hot-cold}$ rate values presented in the plot in Figure 6.6 (b).

In addition, as can be seen from Figure 6.6 (a), the time evolution of ΔT_S exhibits different behaviors among the values of $\overline{P}$ under consideration. For the two higher values of $\overline{P}$, ΔT_S tends to increase with time into an asymptotic value. In contrast, for the lower $\overline{P}$, after the first $300\,\mathrm{s}$, ΔT_S starts a decreasing trend. As previously stated, the latter exhibits a smaller and slower rate of heat absorption. Consequently, after a certain period of time, the fluid's capacity to dissipate heat from the heat source gradually diminishes, resulting in a reduction in the value of ΔT_S over time.

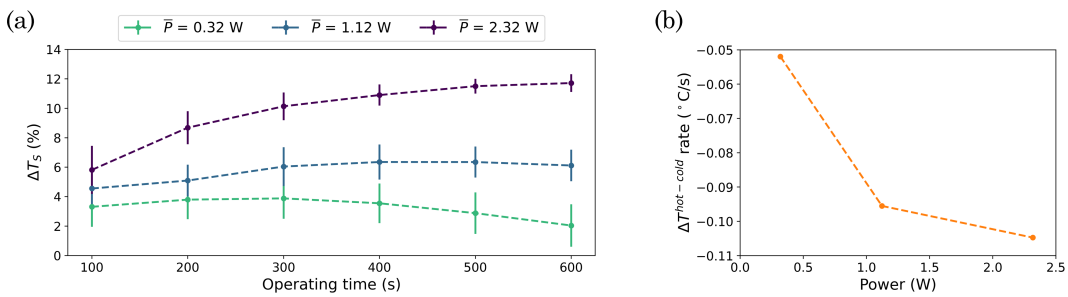

FIGURE 6.6: (a) Temperature span (ΔT_S, as defined in Equation 6.1) time evolution for the average heat source powers $\left(\overline{P}\right)$ tested on the 2D MAFTS device. (b) Minimum $\Delta T^{hot-cold}$ rate obtained during the MAFTS operation, for each power tested.

6.3.3. Influence of the motor operating mode on the performance

The performance of the device was evaluated for two different motor operating modes - the no feedback and the feedback mode, considering a $\overline{P}$ of $2.32\,\mathrm{W}$. As previously described, the no feedback mode, is completely temperature-independent.

In contrast, in the feedback mode, the number of rotations performed in each state depends on the evolution of the temperature value of the hot reservoir (T_{hot}). During the

ON state, the top motor performs complete rotations with an average time period of $5.5\,\mathrm{s}$, as in the no feedback mode. This continues until T_{hot} stops decreasing, at which point the top motor completes a full rotation and then stops. The final ON state temperature value of the hot reservoir is identified as $T_{\mathrm{hot}}^{\mathrm{ON}}$. Afterwards, in the OFF state, the bottom motor rotates until T_{hot} reaches a temperature value of $T_{\mathrm{hot}}^{\mathrm{OFF}} = T_{\mathrm{hot}}^{\mathrm{ON}} + \delta T$, where δT is a previously user-defined threshold value. Subsequently, the bottom motor completes its rotation, stops and then the top motor initiates a new rotation. This operation is repeated cyclically over a specified time interval. In Figure 6.7 (a) is illustrated the time evolution of T_{hot}, with the values of $T_{\mathrm{hot}}^{\mathrm{ON}}$ and $T_{\mathrm{hot}}^{\mathrm{OFF}}$ after the first cycle identified with horizontal dashed green and red lines, respectively.

As can be seen from the plots in Figure 6.7 (b), the ΔT_S time evolution was similar for both operating modes. The ΔT_S values for the no feedback mode were slightly higher, due to its higher values for $\Delta T^{hot-cold}$. Nevertheless, this is not significant, since for every operating time considered, the error bars are intersecting.

The major difference between the two operating modes is in the time evolution of the average ΔT_{hot} value in each cycle of the 2D MAFTS device $\left(\Delta T_{cycle}^{hot}\right)$. Figure 6.7 (c) illustrates the time evolution of ΔT_{cycle}^{hot} for both operating modes. From that figure it becomes evident that for the no feedback mode, even though there is an initial decline in ΔT_{cycle}^{hot}, this value subsequently increases over time. Conversely, for the feedback mode, ΔT_{cycle}^{hot} exhibits a decreasing trend towards a lower asymptotic value. This observation suggests that the feedback mode is a superior operating mode, as it facilitates the stabilization of the average temperature value of the heat source at a lower plateau.

6.3.4. Comparison with the performance of the 1D MAFTS device

In Table 6.1 are summarized the performance results for the 1D MAFTS device and the 2D MAFTS device (for both motor operating modes) under their optimal operating conditions. As previously stated, the ΔT_S quantifies the decrease in the temperature difference between the hot and cold terminals. In other words, it is a measure of the quality of the exchange of heat between those terminals. The minimum $\Delta T^{hot-cold}$ rate quantifies the rate of heat exchange. The ΔT_{min}^{hot} and the ΔT_{max}^{cold} correspond to the minimum and maximum values of ΔT_{hot} and ΔT_{cold}, respectively, attained during the operation of each device. The greater these two values are in absolute value, the more effective is the absorption and the rejection of heat in the hot and cold terminals, respectively. It should be noted that, in

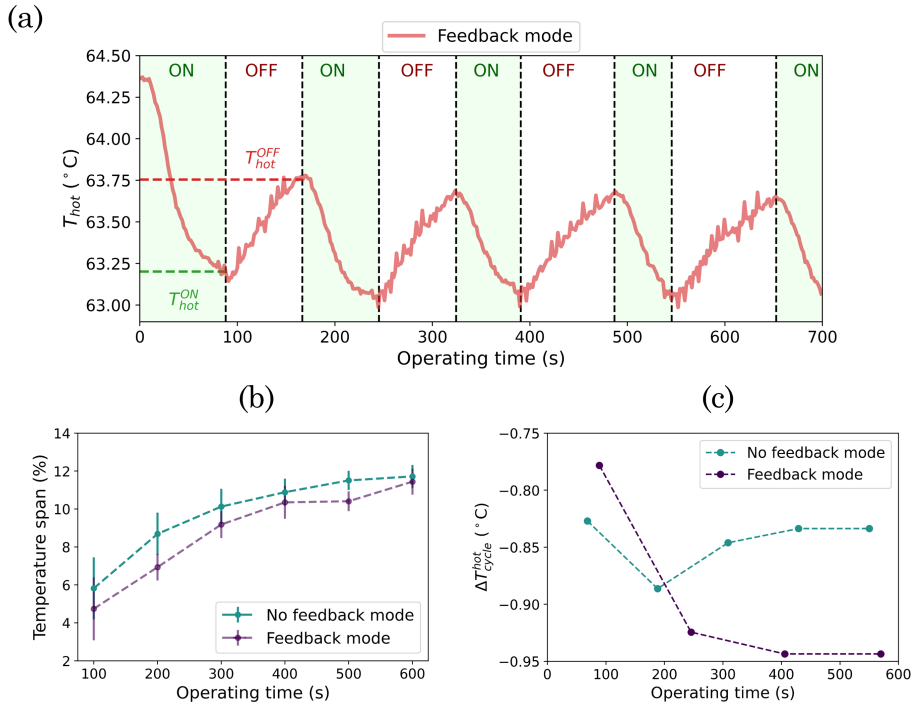

FIGURE 6.7: (a) Time dependence of the hot reservoir's temperature $\left(T^{hot}\right)$ during the device operation, for an average heat source power of $2.32\,\mathrm{W}$, and for the feedback motor operating mode. The different operating states (ON and OFF) of the MAFTS device are identified. The horizontal dashed green and red lines identify the final ON state $\left(T_{\mathrm{hot}}^{\mathrm{ON}}\right)$ and OFF state $\left(T_{\mathrm{hot}}^{\mathrm{OFF}}\right)$ temperature values of the hot reservoir, after the first operating cycle of the MAFTS device. (b) Temperature span (ΔT_S, as defined in Equation 6.1) time evolution for the two motor operating modes - the no feedback and the feedback modes - tested on the 2D MAFTS device. (c) Time evolution of the cycle average temperature variation of the hot reservoir $\left(\Delta T_{cycle}^{hot}\right)$ for both operating modes.

the case of the 1D MAFTS device, the terms "hot" and "cold" are equivalent to the heat source and sink, respectively.

TABLE 6.1: Performance comparison between the 1D and 2D MAFTS devices. In the case of the 1D MAFTS device, the terms "hot" and "cold" are equivalent to the heat source and sink, respectively

ΔT_S (%)	**minimum** $\Delta T^{hot-cold}$ **rate** (°C/s)	ΔT_{min}^{hot} (°C)	ΔT_{max}^{cold} (°C)
1D MAFTS device			
65 % FR and 0.5 Hz frequency			
19.8	−0.27	−0.43	1.71
2D MAFTS device			
no feedback mode and $\overline{P} = 2.32$ *W*			
11.7	−0.10	−1.33	4.35
feedback mode and $\overline{P} = 2.32$ *W*			
11.4	−0.08	−1.37	3.58

Table 6.1 reveals that the 1D MAFTS device exhibited the highest value for ΔT_S and the lowest value for the minimum $\Delta T^{hot-cold}$ rate. It can thus be concluded that this device

facilitates an enhanced heat exchange between its terminals. In contrast, the 2D MAFTS device exhibited the maximum absolute values for both ΔT_{min}^{hot} and ΔT_{max}^{cold}. Consequently, the utilization of the latter device enables an enhanced absorption and rejection of the heat at the hot and cold terminals, respectively.

In light of the aforementioned considerations, these devices should be selected with due consideration of the intended application. For instance, the 1D MAFTS should yield superior outcomes for applications that require an effective exchange of heat between the device terminals. One such application would be its integration into a thermal circuit to regulate the heat flux between two elements. Conversely, the 2D MAFTS results suggest that its deployment as a cooling technology would be more advantageous, as it can achieve a greater reduction in the temperature of the heat source.

7. Conclusions and future work

7.1. General conclusions

As the demand for higher computational power intensifies, driven primarily by advancements in AI and IT, the challenge of excessive heat generation has become increasingly prominent. Current cooling technologies are proving inadequate to manage the rising heat fluxes, thereby threatening the performance and longevity of electronic devices. The integration of Galinstan-based magnetic liquid metals into MAFTSs presents a promising avenue for enhancing thermal conductivity. Moreover, the application of magnetic fields allows for precise and efficient wireless regulation of heat fluxes, thereby improving heat dissipation and reducing the risk of device overheating.

In this thesis, we focused on the development of two MAFTS devices with distinct operating mechanisms, incorporating different magnetic liquid metals that synergistically combine the high thermal conductivity of Galinstan with the ferromagnetism of Ni micro (ferromagnetic microfluid) and nanoparticles (ferromagnetic nanofluid). The first MAFTS device integrates a ferromagnetic microfluid, which exhibits a 1D motion aligned with the gravitational force, whereas the second device was designed for 2D actuation of the ferromagnetic nanofluid. This study encompasses the fabrication and thorough characterization of the constituent materials of each magnetic liquid metal, the performance evaluation of the ferromagnetic microfluid-based 1D MAFTS device, and the design and fabrication of a new 2D MAFTS device along with a suitable evaluation apparatus. This thesis also demonstrates the potential of the 2D MAFTS device for thermal management applications through experiments with a commercial magnetite-based ferrofluid.

The synthesized magnetic liquid metals comprised a Galinstan matrix with a Ga/In/Sn composition of $(65.5 : 23.7 : 10.8)\ \mathrm{wt.\%}$, which slightly deviates from the target Ga/In/Sn $(68 : 22 : 10)\ \mathrm{wt.\%}$ composition. This variation resulted in an increased thermal conductivity of $25.5\,\mathrm{W\,m^{-1}\,K^{-1}}$, which is attributed to the higher In concentration relative to previously reported alloys. This study presents the first magnetization versus applied magnetic field characterization of the Galinstan, revealing a diamagnetic behavior with a mass magnetic susceptibility of $-6.23 \times 10^{-10}\,\mathrm{m^3\,kg^{-1}}$. This indicates that Galinstan alone contributes negligibly to the overall magnetic response of the magnetic liquid metals.

To fabricate the ferromagnetic microfluid, Ni microparticles, with an average particle size of $(16 \pm 8)\ \mu\mathrm{m}$, were embedded into the Galinstan within an inert Ar atmosphere. The methodology considered promotes the adhesion of the Galinstan to the magnetic particles, through the successive breaking and renewal of the LM oxide layer. This induced oxidation results in a slight reduction in thermal conductivity, in comparison to Galinstan, with values reaching approximately $21\,\mathrm{W\,m^{-1}\,K^{-1}}$. As disclosed by its room temperature magnetic curve, the microfluid, with a Ni concentration of $2.6\,\mathrm{wt.\%}$, exhibits a ferromagnetic behavior, thereby demonstrating that it can be remotely controlled through the application of an external magnetic field.

To test the viability of a Galinstan-based 1D MAFTS system for thermal management applications, the ferromagnetic microfluid was integrated into the 1D MAFTS device. Our findings revealed that, for each of the tested magnet movement frequencies and FRs, the device demonstrated effective control of the heat flux between heat source and sink. The 1D MAFTS heat dissipation was maximum for the lower FR ($65\,\%$) and higher frequency ($0.5\,\mathrm{Hz}$) tested. Under these optimal working conditions, a temperature span of $19.8\,\%$ and a switching ratio of 1.26 were achieved. The high boiling point of the base fluid suggests that the presented 1D MAFTS will have a longer operation lifespan at the same performance level, in comparison to currently available magnetically actuated alternatives.

Regarding the production of the ferromagnetic nanofluid, firstly a silica coating was applied to the Ni nanoparticles, with the objective of improving their compatibility with the oxide layer of the LM, thus facilitating their incorporation within the Galinstan matrix. The SEM images analysis revealed that, during the fabrication process, the silica did not adhere directly to the surface of the nanoparticles. Instead, an amorphous silica matrix was mixed and deposited within the particles' dispersion. As evidenced by their low-temperature isothermal magnetization versus field curves, the different batches of silica-coated Ni nanoparticles exhibited a silica concentration between 1.0 and $8.9\,\mathrm{wt.\%}$. The fabrication of the ferromagnetic nanofluid was achieved by embedding the silica-coated Ni nanoparticles into the Galinstan matrix, employing the same methodology as that utilized for the microfluid.

The ferromagnetic nanofluid was introduced into the 2D MAFTS device to evaluate its heat management performance. However, we were unable to facilitate the transition of the nanofluid between the hot and cold reservoirs, due to insufficient magnetic force strength

relative to the viscous forces experienced by the fluid. Despite this, the performance evaluation of the 2D MAFTS device was successfully accomplished with a magnetite-based ferrofluid. Our findings revealed that increased heat source power improved cooling performance, due to enhanced heat absorption and rejection. Indeed, for the higher average heat source power tested ($2.32\,\mathrm{W}$), a maximum temperature span of $11.7\,\%$ was achieved. This value is lower than that achieved for the 1D MAFTS device. Nevertheless, the 2D MAFTS device attained a maximum reduction of the temperature of the hot reservoir by $1.33\,^{\circ}\mathrm{C}$, surpassing the 1D MAFTS by $0.9\,^{\circ}\mathrm{C}$. Furthermore, an operating mode dependent on the evolution of the temperature of the hot reservoir enabled the stabilization of the average temperature value of the heat source at a value $0.95\,^{\circ}\mathrm{C}$ lower than its value before starting operation. These observations indicate that the 1D MAFTS may be more effective for applications requiring an efficient heat exchange between its terminals, whereas the 2D MAFTS may be better suited to effectively cooling down electronic components.

To conclude, to the best of our knowledge, this research has provided the first demonstration of the feasibility of Galinstan-based magnetic liquid metals for use in magnetically actuated TCDs. This has opened up a new range of possibilities for cooling electronic equipment.

7.2. Future work

The results obtained with the 1D MAFTS device constitute the first evidence of the integration of Galinstan-based magnetic liquid metals into magnetically actuated TCDs. However, further research is required to determine the optimal concentration of Ni microparticles that maximizes the performance of the ferromagnetic microfluid, particularly in terms of its magnetic and thermal transport properties. This strategy aims to fully leverage the advantages of the thermal conductivity of Galinstan, thereby advancing the development of an highly effective and durable remote and wireless thermal management technology for electronic components.

The 2D MAFTS device yielded promising results using a magnetite-based ferrofluid. The higher thermal conductivity of the Galinstan-based ferromagnetic nanofluid suggests that its incorporation into the device could potentially enhance its performance. Therefore, the following stage of our investigation will be to successfully manipulate the nanofluid within the 2D MAFTS channels. To achieve this, we have to guarantee that the magnetic forces acting on the fluid surpass the viscous forces. The most challenging but also the

most promising avenue of research is to reduce the intensity of the viscous forces. One potential solution is to reduce the fluid's oxidation and, thus, viscosity, by coating the Ni particles with silver [75]. Alternatively, exploring different materials for the fabrication of the 2D MAFTS device, such as PMMA, or increasing the height of the channel walls could reduce fluid adhesion and improve fluid dynamics.

Furthermore, to assess the feasibility of the 2D MAFTS in managing the heat fluxes generated by electronic equipment, which are projected to exceed $500\,\mathrm{W\,cm^{-2}}$ [6], further experimentation with higher values of heat source power is necessary. Additionally, the necessity of moving parts (rotating magnet supports) to facilitate the movement of the fluid restricts the device's application range. Consequently, future work will include the development of an alternative magnetic field gradient source. Potential solutions include the use of pairs of electromagnets, gradient coils [138, 139], or even the printing of coils directly into the PDMS structure [140, 141]. These new field gradient sources must be meticulously designed to minimize the effect of Joule heating on the temperature of the working fluid.

A. Appendix A - Supplementary multimedia

A1. Figures

A1.1. Morphological characterization of the commercial Nickel nanoparticles

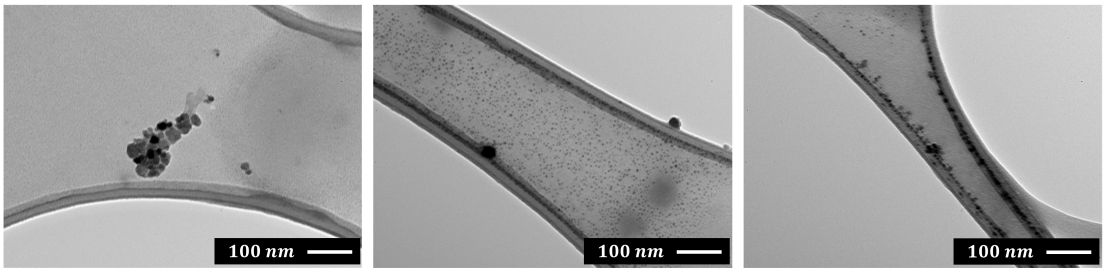

(a) (b) (c)

FIGURE A1: TEM images of the commercial Ni nanoparticles with $15000\times$ magnification and a $80\,\mathrm{kV}$ electron beam.

A1.2. 2D cooling experimental setup - Magnetic field distribution

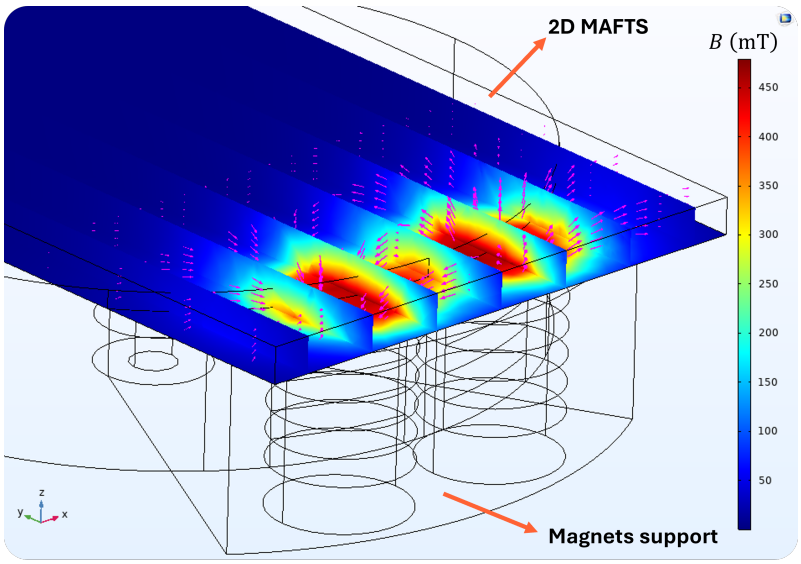

FIGURE A2: Results from the simulations of the magnetic field lines (pink arrows) and intensity (color surface plots) distribution produced by the magnetic configuration used in the 2D MAFTS setup. The simulations were performed using the COMSOL Multiphysics software.

A1.3. 2D cooling experimental setup - Electrical circuit diagram

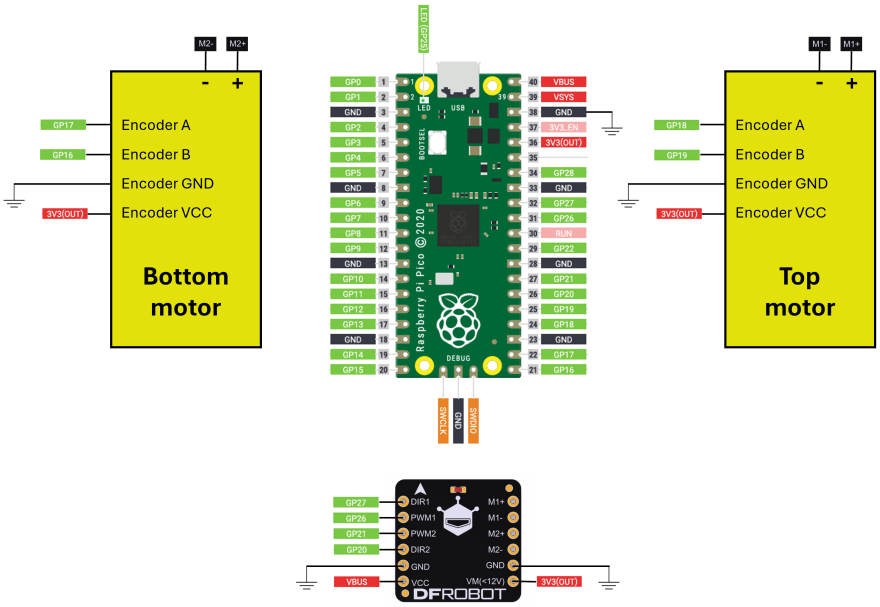

FIGURE A3: Schematic illustration of the electric circuit diagram considered for the control of the magnet supports rotation in the 2D MAFTS experimental setup.

B. Appendix B - Characterization of the silica-coated Ni nanoparticles

The purpose of this Appendix is to provide the characterization results of every silica-coated batch fabricated, and fully characterized throughout this thesis work. Even though 12 batches of silica-coated Ni nanoparticles were produced, only in samples number $2, 3, 5, 6, 9, 10, 11$ and 12, a complete characterization, comprising Raman, X-ray diffraction (XRD) and magnetometry measurements, was performed. Hence, the analysis bellow will be limited to these samples.

B1. Raman measurements

In every analyzed sample, the Raman measurements were performed in two different zones ($Z1$ and $Z2$), each of them evaluated with two increasing laser powers ($5\,\%$ and $10\,\%$). As was explained in Section 4.3.2, the existence of silica in a sample is clearly evidenced by a characteristic Raman profile, containing five pronounced Raman modes with wavenumbers ranging between $100 - 2000\,\mathrm{cm}^{-1}$. In Figure B1, are illustrated the Raman measurements where it was possible to conclude that the sample in analysis did contain silica. In some of them, the Raman peaks could be detected with both laser powers (P_{laser}), as was the case of samples number $6, 10, 11$ and 12. While in the rest, one needed a stronger P_{laser} of $10\,\%$ to detect the signal associated to the vibrations. For the latter, this can be related to a smaller amount of silica in the laser measuring spot. In Table B1, are summarized the position of the silica indicative peaks, which were identified in the data presented in Figure B1.

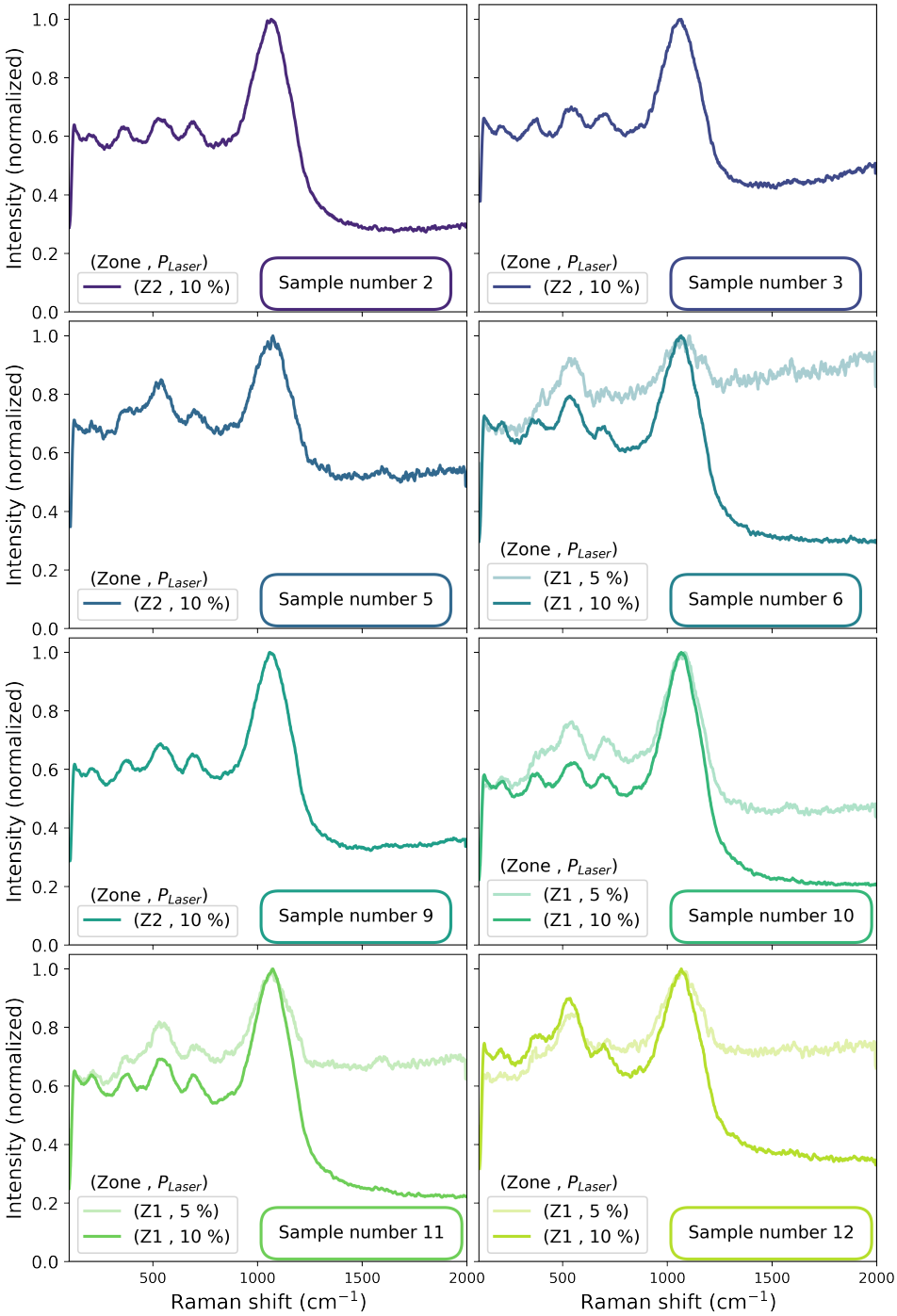

FIGURE B1: Normalized Raman spectra of the analyzed batches of silica-coated Ni nanoparticles, with the corresponding measuring zone and laser power (P_{laser}) identified.

TABLE B1: Position of the Raman peaks in the measurements where it was evidenced the presence of silica

Sample #	(Zone , P_{laser})	Peak wavenumber $\left(\mathrm{cm}^{-1}\right)$				
		Peak 1	Peak 2	Peak 3	Peak 4	Peak 5
2	(Z2 , 10)	196	361	525	695	1065
3	(Z2 , 10)	201	378	542	706	1067
5	(Z2 , 10)	207	389	540	697	1073
6	(Z1 , 5)	222	398	531	708	1067
	(Z1, 10)	209	355	536	700	1067
9	(Z2, 10)	211	374	536	690	1058
10	(Z1, 5)	211	399	545	697	1084
	(Z1, 10)	215	378	554	693	1067
11	(Z1, 5)	215	376	531	708	1068
	(Z1, 10)	207	380	532	693	1073
12	(Z1, 5)	203	372	542	713	1068
	(Z1, 10)	205	391	536	695	1067

B2. X-ray diffraction measurements

In Figure B2 are presented the room-temperature X-ray diffractograms of the silica-coated Ni nanoparticles, ranging $2\theta = 30^\circ - 110^\circ$. The Bragg peaks presented in those diffractograms denote the samples' polycrystalline nature. The minimal variation in the position of the Bragg peaks among the samples in analysis, signals that the silica deposition procedure did not affect their crystalline structure. This structure is believed to result from the contribution of three different crystallographic phases. Firstly, a dominant Ni face centered cubic ($\mathrm{Fm\overline{3}m}$ space group) phase [108] was indexed to the peaks at $2\theta = 44.5^\circ$ (111), 51.8° (200), 76.4° (220), 92.9° (311) and 98.4° (222). Secondly, a NiO face centered cubic (FCC) phase [112] was associated with the peaks at $2\theta = 37.1^\circ$ (111), 43.1° (200) and 62.6° (220). Finally, the peaks at $2\theta = 39.0^\circ$ (100), 41.7° (002) and 58.4° (102), were attributed to a Ni hexagonal close packed ($\mathrm{P6_3/mmc}$ space group) structure [119]. Considering these three crystallographic phases, structural Le Bail refinements were carried out. Table B2 summarizes the lattice parameters, and phase percentages, yielded from the refinement of each sample experimental data. It is important to note that the Ni FCC and hexagonal close packed (HCP) phases have common Bragg peaks. This results in an higher uncertainty in the phase percentage distributed between them.

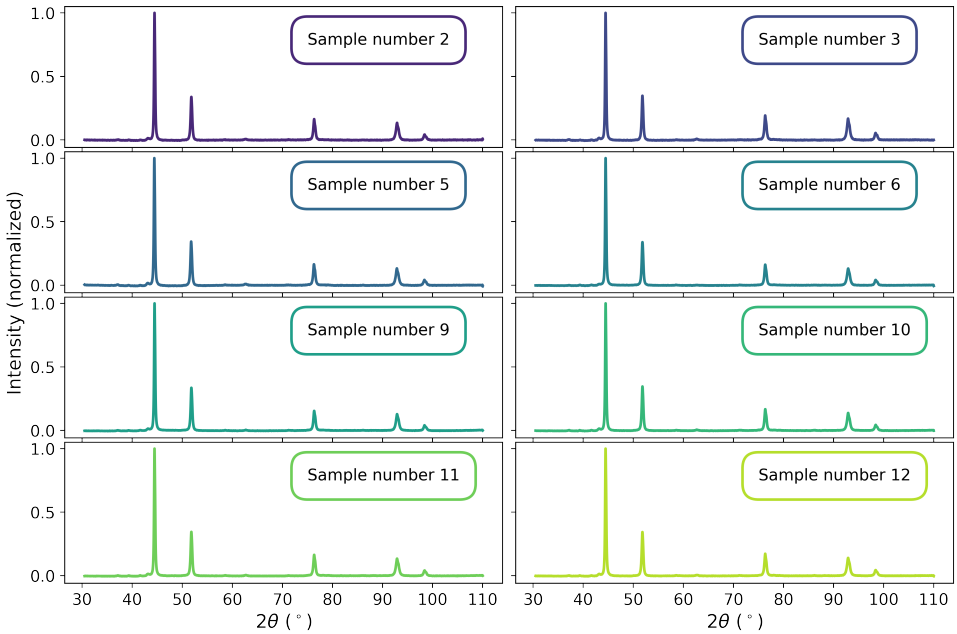

FIGURE B2: Room temperature X-ray diffractograms of the analyzed batches of silica-coated Ni nanoparticles.

TABLE B2: Lattice parameters and phase percentages yielded from the Le Bail refinements to the X-ray diffraction patterns of the analyzed batches of silica-coated Ni nanoparticles. The refinement considered three crystallographic phases: a Ni face centered cubic (FCC) phase, a NiO FCC phase and a Ni hexagonal close packed (HCP) phase

Sample	Crystallographic phases						
	Ni FCC		NiO FCC		Ni HCP		
	$a = b = c$ (Å)	phase %	$a = b = c$ (Å)	phase %	$a = b$ (Å)	c (Å)	phase %
2	3.53	91.9	4.19	0.9	2.66	4.33	7.2
3	3.53	91.5	4.19	0.6	2.66	4.33	7.8
5	3.52	78.5	4.19	0.7	2.66	4.33	20.8
6	3.52	78.4	4.14	1.1	2.66	4.38	20.5
9	3.52	94.2	4.18	0.7	2.66	4.33	5.2
10	3.52	89.7	4.19	0.4	2.66	4.33	9.8
11	3.52	95.7	4.18	0.6	2.66	4.33	3.6
12	3.52	77.3	4.19	0.8	2.66	4.33	21.9

B3. Magnetic measurements

The magnetization hysteresis curves, at $10\,\mathrm{K}$, of the silica-coated Ni nanoparticles are represented in Figure B3. At high fields, for every sample, the magnetization did not saturate asymptotically to a fixed value, due to the antiferromagnetic contribution from the NiO. This element, whose presence was disclosed by the Raman and XRD measurements, does not saturate in a $5\,\mathrm{T}$ field. Therefore, to remove this antiferromagnetic behavior, the slope of the magnetic curve, obtained for magnetic fields with strength higher than $2\,\mathrm{T}$, was subtracted to the sample's magnetization. As can be seen from the inserted plots in

Figure B3, the low-field magnetic response did not change after this treatment.

From the treated experimental data, it was possible to determine the saturation magnetizations (M_{sat}) and the coercive fields (H_c) of the samples in analysis. Moreover, by considering the expression presented in equation 4.1, from the ratio between the silica-coated particles' saturation magnetization values, and that of the commercial Ni nanoparticles $\left(M_{sat}^{\mathrm{Ni}} = 47.4 \pm 0.2\,\mathrm{Am^2kg^{-1}}\right)$, it was possible to estimate the wt.% of silica in each sample. The estimated parameters are summarized in Table B3.

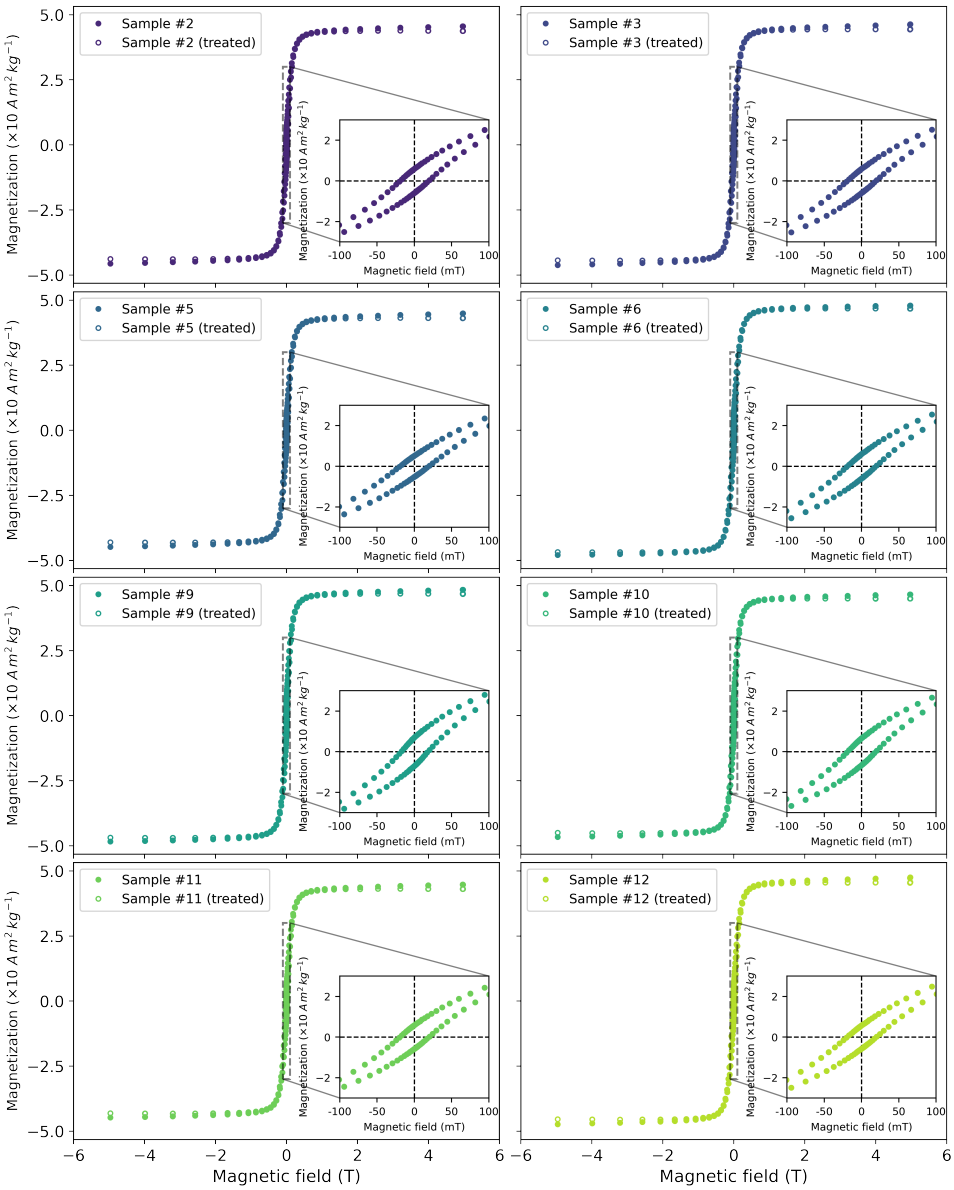

FIGURE B3: Magnetic response of the different batches of silica-coated Ni nanoparticles to varying magnetic fields within the range $[-5, 5]$ T, at $10\,\mathrm{K}$. The filled points correspond to the raw data, and the unfilled ones to the treated data, without the antiferromagnetic contribution from NiO. The inset corresponds to a zoom-in of the low-field range between $-50\,\mathrm{mT}$ and $50\,\mathrm{mT}$.

TABLE B3: Results from the magnetic characterization of the silica-coated Ni particles. This table includes the values estimated for their saturation magnetization (M_{sat}), wt.% of SiO_2 and coercive field (H_c)

Sample	2	3	5	6	9	10	11	12
M_{sat} $\left(\mathrm{Am^2kg^{-1}}\right)$	43.9	44.5	43.2	46.8	46.9	45.1	43.2	45.6
wt.% SiO_2	7.3	6.1	8.9	1.2	1.0	4.8	8.8	3.8
H_c (mT)	19.2	19.2	19.3	19.1	17.6	18.9	19.6	19.6

C. Appendix C - 1D MAFTS device thermal circuit model

To obtain the effective thermal conductivity of the 1D MAFTS device during its operation $\left(k_{eff}^{ON}\right)$, and while it is deactivated $\left(k_{eff}^{OFF}\right)$, we considered the thermal circuit presented in Figure C1. This model was developed under the assumption that the system is at the stationary state. Furthermore, considering that:

$$\begin{cases} Q = q_1 + q_2 \\ \Delta T^{so-si} = T_{source} - T_{sink} = q_2 \cdot R_{TS} \\ T_{source} - T_{amb} = q_1 \cdot R_{peltier-air} = q_2 \cdot (R_{TS} + R_{sink-air}) \end{cases}, \tag{C.1}$$

we can rearrange this set of equations to establish the following relation:

$$Q = \frac{\Delta T^{so-si}}{R_{TS}} \cdot \left(\frac{R_{TS} + R_{sink-air}}{R_{peltier-air}} + 1 \right) \tag{C.2}$$

The thermal resistances $R_{peltier-air}$ and $R_{sink-air}$ are associated with the heat exchanges of the Peltier element (heat source) and the heat sink with the air, respectively, which are established through a convective heat flow. The resistance R_{TS} is linked to the conduction of the heat between the heat source and heat sink, and through the 1D MAFTS. Taking this into account, these resistances can be calculated considering the following expressions:

$$\begin{cases} R_{peltier-air} = \dfrac{1}{h_{peltier-air} \cdot \left(A_{peltier} - A_{TS}\right)} \\ R_{sink-air} = \dfrac{1}{h_{sink-air} \cdot A_{TS}} \\ R_{TS} = \dfrac{L}{k_{eff} \cdot A_{TS}} \end{cases}, \tag{C.3}$$

where $A_{peltier} = 16\,\mathrm{cm}^2$ is the area of the Peltier element; $A_{TS} = 9\,\mathrm{cm}^2$ is the area of the thermal electrodes of the 1D MAFTS; $h_{peltier-air}$ is the convective heat transfer coefficient (CHTC) of the Peltier with air, which according to [142] takes a value of $25\,\mathrm{Wm^{-2}K^{-1}}$; $h_{sink-air}$ is the CHTC of copper under a low conductive flow of air, assuming a value of

$11.3\,\mathrm{Wm^{-2}K^{-1}}$ [143]; $L = 1\,\mathrm{cm}$ is the thickness of the 1D MAFTS device; and k_{eff} is the effective thermal conductivity of the 1D MAFTS.

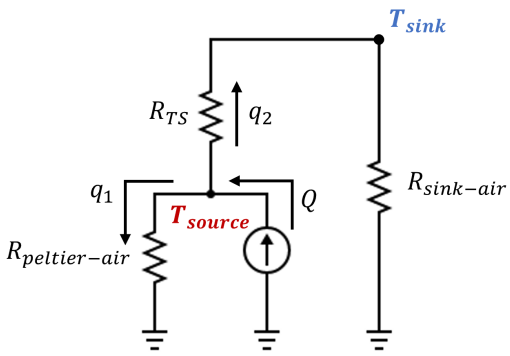

FIGURE C1: Thermal circuit model of the 1D MAFTS device at the stationary state.

Now, combining the expressions presented in Equations C.2 and C.3, we can rearrange Equation C.2 to establish a relation which allows the determination of k_{eff}:

$$k_{eff} = \frac{L}{1 + x \cdot a_{air}} \cdot \left(\frac{Q}{A_{TS} \cdot \Delta T^{so-si}} - h_{peltier-air} \cdot a_{air} \right) \tag{C.4}$$

where $x = h_{peltier-air}/h_{sink-air}$ and $a_{air} = \left(A_{peltier} - A_{TS}\right)/A_{TS}$.

The value of k_{eff} will depend on whether the 1D MAFTS device is $\left(k_{eff}^{ON}\right)$ or not $\left(k_{eff}^{OFF}\right)$ operating. The stationary conditions for such cases are achieved at the end and at the start of the 1D MAFTS operation, respectively. Therefore, to calculate k_{eff}^{ON}, one must consider the value of ΔT^{so-si} at the end of the device operation $\left(\Delta T_f^{so-si}\right)$. To determine k_{eff}^{OFF}, the value of ΔT^{so-si} at the start of the device operation $\left(\Delta T^{so-si}(0)\right)$ must be considered. Hence, the expressions to calculate k_{eff}^{ON} and k_{eff}^{OFF} are given by Equations C.5 and C.6, respectively.

$$k_{eff}^{ON} = \frac{L}{1 + x \cdot a_{air}} \cdot \left(\frac{Q}{A_{TS} \cdot \Delta T_f^{so-si}} - h_{peltier-air} \cdot a_{air} \right) \tag{C.5}$$

$$k_{eff}^{OFF} = \frac{L}{1 + x \cdot a_{air}} \cdot \left(\frac{Q}{A_{TS} \cdot \Delta T^{so-si}(0)} - h_{peltier-air} \cdot a_{air} \right) \tag{C.6}$$

D. Appendix D - Determination of the specific heat of the PDMS devices

The purpose of this Appendix is to provide the methodology for the determination of the specific heat of the PDMS devices, by considering the temperature variation of the hot and cold reservoirs during the cooling stages of the 2D MAFTS device trials.

According to the Newton's law of cooling, the cooling rate of a body (dT/dt) is directly proportional to the temperature difference between the body and the surrounding ambient $\left(\Delta T(t) = T(t) - T_{amb}\right)$, as stated by Equation D.1. Notice that it is assumed a constant temperature value for the ambient (T_{amb}). The solution of the differential equation presented in Equation D.1 is given by Equation D.2, which dictates that $\Delta T(t)$ follows an exponential decay with time, at a time constant τ. Under the condition of an uniform temperature distribution inside the body, the time constant of the system can be given by Equation D.3, where m_{body} and c_{body} are the mass and the specific heat capacity of the body, respectively, A_{surface} corresponds to the surface area exposed to the ambient, and h_{amb} is the average heat transfer coefficient between the surroundings and the surface of the body. [136, 144–146]

$$\frac{dT}{dt} = \frac{d\Delta T}{dt} = -\frac{1}{\tau}\Delta T(0) \tag{D.1}$$

$$\Delta T(t) = \Delta T(0)\,\exp\left(-\frac{t}{\tau}\right) \tag{D.2}$$

$$\tau = \frac{m_{\text{body}}\,c_{\text{body}}}{A_{\text{surface}}\,h_{amb}} \tag{D.3}$$

Taking this into consideration, it is possible to estimate the specific heat capacity from the time evolution of the hot and cold reservoirs' temperature during the cooling stage of a performance evaluation trial for the 2D MAFTS device. For such, the trial with an average heat source power of $2.32\,\mathrm{W}$, and with the motors operating in the no feedback mode was considered.

The first step is to identify the time interval in which the exponential temperature variation regime is valid. As illustrated in Figure D1, the temperature suffered an exponential decay only after the first 12 minutes of cooling. The second step is to determine the time constant

characteristic of each reservoirs cooling $(\tau_{\text{reservoir}})$. For such, a linear fit to $\ln[\Delta T](t)$ was performed. From the slope of the fitted curve $(a_{\text{reservoir}})$, it was possible to determine $\tau_{\text{reservoir}}$, as given by:

$$\tau_{\text{reservoir}} = -\frac{1}{a_{\text{reservoir}}}. \tag{D.4}$$

The values of $1028\,\text{s}$ and $738\,\text{s}$ were obtained for τ_{hot} and τ_{cold}, respectively, as depicted in the equations from the text boxes inserted in the plots from Figure D1. The specific heat of the device was then obtained from the data of each reservoirs' temperature variation $(c_{\text{reservoir}})$, by considering Equation D.3. For such, the mass and the surface area of the device considered were $m_{\text{body}} = 30\,\text{g}$ and $A_{\text{surface}} = 6988\,\text{mm}^2$, respectively. The heat transfer coefficient of the surroundings was considered to be that of air, under low speed flow over a surface ($h_{amb} = 10\,\text{W}\,\text{m}^{-2}\,\text{K}^{-1}$ [147]). The values obtained for c_{hot} and c_{cold} are presented in Table D1. Considering their average value, a specific heat of $(1.69 \pm 0.03)\ \text{kJ}\,\text{kg}^{-1}\,\text{K}^{-1}$ was determined for the device. The value obtained is $16\,\%$ higher than that of PDMS ($1.46\,\text{kJ}\,\text{kg}^{-1}\text{K}^{-1}$ [137]). This is due to the higher specific heat of the ferrofluid contained inside the device.

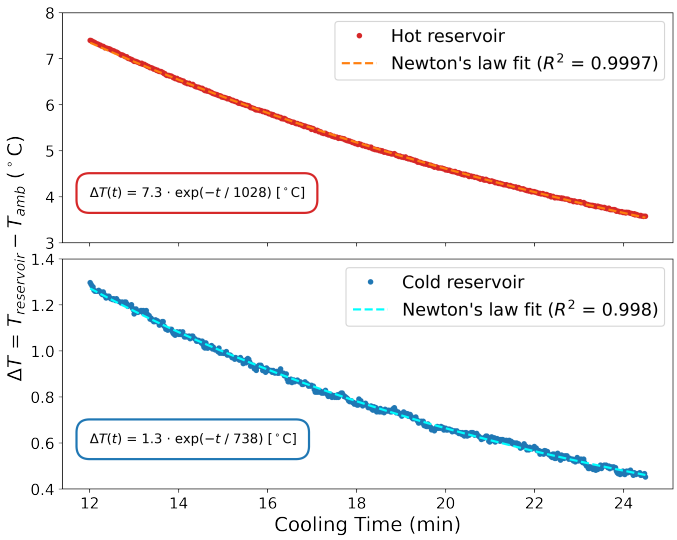

FIGURE D1: Temperature variation of the temperature of the hot (red dots) and cold (blue dots) reservoirs relative to the ambient (ΔT), during their cooling stage. The dashed lines represent the fit of the data to an exponential temperature decay, as suggested from Newton's law of cooling. Inside the red and blue boxes are presented the equations of cooling obtained for the hot and cold reservoirs, respectively.

TABLE D1: Results from the determination of the specific heat of the PDMS

Reservoir	Hot	Cold	*Average*
Specific heat $(\mathrm{kJ}, \mathrm{kg}^{-1}, \mathrm{K}^{-1})$	1.667 ± 0.001	1.719 ± 0.003	1.69 ± 0.03

References

[1] *Ondrej Burkacky et al., 29 March 2024, Generative AI: The next S-curve for the semiconductor industry?, McKinsey & Company, accessed on 18 august 2024*, Std. [Online]. Available: https://www.mckinsey.com/industries/semiconductors/our-insights/generative-ai-the-next-s-curve-for-the-semiconductor-industry [Cited on page 3.]

[2] G. Moore, "Cramming more components onto integrated circuits," *Proceedings of the IEEE*, vol. 86, no. 1, pp. 82–85, Jan. 1998. [Cited on page 3.]

[3] *International Roadmap for Devices and Systems (IRDS) 2023 Edition - More Moore*, Std., 2023, accessed 18 August 2024. [Online]. Available: https://irds.ieee.org/editions/2023 [Cited on page 3.]

[4] K. Klinar, T. Swoboda, M. Muñoz Rojo, and A. Kitanovski, "Fluidic and mechanical thermal control devices," *Advanced Electronic Materials*, vol. 7, no. 3, Dec. 2020. [Cited on pages 6, 7, 8, and 61.]

[5] A. L. Moore and L. Shi, "Emerging challenges and materials for thermal management of electronics," *Materials Today*, vol. 17, no. 4, pp. 163–174, May 2014. [Cited on pages 3 and 6.]

[6] Z. Li, H. Luo, Y. Jiang, H. Liu, L. Xu, K. Cao, H. Wu, P. Gao, and H. Liu, "Comprehensive review and future prospects on chip-scale thermal management: Core of data center's thermal management," *Applied Thermal Engineering*, vol. 251, p. 123612, Aug. 2024. [Cited on pages 3, 20, and 80.]

[7] *Communication from the Commission to the European Parliament, the European Council, the Council, the European Economic and Social Committee and the Committee of the Regions - A new Circular Economy Action Plan for a cleaner and more competitive Europe*, European Comissions Std., 2020. [Online]. Available: https://eur-lex.europa.eu/legal-content/EN/TXT/?qid=1583933814386&uri=COM:2020:98:FIN [Cited on page 3.]

[8] *Communication from the Commission to the European Parliament, the European Council, the Council, the European Economic and Social Committee and the*

Committee of the Regions- The European Green Deal, European Comissions Std., 2019. [Online]. Available: https://eur-lex.europa.eu/resource.html?uri=cellar:b828d165-1c22-11ea8c1f-01aa75ed71a1.0002.02/DOC_1&format=PDF [Cited on page 3.]

[9] *19 April 2023, Intel Dives into the Future of Cooling, intel, accessed on 18 august 2024*, Std. [Online]. Available: https://www.intel.com/content/www/us/en/newsroom/news/intel-dives-into-future-of-cooling.html [Cited on page 3.]

[10] *Robert Curtis et al., 3 March 2023, The Future of Server Cooling - Part 2: New IT hardware Features and Power Trends, Dell, accessed on 18 august 2024*, Std. [Online]. Available: https://infohub.delltechnologies.com/en-us/p/the-future-of-server-cooling-part-2-new-it-hardware-features-and-power-trends-1/ [Cited on page 3.]

[11] Vivian M. Andrade and Claudia R. Fernandes and Joana S. Teixeira and Clara Pereira and Ana L. Pires and Daniel J. Silva and Joao Ventura and Joana Oliveira, "High-performance magnetic thermal switch based on MnFe2O4/Ethylene Glycol:Water refrigerant dispersion," *Energy*, vol. 283, p. 129123, nov 2023. [Cited on pages 4, 6, 8, and 61.]

[12] C. Rodrigues, M. Dias, L. Martins, D. Silva, J. Araújo, J. Oliveira, A. Pereira, and J. Ventura, "A magnetically-activated thermal switch without moving parts," *Energy Conversion and Management*, vol. 197, p. 111881, Oct. 2019.

[13] G. Wehmeyer, T. Yabuki, C. Monachon, J. Wu, and C. Dames, "Thermal diodes, regulators, and switches: Physical mechanisms and potential applications," *Applied Physics Reviews*, vol. 4, no. 4, p. 041304, Dec. 2017. [Cited on pages 4, 6, and 7.]

[14] L. Shi, Y. Hu, and Y. He, "Magneto-responsive thermal switch for remote-controlled locomotion and heat transfer based on magnetic nanofluid," *Nano Energy*, vol. 71, p. 104582, may 2020. [Cited on pages 9, 10, and 61.]

[15] N. Petelin, K. Vozel, K. Klinar, and A. Kitanovski, "The numerical study on performance evaluation of a thermal switch capacitor in a magnetocaloric cooling device," *iScience*, vol. 25, no. 12, p. 105517, Dec. 2022. [Cited on pages 4, 5, and 6.]

[16] T. Yang, B. Kwon, P. B. Weisensee, J. G. Kang, X. Li, P. Braun, N. Miljkovic, and W. P. King, "Millimeter-scale liquid metal droplet thermal switch," *Applied Physics Letters*, vol. 112, no. 6, feb 2018. [Cited on pages 4, 6, and 7.]

[17] I. A. de Castro, A. F. Chrimes, A. Zavabeti, K. J. Berean, B. J. Carey, J. Zhuang, Y. Du, S. X. Dou, K. Suzuki, R. A. Shanks, R. Nixon-Luke, G. Bryant, K. Khoshmanesh, K. Kalantar-zadeh, and T. Daeneke, "A gallium-based magnetocaloric liquid metal ferrofluid," *Nano Letters*, vol. 17, no. 12, pp. 7831–7838, Nov. 2017. [Cited on pages 4, 11, 12, 13, 14, 29, 31, 34, 47, and 61.]

[18] M. L. V. Ramires, C. A. N. de Castro, Y. Nagasaka, A. Nagashima, M. J. Assael, and W. A. Wakeham, "Standard reference data for the thermal conductivity of water," *Journal of Physical and Chemical Reference Data*, vol. 24, no. 3, pp. 1377–1381, may 1995. [Cited on pages 4, 11, and 12.]

[19] Y. Plevachuk, V. Sklyarchuk, S. Eckert, G. Gerbeth, and R. Novakovic, "Thermophysical properties of the liquid ga–in–sn eutectic alloy," *Journal of Chemical Engineering Data*, vol. 59, no. 3, pp. 757–763, Feb. 2014. [Cited on pages 11, 12, 34, and 61.]

[20] S. Handschuh-Wang, T. Gan, M. Rauf, W. Yang, F. J. Stadler, and X. Zhou, "The subtle difference between galinstan (r) and eutectic GaInSn," *Materialia*, vol. 26, p. 101642, dec 2022. [Cited on pages 11, 12, 31, and 32.]

[21] W. Kong, Z. Wang, M. Wang, K. C. Manning, A. Uppal, M. D. Green, R. Y. Wang, and K. Rykaczewski, "Oxide-Mediated Formation of Chemically Stable Tungsten–Liquid Metal Mixtures for Enhanced Thermal Interfaces," *Advanced Materials*, vol. 31, no. 44, Sep. 2019. [Cited on pages 4, 11, 12, 34, and 61.]

[22] Y. Chang, *Our patented process brings exotic liquid metal thermal compound to new ROG gaming laptops*, Republic of Gamers Std., Apr. 2020, accessed 26 September 2023. [Online]. Available: https://rog.asus.com/articles/technologies/patented-process-brings-exotic-liquid-metal-thermal-compound-to-new-rog-gaming-laptops/ [Cited on page 4.]

[23] B. Sagan, *PS5 Liquid Metal Cooling - Problem, or Low Temperatures Guaranteed?*, gamepressure Std., Oct. 2020, accessed 26 September 2023. [Online]. Available: https://www.gamepressure.com/editorials/ps5-liquid-metal-cooling-problem-or-low-temperatures-guaranteed/zf339 [Cited on page 4.]

[24] S. Chen, H.-Z. Wang, R.-Q. Zhao, W. Rao, and J. Liu, "Liquid Metal Composites," *Matter*, vol. 2, no. 6, pp. 1446–1480, jun 2020. [Cited on pages 4 and 13.]

[25] J. B. Puga, B. D. Bordalo, D. J. Silva, M. M. Dias, J. H. Belo, J. P. Araújo, J. C. Oliveira, A. M. Pereira, and J. Ventura, "Novel thermal switch based on magnetic nanofluids with remote activation," *Nano Energy*, vol. 31, pp. 278–285, Jan. 2017. [Cited on pages 5, 7, 8, 9, 55, and 60.]

[26] T. Yang, T. Foulkes, B. Kwon, J. G. Kang, P. V. Braun, W. P. King, and N. Miljkovic, "An integrated liquid metal thermal switch for active thermal management of electronics," *IEEE Transactions on Components, Packaging and Manufacturing Technology*, vol. 9, no. 12, pp. 2341–2351, Dec. 2019. [Cited on page 6.]

[27] N. Petelin, M. Kalin, and A. Kitanovski, "A conceptual design of a thermal switch capacitor in a magnetocaloric device: experimental characterization of properties and simulations of operating characteristics," *Journal of Physics: Energy*, vol. 5, no. 3, p. 035007, Jul. 2023. [Cited on pages 6 and 7.]

[28] K. Klinar and A. Kitanovski, "Thermal control elements for caloric energy conversion," *Renewable and Sustainable Energy Reviews*, vol. 118, p. 109571, Feb. 2020. [Cited on pages 6 and 8.]

[29] T. Swoboda, K. Klinar, A. S. Yalamarthy, A. Kitanovski, and M. Muñoz Rojo, "Solid-State Thermal Control Devices," *Advanced Electronic Materials*, vol. 7, no. 3, Nov. 2020. [Cited on page 6.]

[30] J. Ma, X. Lin, M. Xian, X. Ke, D. Lu, Y. Yao, T. Tao, B. Liang, and S.-G. Lu, "High performance electrostatically driven thermal switch incorporated with a mini-channel cooling," *Energy Sources, Part A: Recovery, Utilization, and Environmental Effects*, pp. 1–16, Aug. 2020. [Cited on page 7.]

[31] K. Klinar, K. Vozel, T. Swoboda, T. Sojer, M. Muñoz Rojo, and A. Kitanovski, "Ferrofluidic thermal switch in a magnetocaloric device," *iScience*, vol. 25, no. 2, p. 103779, Feb. 2022. [Cited on page 8.]

[32] S. Sütterlin, D. Bölke, M. Ehresmann, N. Heinz, J. Dietrich, B. Karahan, M. Kob, M. O'Donohue, C. Korn, S. Grossmann, D. Philipp, M. Steinert, D. Acker, Y. Remane, P. Kreul, M. Schneider, S. Zajonz, B. Wank, F. Turco, M. Buchfink, E. Gutierrez, S. Hofmann, S. Ruffner, A. Wagner, L. Breitenbücher, F. Schäfer, G. Herdrich, and S. Fasoulas, "Fargo: validation of space-relevant ferrofluid applications on the iss," *CEAS Space Journal*, Mar. 2024. [Cited on pages 8 and 61.]

[33] B. Karahan, M. Kob, S. Sütterlin, J. Dietrich, D. Bölke, M. Steinert, N. Heinz, E. Gutierrez, S. Großmann, D. Philipp, F. Turco, M. Buchfink, C. Korn, S. Zajonz, M. O'Donohue, Y. Remane, P. Kreul, M. Schneider, D. Acker, and G. Herdrich, "Recent results of ferrofluid iss experiments to enable sustainable space activities," 06 2023.

[34] J. Dietrich, M. Kob, S. Zajonz, C. Korn, B. Karahan, S. Sütterlin, N. Heinz, D. Bölke, S. Großmann, D. Philipp, F. Turco, M. Buchfink, M. O'Donohue, Y. Remane, P. Kreul, M. Schneider, M. Steinert, E. Gutierrez, D. Acker, and G. Herdrich, "Scientific results of fargo -a verification of novel ferrofluid systems on the iss," 10 2023. [Cited on page 8.]

[35] V. M. Andrade, C. R. Fernandes, D. J. Silva, J. S. Teixeira, C. R. Pereira, R. Duarte, A. L. Pires, J. Ventura, and J. Oliveira, "Magnetic refrigeration enhanced by magnetically-activated thermal switch: An experimental proof-of-concept," *International Journal of Refrigeration*, vol. 164, pp. 210–217, Aug. 2024. [Cited on page 8.]

[36] D. Wang, Y. Hou, J. Tang, J. Liu, and W. Rao, "Liquid metal as energy conversion sensitizers: Materials and applications," *Advanced Science*, Mar. 2024. [Cited on pages 10 and 14.]

[37] A. Zavabeti, J. Z. Ou, B. J. Carey, N. Syed, R. Orrell-Trigg, E. L. H. Mayes, C. Xu, O. Kavehei, A. P. O'Mullane, R. B. Kaner, K. Kalantar-zadeh, and T. Daeneke, "A liquid metal reaction environment for the room-temperature synthesis of atomically thin metal oxides," *Science*, vol. 358, no. 6361, pp. 332–335, Oct. 2017. [Cited on page 10.]

[38] T. Daeneke, K. Khoshmanesh, N. Mahmood, I. A. de Castro, D. Esrafilzadeh, S. J. Barrow, M. D. Dickey, and K. Kalantar-zadeh, "Liquid metals: fundamentals and applications in chemistry," *Chemical Society Reviews*, vol. 47, no. 11, pp. 4073–4111, 2018. [Cited on pages 10, 12, 26, 30, 34, and 61.]

[39] K. Ma and J. Liu, "Liquid metal cooling in thermal management of computer chips," *Frontiers of Energy and Power Engineering in China*, vol. 1, no. 4, pp. 384–402, Oct. 2007. [Cited on pages 10, 13, 14, 18, and 19.]

[40] S. Liu, K. Sweatman, S. McDonald, and K. Nogita, "Ga-based alloys in microelectronic interconnects: A review," *Materials*, vol. 11, no. 8, p. 1384, Aug. 2018. [Cited on page 10.]

[41] Y. Deng, Y. Jiang, and J. Liu, "Liquid metal technology in solar power generation - Basics and applications," *Solar Energy Materials and Solar Cells*, vol. 222, p. 110925, Apr. 2021. [Cited on pages 10 and 11.]

[42] J. Liu and Y. Zhou, "A computer chip cooling method which uses low melting point metal and its alloys as the cooling fluid," *China Patent*, vol. 2131419, no. 10, 2002. [Cited on pages 10 and 11.]

[43] Y.-G. Deng and J. Liu, "Corrosion development between liquid gallium and four typical metal substrates used in chip cooling device," *Applied Physics A*, vol. 95, no. 3, pp. 907–915, Jan. 2009. [Cited on pages 10, 13, and 62.]

[44] G. Bo, L. Ren, X. Xu, Y. Du, and S. Dou, "Recent progress on liquid metals and their applications," *Advances in Physics: X*, vol. 3, no. 1, p. 1446359, Jan. 2018. [Cited on pages 10, 12, and 32.]

[45] T. Liu, P. Sen, and C.-J. Kim, "Characterization of nontoxic liquid-metal alloy galinstan for applications in microdevices," *Journal of Microelectromechanical Systems*, vol. 21, no. 2, pp. 443–450, Apr. 2012. [Cited on page 10.]

[46] R. A. Bilodeau, D. Y. Zemlyanov, and R. K. Kramer, "Liquid metal switches for environmentally responsive electronics," *Advanced Materials Interfaces*, vol. 4, no. 5, Jan. 2017. [Cited on pages 10, 12, 13, 32, and 51.]

[47] Q. Zhang and J. Liu, "Nano liquid metal as an emerging functional material in energy management, conversion and storage," *Nano Energy*, vol. 2, no. 5, pp. 863–872, sep 2013. [Cited on pages 10 and 12.]

[48] S. Handschuh-Wang, F. J. Stadler, and X. Zhou, "Critical review on the physical properties of gallium-based liquid metals and selected pathways for their alteration," *The Journal of Physical Chemistry C*, vol. 125, no. 37, pp. 20 113–20 142, Sep. 2021. [Cited on pages 11, 12, 31, 34, and 61.]

[49] F.-M. Allioux, M. B. Ghasemian, W. Xie, A. P. O'Mullane, T. Daeneke, M. D. Dickey, and K. Kalantar-Zadeh, "Applications of liquid metals in nanotechnology," *Nanoscale Horizons*, vol. 7, no. 2, pp. 141–167, 2022. [Cited on pages 11 and 12.]

[50] H. Li and J. Liu, "Revolutionizing heat transport enhancement with liquid metals: Proposal of a new industry of water-free heat exchangers," *Frontiers in Energy*, vol. 5, no. 1, pp. 20–42, Feb. 2011. [Cited on page 12.]

[51] Z. Zeng, C. Wang, M. Zeng, and L. Fu, “Gallium-Based Liquid Metals in Rechargeable Batteries: From Properties to Applications,” *Small*, Jan. 2024. [Cited on page 12.]

[52] P. Geddis, L. Wu, A. McDonald, S. Chen, and B. Clements, “Effect of static liquid galinstan on common metals and non-metals at temperatures up to 200 °c,” *Canadian Journal of Chemistry*, vol. 98, no. 12, pp. 787–798, Dec. 2020. [Cited on pages 11, 12, 13, and 62.]

[53] Q. Yu, Q. Zhang, J. Zong, S. Liu, X. Wang, X. Wang, H. Zheng, Q. Cao, D. Zhang, and J. Jiang, “Identifying surface structural changes in a newly-developed ga-based alloy with melting temperature below 10ºc,” *Applied Surface Science*, vol. 492, pp. 143–149, oct 2019.

[54] X. Wu, H. Fang, X. Ma, and S. Yan, “Gallium-Based Liquid Metals: Optical Properties, Applications, and Challenges,” *Advanced Optical Materials*, vol. 11, no. 22, Oct. 2023.

[55] X.-H. Yang and J. Liu, *Advances in Liquid Metal Science and Technology in Chip Cooling and Thermal Management*. Elsevier, 2018, pp. 187–300.

[56] P. Song, Y. Zhu, Z. An, M. Wei, X. Sun, and Y. Zhang, “Performance study on an electrocaloric heat pump based on ga-based liquid metal,” *Energies*, vol. 16, no. 7, p. 3104, Mar. 2023. [Cited on page 12.]

[57] A. Koh, W. Hwang, P. Y. Zavalij, S. Chun, G. Slipher, and R. Mrozek, “Solidification and melting phase change behavior of eutectic gallium-indium-tin,” *Materialia*, vol. 8, p. 100512, Dec. 2019. [Cited on pages 11, 31, and 32.]

[58] A. Koh, R. Mrozek, and G. Slipher, “Characterization and manipulation of interfacial activity for aqueous galinstan dispersions,” *Advanced Materials Interfaces*, vol. 5, no. 5, Jan. 2018. [Cited on pages 12 and 32.]

[59] S. Liu, X. Sun, N. Kemme, V. G. Damle, C. Schott, M. Herrmann, and K. Rykaczewski, “Can liquid metal flow in microchannels made of its own oxide skin?” *Microfluidics and Nanofluidics*, vol. 20, no. 1, Jan. 2016. [Cited on page 12.]

[60] G. Speckbrock, S. Kamitz, M. Alt, and H. Schmitt, “Low melting gallium, indium, and tin eutectic alloys, and thermometers employing same. US Patent US6019509A,” 1997. [Cited on page 12.]

[61] T. Hao, H. Ma, and X. Ma, "Experimental investigation of oscillating heat pipe with hybrid fluids of liquid metal and water," *Journal of Heat Transfer*, vol. 141, no. 7, May 2019. [Cited on pages 13 and 62.]

[62] H. Yan, W. Zhang, Y. Cui, F. Qian, D. Wei, P. Guo, K. Jiao, J. Huang, Q. Wang, and C. Zhao, "Durable drag reduction and anti-corrosion for liquid flows inside lubricant-infused aluminum/copper capillaries," *Chemical Engineering Science*, vol. 266, p. 118275, Feb. 2023. [Cited on page 13.]

[63] A. Shimizu, Y. Kakehi, S. Bono, and S. Konishi, "Liquid metal droplet shuttling in a microchannel toward a single line multiplexer with multiple sensors," *Scientific Reports*, vol. 12, no. 1, Mar. 2022. [Cited on pages 13 and 62.]

[64] J. So, J. Thelen, A. Qusba, G. J. Hayes, G. Lazzi, and M. D. Dickey, "Reversibly Deformable and Mechanically Tunable Fluidic Antennas," *Advanced Functional Materials*, vol. 19, no. 22, pp. 3632–3637, Nov. 2009. [Cited on page 62.]

[65] M. D. Dickey, R. C. Chiechi, R. J. Larsen, E. A. Weiss, D. A. Weitz, and G. M. Whitesides, "Eutectic Gallium-Indium (EGaIn): A Liquid Metal Alloy for the Formation of Stable Structures in Microchannels at Room Temperature," *Advanced Functional Materials*, vol. 18, no. 7, pp. 1097–1104, Apr. 2008.

[66] S. Bhagwat, C. O'Brien, A. Hamza, S. Sharma, C. Rein, M. Sanjaya, D. Helmer, F. Kotz-Helmer, P. Pezeshkpour, and B. E. Rapp, "An On-Chip Liquid Metal Plug Generator," *Advanced Materials*, vol. 34, no. 23, May 2022.

[67] Y. He, J. You, M. D. Dickey, and X. Wang, "Controllable flow and manipulation of liquid metals," *Advanced Functional Materials*, Oct. 2023.

[68] Z. Liu, S. Qin, X. Chen, D. Chen, and F. Wang, "Pdms-pdms micro channels filled with phase-change material for chip cooling," *Micromachines*, vol. 9, no. 4, p. 165, Apr. 2018. [Cited on pages 13 and 62.]

[69] M. S. Anwar and A. Bangert, "3d printed microfluidics-based reconfigurable antenna," in *2017 IEEE MTT-S International Microwave Workshop Series on Advanced Materials and Processes for RF and THz Applications (IMWS-AMP)*. IEEE, Sep. 2017. [Cited on page 13.]

[70] G. B. Zhang, R. C. Gough, M. R. Moorefield, A. T. Ohta, and W. A. Shiroma, "An electrically actuated liquid-metal switch with metastable switching states," in *2016*

IEEE MTT-S International Microwave Symposium (IMS). IEEE, May 2016. [Cited on page 13.]

[71] G. B. Zhang, R. C. Gough, M. R. Moorefield, K. J. Cho, A. T. Ohta, and W. A. Shiroma, “A liquid-metal polarization-pattern-reconfigurable dipole antenna,” *IEEE Antennas and Wireless Propagation Letters*, vol. 17, no. 1, pp. 50–53, Jan. 2018. [Cited on page 13.]

[72] J. Liu, Y.-X. Zhou, Y.-G. Lv, and T. Li, “Liquid Metal Based Miniaturized Chip-Cooling Device Driven by Electromagnetic Pump,” in *Electronic and Photonic Packaging, Electrical Systems Design and Photonics, and Nanotechnology*, ser. IMECE2005. ASMEDC, Jan. 2005. [Cited on pages 13 and 19.]

[73] Ricardo Pinto (2023). Magnetic Fluids Based Heat Dissipators. Faculdade de Ciencias da Universidade do Porto, Porto, Portugal. [Cited on pages 13, 47, and 53.]

[74] M. Xiong, Y. Gao, and J. Liu, “Fabrication of magnetic nano liquid metal fluid through loading of ni nanoparticles into gallium or its alloy,” *Journal of Magnetism and Magnetic Materials*, vol. 354, pp. 279–283, Mar. 2014. [Cited on pages 14 and 37.]

[75] W. Xiang, Y. Lu, H. Wang, X. Sun, S. Chen, Z. He, and J. Liu, “Liquid-metal-based magnetic fluids,” *Nature Reviews Materials*, vol. 9, no. 6, pp. 433–449, May 2024. [Cited on pages 14, 37, 47, 50, 69, and 80.]

[76] X. He, M. Ni, J. Wu, S. Xuan, and X. Gong, “Hard-magnetic liquid metal droplets with excellent magnetic field dependent mobility and elasticity,” *Journal of Materials Science & Technology*, vol. 92, pp. 60–68, Nov. 2021. [Cited on page 14.]

[77] R. ITO, G. DODBIBA, and T. FUJITA, “Mr fluid of liquid gallium dispersing magnetic particles,” *International Journal of Modern Physics B*, vol. 19, no. 07n09, pp. 1430–1436, Apr. 2005. [Cited on page 14.]

[78] S. O. Tan and H. Demirel, “Performance and cooling efficiency of thermoelectric modules on server central processing unit and northbridge,” *Computers & Electrical Engineering*, vol. 46, pp. 46–55, Aug. 2015. [Cited on pages 14, 17, and 18.]

[79] M. Platini, T. Ropars, B. Pelletier, and N. De Palma, “Cpu overheating prediction in hpc systems,” *Concurrency and Computation: Practice and Experience*, vol. 33, no. 13, Mar. 2021. [Cited on pages 14 and 15.]

[80] ——, "CPU Overheating Characterization in HPC Systems: A Case Study," in *2018 IEEE/ACM 8th Workshop on Fault Tolerance for HPC at eXtreme Scale (FTXS)*. IEEE, Nov. 2018. [Cited on page 15.]

[81] S. Lafond, S. Holmbacka, and J. Lilius, "Energy aware software: Issues, approaches and challenges," in *2016 Seventh International Green and Sustainable Computing Conference (IGSC)*. IEEE, 2016. [Cited on page 15.]

[82] A. Merkel and F. Bellosa, "Balancing power consumption in multiprocessor systems," *ACM SIGOPS Operating Systems Review*, vol. 40, no. 4, pp. 403–414, Apr. 2006. [Cited on page 15.]

[83] T. Abbas, K. Abd-elsalam, and K. Khodairy, "Cpu thermal management of personal and notebook computer (transient study)," in *2010 3rd International Conference on Thermal Issues in Emerging Technologies Theory and Applications*. IEEE, Dec. 2010. [Cited on pages 16, 17, and 18.]

[84] J. D. Carr, "An examination of cpu cooling technologies thermal management options for engineers," 2014. [Online]. Available: https://api.semanticscholar.org/CorpusID:45735301 [Cited on pages 16, 17, 18, and 20.]

[85] *Arrow, 31 October 2019, Understanding heat sinks: Functions, types, & more, Arrow , accessed on 30 june 2024*, Std. [Online]. Available: https://www.arrow.com/en/research-and-events/articles/understanding-heat-sinks-functions-types-and-more [Cited on page 16.]

[86] *Wellste - Division of Bigle, Pin Fin Heat Sink, accessed on 30 june 2024*, Std. [Online]. Available: https://www.wellste.com/pin-fin-heat-sink/ [Cited on page 16.]

[87] *How Do Heat Pipes Work | Heat Pipes 101, celsia - Making Hot Technology Cooler, accessed on 30 june 2024*, Std. [Online]. Available: https://celsiainc.com/heat-sink-blog/how-do-heat-pipes-work/ [Cited on page 17.]

[88] *Peter Thackeray, 23 April 2020, Are heat pipes any good for my CPU?, Siemens - blogs, accessed on 30 june 2024*, Std. [Online]. Available: https://blogs.sw.siemens.com/simcenter/are-heat-pipes-any-good-for-my-cpu/ [Cited on page 17.]

[89] *2 May 2017, Removal and installation steps for thermal fan assembly - ThinkPad X270, Lenovo, accessed on 30 june 2024*, Std. [Online]. Available: https://support.lenovo.com/pt/en/solutions/pd104662-

removal-and-installation-steps-for-thermal-fan-assembly-thinkpad-x270 [Cited on page 18.]

[90] *Ascendtech, Lenovo 130-14AST Heatsink Fan Assembly, accessed on 4 september 2024,*, Std. [Online]. Available: http://www.ascendtech.us/lenovo-130-14ast-heatsink-fan-assembly_i_htsla5h40r34396.aspx [Cited on page 18.]

[91] T. Li, Y.-G. Lv, J. Liu, and Y.-X. Zhou, "A powerful way of cooling computer chip using liquid metal with low melting point as the cooling fluid," *Forschung im Ingenieurwesen*, vol. 70, no. 4, pp. 243–251, Aug. 2006. [Cited on page 19.]

[92] *CPU Cooler: Liquid Cooling Vs. Air Cooling, intel, accessed on 30 june 2024*, Std. [Online]. Available: https://www.intel.com/content/www/us/en/gaming/resources/cpu-cooler-liquid-cooling-vs-air-cooling.html [Cited on page 19.]

[93] C. Li, D. Jiao, J. Jia, F. Guo, and J. Wang, "Thermoelectric cooling for power electronics circuits: Modeling and active temperature control," *IEEE Transactions on Industry Applications*, vol. 50, no. 6, pp. 3995–4005, Nov. 2014. [Cited on page 19.]

[94] R. Rodrigues, T. Jiang, and D. Das, "Comparison of cooling solutions to improve overload capability of power semiconductor devices," in *2018 IEEE Energy Conversion Congress and Exposition (ECCE)*. IEEE, Sep. 2018. [Cited on page 19.]

[95] N. W. Ashcroft and N. D. Mermin, *Solid state physics*, repr. ed. South Melbourne [u.a.]: Brooks/Cole Thomson Learning, 2012, hier auch später erschiene, unveränderte Nachdrucke!! [Cited on page 24.]

[96] C. O. Amorim, F. Mohseni, R. K. Dumas, V. S. Amaral, and J. S. Amaral, "A geometry-independent moment correction method for the MPMS3 SQUID-based magnetometer," *Measurement Science and Technology*, vol. 32, no. 10, p. 105602, Jul. 2021. [Cited on page 25.]

[97] *Quantum Design, Magnetic Property Measurement System - MPMS3 User's manual, available at: <https://www.qdusa.com/pharosindex/> (accessed on 5 august 2024)*, Std. [Cited on page 25.]

[98] M. Heaney, *Electrical Conductivity and Resistivity*, 01 2003, pp. 7–1 to 7. [Cited on page 26.]

[99] Filipa Furriel (2021). Magnetocaloric Ferrofluids. Faculdade de Ciencias da Universidade do Porto, Porto, Portugal. [Cited on pages 26 and 53.]

[100] F. Sar and J.-G. Gasser, “Electronic transport properties of liquid ga–zn alloys,” *Intermetallics*, vol. 11, no. 11–12, pp. 1369–1376, 2003. [Cited on page 27.]

[101] *Royal Society of Chemistry, Tin - Element information, properties and uses - Periodic Table., accessed 17 November 2023*, Std. [Online]. Available: https://www.rsc.org/periodic-table/element/50/tin [Cited on page 30.]

[102] I. D. Joshipura, C. K. Nguyen, C. Quinn, J. Yang, D. H. Morales, E. Santiso, T. Daeneke, V. K. Truong, and M. D. Dickey, “An atomically smooth container: Can the native oxide promote supercooling of liquid gallium?” *iScience*, vol. 26, no. 4, p. 106493, Apr. 2023. [Cited on page 32.]

[103] X. Wang, D. V. M. Repaka, A. Suwardi, Q. Zhu, J. Wu, and J. Xu, “Thermal and electrical properties of liquid metal gallium during phase transition,” *Transactions of Tianjin University*, vol. 29, no. 3, pp. 209–215, Jun. 2023. [Cited on page 32.]

[104] C. Suryanarayana, “Mechanical alloying and milling,” *Progress in Materials Science*, vol. 46, no. 1–2, pp. 1–184, Jan. 2001. [Cited on page 35.]

[105] R. O. Fleming, S. Gonçalves, A. Davarpanah, I. Radulov, L. Pfeuffer, B. Beckmann, K. Skokov, Y. Ren, T. Li, J. Evans, J. Amaral, R. Almeida, A. Lopes, G. Oliveira, J. P. Araújo, A. Apolinário, and J. H. Belo, “Tailoring negative thermal expansion via tunable induced strain in la–fe–si-based multifunctional material,” *ACS Applied Materials & Interfaces*, vol. 14, no. 38, pp. 43 498–43 507, Sep. 2022. [Cited on page 35.]

[106] S. J. Dapkunas and A. Jillavenkatesa, *NIST recommended practice guide :: particle size characterization/*, 2001. [Cited on pages 35 and 40.]

[107] J. Rodriguez-Carvajal, “Recent developments of the program fullprof, commission on powder diffraction,” *IUCr Newsl.*, vol. 26, 01 2001. [Cited on pages 36 and 44.]

[108] A. J. Bradley and A. Taylor, “An X-ray analysis of nickel-aluminum system,” *Proceedings of the Royal Society of London. Series A - Mathematical and Physical Sciences*, vol. 159, no. 896, pp. 56–72, Mar. 1937. [Cited on pages 36, 44, and 85.]

[109] “The magnetization of pure iron and nickel,” *Proceedings of the Royal Society of London. A. Mathematical and Physical Sciences*, vol. 321, no. 1547, pp. 477–491, mar 1971. [Cited on page 36.]

[110] G. DODBIBA, K. ONO, H. S. PARK, S. MATSUO, and T. FUJITA, "FeNbVB ALLOY PARTICLES SUSPENDED IN LIQUID GALLIUM: INVESTIGATING THE MAGNETIC PROPERTIES OF THE MR SUSPENSION," *International Journal of Modern Physics B*, vol. 25, no. 07, pp. 947–955, Mar. 2011. [Cited on page 37.]

[111] N. Abid, A. M. Khan, S. Shujait, K. Chaudhary, M. Ikram, M. Imran, J. Haider, M. Khan, Q. Khan, and M. Maqbool, "Synthesis of nanomaterials using various top-down and bottom-up approaches, influencing factors, advantages, and disadvantages: A review," *Advances in Colloid and Interface Science*, vol. 300, p. 102597, Feb. 2022. [Cited on page 38.]

[112] A. Tago, N. Yamauchi, K. Nakashima, D. Nagao, and Y. Kobayashi, "Effect of silica-coating on crystal structure and magnetic properties of metallic nickel particles," *Advanced Powder Technology*, vol. 32, no. 11, pp. 4177–4185, Nov. 2021. [Cited on pages 38, 44, 45, and 85.]

[113] J.-T. Lue, "A review of characterization and physical property studies of metallic nanoparticles," *Journal of Physics and Chemistry of Solids*, vol. 62, no. 9–10, pp. 1599–1612, Sep. 2001. [Cited on page 40.]

[114] X.-F. Zhang, Z.-G. Liu, W. Shen, and S. Gurunathan, "Silver Nanoparticles: Synthesis, Characterization, Properties, Applications, and Therapeutic Approaches," *International Journal of Molecular Sciences*, vol. 17, no. 9, p. 1534, Sep. 2016. [Cited on page 40.]

[115] E. S. D. T. de Mendonça, A. C. B. de Faria, S. C. L. Dias, F. F. Aragón, J. C. Mantilla, J. A. Coaquira, and J. A. Dias, "Effects of silica coating on the magnetic properties of magnetite nanoparticles," *Surfaces and Interfaces*, vol. 14, pp. 34–43, Mar. 2019. [Cited on page 41.]

[116] N. Mironova-Ulmane, A. Kuzmin, I. Steins, J. Grabis, I. Sildos, and M. Pärs, "Raman scattering in nanosized nickel oxide nio," *Journal of Physics: Conference Series*, vol. 93, p. 012039, Dec. 2007. [Cited on pages 42 and 43.]

[117] S. Donthu, D. Chi, S. Tripathy, A. Wong, and S. Chua, "Micro-raman spectroscopic investigation of nisi films formed on bf2 +-, b+- and non-implanted (100)si substrates," *Applied Physics A*, vol. 79, no. 3, pp. 637–642, Aug. 2004. [Cited on page 43.]

[118] P. McMillan, “Structural studies of silicate glasses and melts-applications and limitations of raman spectroscopy,” *American Mineralogist - AMER MINERAL*, vol. 69, pp. 622–644, 07 1984. [Cited on page 43.]

[119] D. Kumar, H. Singh, and S. Banerjee, “Controlled design of phase specific ni nanoparticles from different precursors and their antibacterial activities,” *Advanced Science, Engineering and Medicine*, vol. 8, no. 5, pp. 339–349, Jun. 2016. [Cited on pages 44 and 85.]

[120] M. Ammar, F. Mazaleyrat, J. P. Bonnet, P. Audebert, A. Brosseau, G. Wang, and Y. Champion, “Synthesis and characterization of core–shell structure silica-coated fe29.5ni70.5nanoparticles,” *Nanotechnology*, vol. 18, no. 28, p. 285606, Jun. 2007. [Cited on page 45.]

[121] A. C. Johnston-Peck, J. Wang, and J. B. Tracy, “Synthesis and structural and magnetic characterization of ni(core)/nio(shell) nanoparticles,” *ACS Nano*, vol. 3, no. 5, pp. 1077–1084, Apr. 2009. [Cited on page 45.]

[122] Keerthivasan Rajamani (2022). A Magnetocaloric Mixture Based Refrigerator - From Material to System Level Analysis. Faculty of Engineering Technology, University of Twente, The Netherlands. [Cited on page 53.]

[123] L. Ren, J. Zhuang, G. Casillas, H. Feng, Y. Liu, X. Xu, Y. Liu, J. Chen, Y. Du, L. Jiang, and S. X. Dou, “Nanodroplets for stretchable superconducting circuits,” *Advanced Functional Materials*, vol. 26, no. 44, pp. 8111–8118, Sep. 2016. [Cited on page 54.]

[124] Andre Miguel Trindade Pereira, Joao Oliveira Ventura, et.al. (2017). Magnetocaloric Refrigerator or Heat Pump Comprising an Externally Activatable Thermal Switch (WO/2017/175186). [Online]. Available: https://patentscope.wipo.int/search/en/detail.jsf?docId=WO2017175186 [Cited on page 55.]

[125] *WikiChip - Chips & Semi, Core i5-6600K - Intel, accessed on 9 december 2024*, Std. [Online]. Available: https://en.wikichip.org/wiki/intel/core_i5/i5-6600k#google_vignette [Cited on page 63.]

[126] P. Roca-Cusachs, F. Rico, E. Martínez, J. Toset, R. Farré, and D. Navajas, “Stability of microfabricated high aspect ratio structures in poly(dimethylsiloxane),” *Langmuir*, vol. 21, no. 12, pp. 5542–5548, Apr. 2005. [Cited on page 63.]

[127] I. Maia, C. Rocha, P. Pontes, V. Cardoso, J. M. Miranda, A. S. Moita, G. Minas, A. L.N. Moreira, and R. Lima, *Heat Transfer and Fluid Flow Investigations in PDMS Microchannel Heat Sinks Fabricated by Means of a Low-Cost 3D Printer*. IntechOpen, May 2020. [Cited on page 64.]

[128] *Matbase - Material Properties Database, Material Properties of Polylactic Acid (PLA), Agro Based Polymers, accessed on 10 august 2024* , Std. [Online]. Available: https://web.archive.org/web/20120210194852/http://www.matbase.com/material/polymers/agrobased/polylactic-acid-pla/properties [Cited on page 64.]

[129] C. Yang, W. Wang, and Z. Li, "Optimization of corona-triggered pdms-pdms bonding method," in *2009 4th IEEE International Conference on Nano/Micro Engineered and Molecular Systems*. IEEE, 2009. [Cited on page 66.]

[130] B. Mosadegh, H. Tavana, S. C. Lesher-Perez, and S. Takayama, "High-density fabrication of normally closed microfluidic valves by patterned deactivation of oxidized polydimethylsiloxane," *Lab Chip*, vol. 11, no. 4, pp. 738–742, 2011. [Cited on page 66.]

[131] S. Satyanarayana, R. Karnik, and A. Majumdar, "Stamp-and-stick room-temperature bonding technique for microdevices," *Journal of Microelectromechanical Systems*, vol. 14, no. 2, pp. 392–399, Apr. 2005. [Cited on page 66.]

[132] S. Doganay, L. Cetin, M. A. Ezan, and A. Turgut, "A rotating permanent magnetic actuator for micropumping devices with magnetic nanofluids," *Journal of Micromechanics and Microengineering*, vol. 30, no. 7, p. 075012, May 2020. [Cited on page 68.]

[133] J. M. D. Coey, *Magnetism and magnetic materials*. Cambridge: Cambridge University Press, 2009, includes bibliographical references and index. [Cited on page 69.]

[134] T. T. Hoang, P. T. Phan, M. T. Thai, J. Davies, C. C. Nguyen, H.-P. Phan, N. H. Lovell, and T. N. Do, "Magnetically engineered conductivity of soft liquid metal composites for robotic, wearable electronic, and medical applications," *Advanced Intelligent Systems*, vol. 4, no. 12, Oct. 2022. [Cited on page 69.]

[135] N. Damle and Y. Joshi, "Experimental and analytical study of the hydrodynamic and single and two-phase convective heat transfer performance of flexible pdms

microchannels with micropillar arrays," *Applied Thermal Engineering*, vol. 224, p. 119799, Apr. 2023. [Cited on page 71.]

[136] V. Lienhard, John H. and V. Lienhard, John H., *Heat Transfer Textbook Fifth Edition*. Dover Publications, Incorporated, 2019. [Cited on pages 72 and 91.]

[137] *Polymer Data Handbook: Second Edition*. Oxford University PressNew York, NY, May 2009. [Cited on pages 72 and 92.]

[138] M. Poole and R. Bowtell, "Novel gradient coils designed using a boundary element method," *Concepts in Magnetic Resonance Part B: Magnetic Resonance Engineering*, vol. 31B, no. 3, pp. 162–175, Jul. 2007. [Cited on page 80.]

[139] S. S. Hidalgo-Tobon, "Theory of gradient coil design methods for magnetic resonance imaging," *Concepts in Magnetic Resonance Part A*, vol. 36A, no. 4, pp. 223–242, Jul. 2010. [Cited on page 80.]

[140] C. Qi, N. Sugita, and T. Shinshi, "Development of a flexible coil based on conductive polymer composite for pdms-based soft electromagnetic microactuators," *Sensors and Actuators A: Physical*, vol. 363, p. 114766, Dec. 2023. [Cited on page 80.]

[141] B. Moffat, M. Desmulliez, K. Brown, C. Desai, D. Flynn, and A. Sutherland, "A microfabricated current sensor for arc fault detection of aircraft wiring," in *2008 2nd Electronics Systemintegration Technology Conference*, vol. 62. IEEE, Sep. 2008, pp. 299–304. [Cited on page 80.]

[142] C. Wang, C. Calderón, and Y. Wang, "An experimental study of a thermoelectric heat exchange module for domestic space heating," *Energy and Buildings*, vol. 145, pp. 1–21, Jun. 2017. [Cited on page 89.]

[143] Thanigaivelan, R. and Deepa, D and Mythili, T and Arunachalam, Ramanathan, "Experimental Investigation of Natural Convective Heat Transfer Around Micro-fin Arrays," vol. 76, pp. 501–505, 08. [Cited on page 90.]

[144] *Philosophical Transactions of the Royal Society of London*, vol. 22, no. 270, pp. 824–829, Apr. 1701. [Cited on page 91.]

[145] S. Maruyama and S. Moriya, "Newton's law of cooling: Follow up and exploration," *International Journal of Heat and Mass Transfer*, vol. 164, p. 120544, Jan. 2021.

[146] U. Besson, “The history of the cooling law: When the search for simplicity can be an obstacle,” *Science Education*, vol. 21, no. 8, pp. 1085–1110, Nov. 2010. [Cited on page 91.]

[147] *Convective Heat Transfer Coefficients Table Chart, Engineers Edge, accessed on 15 august 2024*, Std. [Online]. Available: https://www.engineersedge.com/heat_transfer/convective_heat_transfer_coefficients__13378.htm [Cited on page 92.]